Strain Relaxation in SiGe/Si Heteroepitaxy

Lydia Helena Wong

School of Materials Science and Engineering

A thesis submitted to the Nanyang Technological University
in fulfilment of the requirement for the degree of
Doctor of Philosophy

2007

ACKNOWLEDGEMENTS

First of all, I would like to thank my thesis advisor, Professor Wong Chee Cheong, who has always believed in me since the beginning. His enthusiasm is often contagious, his zeal towards education and research are always inspiring. I am indeed fortunate to learn from such a great teacher.

I sincerely thank the following brilliant researchers who helped me start and carry on this project. Firstly, to Dr Liu Jinping, who introduced the fascinating heteroepitaxy area and produced fantastic samples for this project. I am forever in debt to Dr Cristiano Ferraris, who has patiently taught me everything I need to know about TEM and brought this project to a more sophisticated level of analysis. He has made the otherwise dull and complicated TEM training to be a fun and captivating experience. I would also thank Professor Filippo Romanato, who has shared his knowledge in heteroepitaxy growth and characterization so generously.

This project is a collaboration work with Chartered Semiconductor, where I had the opportunity to be trained by these exceptional people. I would like to thank Dr Lap Chan, whose passion for knowledge has inspired me to never stop learning. I am grateful to Dr Alex See and Mr. Tee Kheng Chok who have shared their knowledge on materials characterization and device integration.

This thesis involves a variety of characterization techniques, which became accessible because of the following people. I would like to acknowledge Professor Shen Zexiang who let me use his Raman facility generously. I would also like to thank Dr Foo Yong Lim for the coaching in Reciprocal Space Map analysis and the access to the RSM facility at IMRE. I am grateful for the RBS acquisition and analyses by Professor Thomas Osipowicz and Dr Debbie Sng. I would also like to express my gratitude to Dr

Ramesh Rao for the early training of HR-XRD and the occasional assistance with AES. I would like to thank Doreen Lai and Clark Ong for SIMS analyses. Lastly, I am grateful for the assistance and friendship of the present and previous technicians of Microelectronics Lab: Mastura, Yani, Sandy, Jing Li and Fiona. Irene, GuoJun, Xu Cheng and Swee Sing are acknowledged for their assistance in SEM, TEM sample preparation, and AFM, respectively.

This PhD journey has been exciting, unpredictable and sometimes depressing. The following people have made it bearable and enjoyable. My lunch-time friends: Lay Kuan, Yeong Huey, Pui Woon and Xiao Fang, who have lent listening ears, offered comforting words and whose friendship I would keep and cherish forever. The Special Project big family especially Batch 7, who has been a wonderful group of friends whose company has been encouraging and refreshing. I am looking forward to working with all of you at Chartered.

I am truly blessed to be born and raised in a loving family, who always believe in me even in times when I do not. Herewith, I dedicate this thesis to my parents, whose unconditional love has kept me going at all times. I would also like to thank Hendra, for listening to my new hypotheses, easing my mind off any stressful situations, and most of all, for his constant supportive love.

Last but not least, I would like to give my greatest praise and thanksgiving to the Heavenly Father for showing the right path and faithfully walking with me all the way.

TABLE OF CONTENTS

Appendices

LIST OF FIGURES

LIST OF TABLES

Page

ABSTRACT

Heteroepitaxy of lattice-mismatched materials are important for both optoelectronic and microelectronic applications. Within the community of research in heteroepitaxy, the long-standing goal is to obtain strain relaxation while minimizing the generation of defects which often leads to device degradation.

The focus of this study is SiGe/Si heteroepitaxy, designed to meet the device requirements of strained-Si based transistors. The most widely adopted approach for reducing threading dislocation density (TDD) in this materials system is the insertion of a buffer layer between the relaxed SiGe and Si substrate. Due to the growing importance of advanced materials, understanding methods of lattice relaxation is generally important for advancing new methods of lattice-engineering and engineered-substrate creation. This thesis describes the discovery and development of two novel buffer systems: a) the reverse-graded (RG) buffer system and b) the SiGe/SiGeC superlattice buffer system. Both systems have succeeded in reducing TDD in SiGe/Si. Their development and characterization, and the strain relaxation mechanisms will be fully described.

A comprehensive study of strain relaxation requires a simple and accurate strain quantification method. Raman spectroscopy is one of the most convenient techniques, yet strain-shift coefficients for accurate strain quantification of strained Si and strained SiGe have not been agreed upon unanimously. The first direct measurement of strain-shift coefficient for strained Si is presented and yields a measured value of -784 ± 4 cm^{-1}. The strain shift coefficient of SiGe is found to be a strong function of Ge concentration (x), and follows the empirical relation: $b = -773.8 - 897.7x$ for $x<0.35$.

The first buffer system described in this thesis, the reverse-graded (RG) buffer layer, has a lattice mismatch which starts at the highest value at the RG/Si interface and decreases to a final mismatch at the RG/SiGe interface. Relaxed $Si_{1-x}Ge_x$ ($x = 0.14$-0.35) layers with TDD of $10^5/cm^2$ were successfully grown on a 90 nm RG layer. Using Transmission Electron Microscope (TEM) and Reciprocal Space Mapping (RSM), we were able to trace the origin of low TDD to the localized accumulation of misfit dislocations at the RG/Si interface and the large residual strain in the RG layer. Extension of an equilibrium strain relaxation theory allowed us to identify the uniqueness of the RG concept to be the large initial misfit at the interface, which helps to quickly supersaturate strain for dislocation nucleation rather than the conventional reliance on buffer thickness to induce relaxation. Used judiciously, we postulate that this technique could benefit heteroepitaxial growth on any substrates simply by using another material with similar crystal structure and a larger lattice constant as a buffer layer.

The second novel buffer layer concept, the SiGe/SiGeC superlattice, has also been demonstrated. In this heterostructure, TDD decreases with relaxation, in stark contrast to the commonly observed opposite tendency. TEM results revealed the presence of $Si_{1-x-y}Ge_xC_y$ domains (with $x \leq 0.23$ and $y \leq 0.01$) after annealing at 1000 °C. It is inferred that these domains assist the low TDD relaxation by releasing the epitaxial misfit strain as localized discrete strain and by facilitating the formation of pure edge dislocations from 60° misfit dislocations leading to TD annihilation.

In summary, this thesis demonstrates two different routes for the relaxation of strained layers which minimize the traditional penalty of threading dislocations. More importantly, this work demonstrates the effectiveness of interfacial strain relief and localized strain relief in influencing the kinetics of relaxation. These concepts, with further development, could hold the keys to improved strain relaxation in other important material systems.

Chapter 1:

Introduction

1.1. Background

Heteroepitaxy of lattice-mismatched materials is a central topic in the materials science and engineering of thin films. Such materials are important for both optoelectronic and microelectronic applications, such as II-VI and III-V semiconductor lasers [1, 2], SiGe heterojunction bipolar transistor (HBTs) [3], and strained channel field-effect-transistors [4, 5]. When a material is grown on another substrate of different lattice constant, a lattice mismatch strain is generated in the epitaxial layer and is not relaxed if its thickness does not exceed the critical thickness [6]. For thicknesses beyond the critical thickness, strain energy is released by the formation of misfit dislocations, which is found to be deleterious for device performance [7, 8]. It has been the long-standing goal of the heteroepitaxy research community to induce strain relaxation with the least amount of defect density. This thesis aims to reduce defect density of the strain-relaxed SiGe/Si heteroepitaxy, designed to meet the device requirements of strained-Si based transistors (Fig. 1.1).

Recent reports from the International Electron Device Meetings (IEDM) show the emerging of strained-channel technology, the key driver to extend Moore's law when geometric scaling has become a complicated and problematic solution [9-11]. The modified strained Si band structure suppresses intervalley scattering, reduces effective mass and hence improves carrier mobility [12, 13]. The effective mobility of electrons and holes were reported to increase by up to 3 times in strained Si channels and 8 times in strained Ge channels, respectively [4,14,15], resulting in up to 3 times drive current improvement in NMOS and PMOS transistors [16].

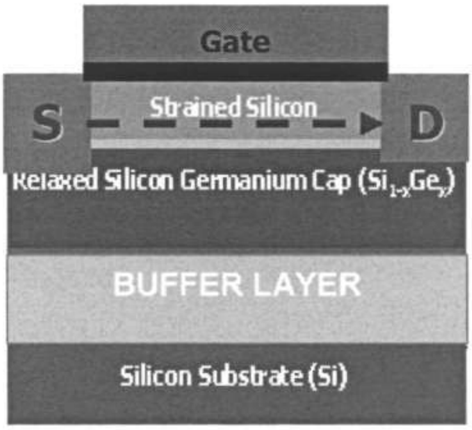

Figure 1.1. Schematic of strained Si/relaxed SiGe/ buffer SiGe heterostructure for high-mobility transistor; S and D represent, respectively, source and drain regions.

The integration of strained channels into Si wafer processing is critically dependent on the success of heteroepitaxy technology, which remains a challenging proposition. The 4.2 % lattice constant mismatch between pure Si (a = 0.543 nm) and Ge (a=0.569 nm) must be accommodated with minimum threading dislocation density (TDD). If strained Si is grown on a relaxed SiGe directly grown on Si substrate, the typical TDD is between 10^9-$10^{11}/cm^2$ [17], orders of magnitude higher than pure Si substrate (< $10/cm^2$). Obviously, minimum TDD is the most important property of a relaxed SiGe heteroepitaxy. Also, the interface surface roughness of the heterostructure must be kept as low as possible because it may directly affect hole mobility enhancement [18]. Stability of strain at high temperatures commonly used in device fabrication is another desirable requirement. Lastly, the total thickness of SiGe and the buffer layer, usually inserted between SiGe and Si substrate to minimize TDD, should be as thin as possible because SiGe has a poorer thermal dissipation than Si [19].

The growth of SiGe on Si mesa structures has been shown to reduce misfit and threading dislocation density as the nucleation sources of misfit dislocations is reduced and the existing few misfit dislocations are able to glide to the mesa edges [20]. Elastic relaxation without defect generation is possible if the mesa aspect ratio (~ 1) is carefully controlled [21, 22]. However, a more stringent device lay-out design must be imposed to adopt this method for device processing. Moreover, the non-homogenous mesa thickness may cause serious problems in subsequent processes. Chemical mechanical polishing (CMP) of non-planar surface, for example, may lead to complications in Lithography. Another approach is to make use of the elastic strain transfer between SiGe and a thin Si membrane on insulator (SOI) [23, 24]. It is difficult, however, to expect uniform elastic-strain-relaxation across a 12-inch wafer because defects, commonly found in the Si membrane, resist the 'sliding' of the SiGe epilayer [25].

Buffer layers, grown between SiGe and Si substrate are often used to control TDD. A classical approach involves the growth of a strained-layer-superlattice of SiGe/Si [26, 27]; however the lowest TDD attainable by this method is 10^6/cm^2 [28]. Low temperature thin Si buffer layer growth (around 100-300 nm) was successfully demonstrated [29-31]. A high density of point defects was produced because surface atom migration is significantly restricted during low-T growth [29]. The required temperature of around 400 °C is, however, too low to be implemented practically, because there is no appreciable Si growth using normal Si hydride sources such as SiH_4 and Si_2H_6 at that temperature range for standard Chemical Vapor Deposition (CVD) epitaxial reactors. Another interesting approach involves the growth of thin SiGe layers, followed by He [32] or H^+ [33] implantation and then thermal annealing. Not only does the TDD remain high (10^7 cm^{-2}) using this approach, additional and expensive processes, such as implantation, have to be used. A well-established technique makes use of compositionally graded buffers [34, 35], in which very thick buffers (several μm) are grown on Si substrate with Ge composition increasing from the Si substrate to the buffer surface to a level of 100%Ge. Such thick buffer layer growth is expensive, introduces surface roughness, and impacts device characteristics because of the poor heat conductivity of SiGe layers compared to Si. Earlier studies found that the self-heating effect of a device on a relaxed SiGe buffer is proportional to the square root of the buffer thickness [36, 37]. Clearly, novel approaches that meet all requirements above is relevant for the semiconductor industry and understanding of such approaches would be welcomed by the research community.

1.2. Objective and scope

The objective of this thesis is to reduce dislocation density in relaxed SiGe/Si heteroepitaxial substrates for strained Si devices. The thesis is focused on the development of two novel buffer layer methods and the investigation of their relaxation mechanisms. Preliminary work, including the establishment of strain measurement techniques and investigation of strain relaxation in single heteroepitaxy layers, was carried out prior to the development of the buffer layers.

The scope of the thesis includes the following:

1. Establishment of quantitative strain measurement by Raman spectroscopy.

A comprehensive study of strain relaxation requires a simple and accurate strain quantification method. Raman spectroscopy is one of the most convenient techniques, yet strain-shift coefficients for accurate strain quantification of strained Si and strained SiGe have not been agreed upon unanimously [38-45]. Direct measurement of the strain-shift coefficient of strained Si and strained SiGe was carried out by a combination of High-resolution XRD (HR-XRD) and Raman spectroscopy.

2. Investigation of strain relaxation in single heteroepitaxial layer

The purpose of this study is to understand the classical strain relaxation mechanisms in a simple single-layer heteroepitaxial layer as a background for the development of buffer layers. Strain relaxation was induced by annealing two heterostructures, i.e. strained Si on relaxed SiGe and strained SiGe on Si substrate, at extreme annealing conditions used in device manufacturing process. Strain was quantified by Raman spectroscopy and HR-XRD and in some cases, Ge content was determined by Auger Electron Spectroscopy (AES), Secondary Ion Mass Spectroscopy (SIMS) and Rutherford Backscattering Spectroscopy (RBS). Chemical etching by Secco [46] or Wright solutions [47] was performed to reveal threading dislocations and Nomarsky microscope and Secondary Electron Microscopy (SEM) were used to observe and quantify TDD. Finally, surface roughness and morphology was investigated by Atomic Force Microscopy (AFM).

3. Investigations of a novel reverse-graded SiGe buffer

A novel concept of reverse-graded (RG) SiGe buffer layer, in which the Ge composition decreases from the substrate to the growing surface, is developed and investigated. The rationale behind this approach is derived from Tersoff's [48] equilibrium relaxation theory on forward graded SiGe layer. We hypothesize that in a RG buffer, misfit dislocations are contained at the interface with the highest lattice mismatch, i.e. the RG/Si interface. If all misfit dislocations required for strain relaxation can be confined to nucleate and glide at the interface, nucleation and glide do not necessarily happen in the graded layer, thus allowing a thinner buffer layer. . Furthermore, if most misfit dislocations are located away from the SiGe surface, roughness could possibly be reduced. It is also postulated that the residual strain in RG may assist the reduction of

TDD by promoting glide of MD towards the wafer edge and by blocking the upwards propagation of TDD. Therefore, a relaxed SiGe layer with low TDD and roughness might be grown on a thin RG buffer layer.

Relaxed SiGe layers on RG buffer layer were grown on Si substrate by low-pressure chemical vapor deposition (LP-CVD) and the epitaxial quality was characterized by HR-XRD, AFM, and TDD etching experiments. Further investigation on the relaxation mechanism used Reciprocal Space Map (RSM) technique to quantify the residual strain in the RG layer and cross-sectional and plan-view Transmission Electron Microscopy (TEM) to observe the dislocation behavior in the heterostructure. Finally, the RG heterostructure was annealed at extreme annealing condition to examine its thermal stability.

4. Investigations of a novel SiGeC/SiGe superlattice buffer

Strain relaxation of relaxed SiGe on a novel SiGeC/SiGe superlattice buffer layer is demonstrated after annealing at high temperatures. The idea stems from the fact that SiGeC decomposes into SiC precipitates when annealed at 900°C and above [49-50]. A combination of SiC precipitates and strain field in the superlattice could provide enough force to pin threading dislocations down. Furthermore, the different lattice constant between SiC and SiGe matrix may create coherency strain that transforms the epitaxial mismatch strain into localized discrete strain, resulting in a net reduction of misfit dislocation density. The growth is performed in a LP-CVD system and similar characterization techniques as above are used to investigate the epitaxial quality and strain relaxation mechanisms.

1.3. Thesis organization

This thesis is organized into 8 chapters. The background and motivation of the thesis is explained in the first chapter. A summary of relevant literature in strain relaxation and dislocation behavior in SiGe/Si heteroepitaxy system is presented in Chapter 2. A brief description of the growth technique and a more detailed explanation on the characterization techniques are given in Chapter 3. The original results of this thesis are presented and discussed in Chapter 4 to Chapter 7. Chapter 4 describes the determination of strain-shift coefficient for strain measurement using Raman spectroscopy. Strain relaxation study of single heteroepitaxy layers is presented in Chapter 5. A complete investigation of the novel reverse-graded buffer layer approach is presented in Chapter 6, and the strain relaxation of the SiGe/SiGeC buffer layer is described in Chapter 7. Finally, a summary of work done and recommended future work is presented in Chapter 8.

1.4. Impact

The original contributions of this thesis include the innovation of two novel buffer layer concepts that reduce TDD in heteroepitaxy. First, in the reverse graded (RG) SiGe buffer, the large initial mismatch at the RG/Si interface holds the key to low TDD-relaxation, enabling the use of a graded layer 10 times smaller than the widely-known forward graded layer. This concept implies that any materials can be grown in any substrate by using another material with similar crystal structure and a larger lattice constant as a buffer layer. Second, in the SiGeC/SiGe superlattice buffer, misfit strain is released by a combination of the elastic strain between the SiGeC domains/SiGe matrix and misfit dislocations. Full elastic relaxation without misfit dislocations could be achieved by increasing the density of SiGeC domains.

Chapter 2:

Literature Review

In this chapter, important concepts and recent developments in the SiGe/Si heteroepitaxy will be reviewed. The origin of strain and strain accommodation in heteroepitaxy is presented in section 2.1. The characteristics of dislocations in SiGe/Si heteroepitaxy and the critical thickness concept are explained in sections 2.2 and 2.3, respectively. In section 2.4, current understanding on the nucleation, propagation and termination of dislocations are reviewed. A summary of important buffer layer concepts for dislocation reduction is presented in section 2.5, and finally, a brief review of SiGeC/SiGe heteroepitaxy is discussed in section 2.6.

2.1. The origin and accommodation of strain in heteroepitaxy

The origin of strain in heteroepitaxy is due to the difference in lattice parameters between the two materials and the difference in thermal expansion coefficients [51]. The latter effect is usually much smaller than the lattice parameter effect, and is thus negligible. If a thin epitaxial layer with free lattice parameter a_e is deposited on a substrate with lattice parameter a_s and the lattice parameter difference is accommodated elastically (Fig. 2.1(a)), the elastic mismatch strain ε_0 is given by:

$$\varepsilon_0 = \frac{(a_e - a_s)}{a_s} \qquad (2.1)$$

The lattice constants of Si and Ge at room temperature are 0.5431 nm and 0.5658 nm, respectively, thus corresponds to a total mismatch strain of 4.2%.

The lattice constant of $Si_{1-x}Ge_x$ can be determined by Vegard's law: $a(x) = a_{Si} + x(a_{Ge} - a_{Si})$, however, Dismukes et al. [52] have found a deviation to Vegard's law and their parabolic fitting yields:

$$a(x) = 5.431 + 0.01992x + 0.0028x^2 \qquad (2.2)$$

The large mismatch strain between SiGe and Si can be accommodated by a series of mechanisms, namely: surface roughening, Ge interdiffusion across the SiGe/Si interface and the formation of dislocations.

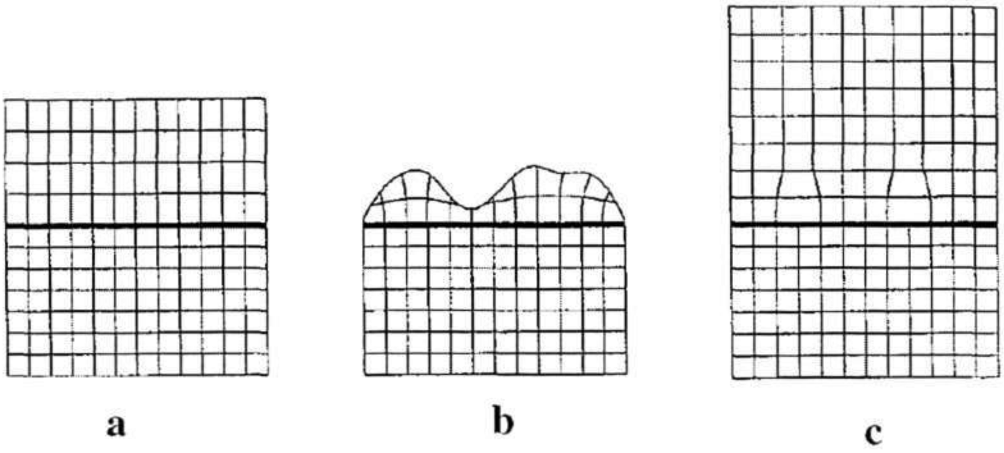

Figure 2.1. Illustrations of (a) fully strained SiGe, (b) relaxation by surface roughening and (c) relaxation by misfit dislocations (after Hull et.al. [53])

Surface roughening in a compressively-strained SiGe on Si produces regions of expansion at the waveform peaks and compression at the waveform troughs (Fig. 2.1(b)). The resultant laterally varying surface strain/stress field may then induce compositional segregation, where Ge atoms are preferentially incorporated at the waveform peaks and Si at the troughs. The development of such surface morphology and compositional segregation requires sufficient adatom mobility of the deposited species on the growth surface. Thus the tendency of such roughening increases with increasing growth temperature and decreasing growth rate, as well as with increasing strain [17, 54]. For sufficiently high surface mobility, the film may grow as a series of discrete islands/clusters. The morphological evolution of these clusters with increasing amount of deposited Ge has been shown to first correspond to pseudomorphic 'hut clusters' with {510} faces, then to the formation of higher aspect ratio pseudomorphic 'domes' with predominant {310} facets and then to dislocated domes [55-58]. Since the roughness of these huts is between 50-70 nm, strain relaxation via surface roughening is not desirable for device applications.

Interdiffusion across the $Si_{1-x}Ge_x$/Si interface increases the thickness of the SiGe epilayer and reduces of average Ge concentration in the resultant $Si_{1-y}Ge_y$ ($y < x$). The mismatch strain between $Si_{1-y}Ge_y$ and Si is smaller than the original strain between $Si_{1-x}Ge_x$ and Si. An extensive study by Van de Walle et al. [59] showed the measured diffusion constant appears to be relatively independent of Ge fraction in the range of x=0.07-0.33. The measured diffusion constants suggest that strain relaxation is not expected to be significant during growth of low Ge fraction and thick SiGe layer on Si at growth temperatures < 800 °C. However, for thin layers, such as SiGe/Si superlattice, this relaxation mode could be more dominant because the activation energy for misfit dislocation formation is much higher [60]. Limited Ge interdiffusion into Si during post-annealing at temperatures > 800 °C might also induce partial strain relaxation [61].

The most widely-studied mode of relaxation is the formation of a misfit dislocations; i.e., missing atomic planes in the film as is shown schematically in Fig. 2.1(c). It is experimentally observed and theoretically predicted that the misfit dislocation array forms only in epitaxial layer thicker than a minimum thickness, known as the critical thickness. Further details on the critical thickness and strain relaxation via misfit dislocations will be presented in the subsequent sections.

2.2. Characteristics of dislocations in SiGe/Si heteroepitaxy

Strain in SiGe/Si heteroepitaxy is relieved by interfacial ***misfit dislocations*** (MD), which propagate by the gliding of ***threading dislocation*** (TD) segments (Fig. 2.2 (a)). In a macroscopically dislocation-free Si substrate, MD nucleation can initiate at local stress concentrations, such as surface steps, facets or local Ge-rich region, all of which are consequences of within-wafer T variations during growth. [58]. Dislocations in FCC crystals glide in {111} planes and in the case of (001) Si wafer, they glide in one of the four possible {111} planes (Fig. 2.2 (b)).

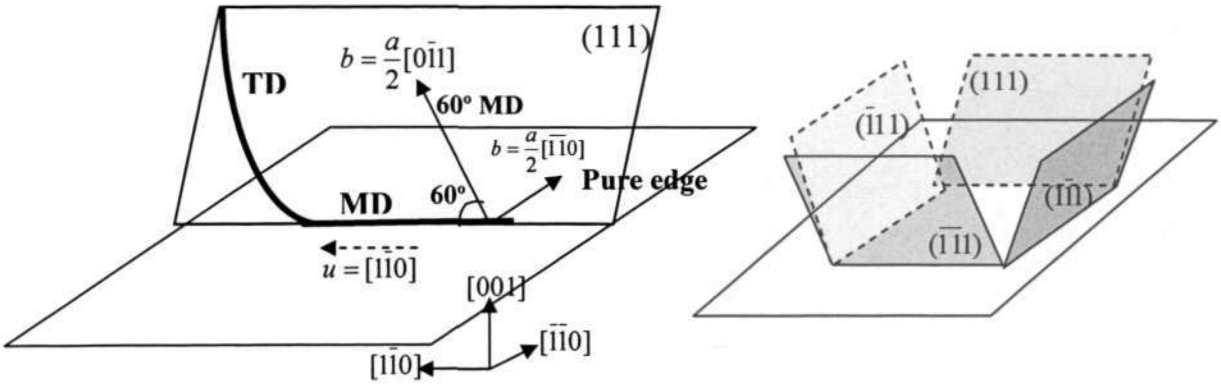

(a) **(b)**

Figure 2.2. Schematic illustration of (a) the geometry of 60° and pure edge dislocations, as well as (b) the four possible glide planes in SiGe layer

There are two common types of MDs in (001) SiGe/Si heteroepitaxy. The first type is known as the 60° dislocation, as the Burgers vector, of the type (a/2) <011>, lies at 60° to the <110> line direction (*u*) and is out of the growth plane. The second type is the pure edge (a/2) <110> dislocation, with Burgers vector lying in the interface at 90° to the line direction. The effective strain relieving component of the MD is given by:

$$\boldsymbol{b}_{eff} = \boldsymbol{b}\cos\theta \qquad (2.3)$$

where θ is the angle between ***b*** and ***u***. From equation (2.3), $\boldsymbol{b}_{eff}$ of a 60° MD is only 50% of the total ***b*** (= 3.9Å). However, because of their ability to propagate rapidly by glide, these are the general total dislocations associated with strain relief in SiGe/Si heterostructures. The pure edge dislocations, on the other hand, are 100% effective at removing lattice mismatch. Since the Burgers vectors do not lie within any glide plane, these defects must move by far slower climb processes.

The formation of pure edge dislocations by reaction of 60° dislocations moving from the same [62-64] and/or opposite [65] directions have been reported to occur by the following reactions or the equivalent reactions with matching Burgers vectors:

$$\frac{1}{2}[10\bar{1}] + \frac{1}{2}[011] = \frac{1}{2}[110] \qquad (2.4)$$

The cross-section and plan-view schematics of the reaction are shown in Fig. 2.3. Since the reactions involve a significant climb, they may be facilitated, but not always necessarily, by Ge/Si interdiffusion [64].

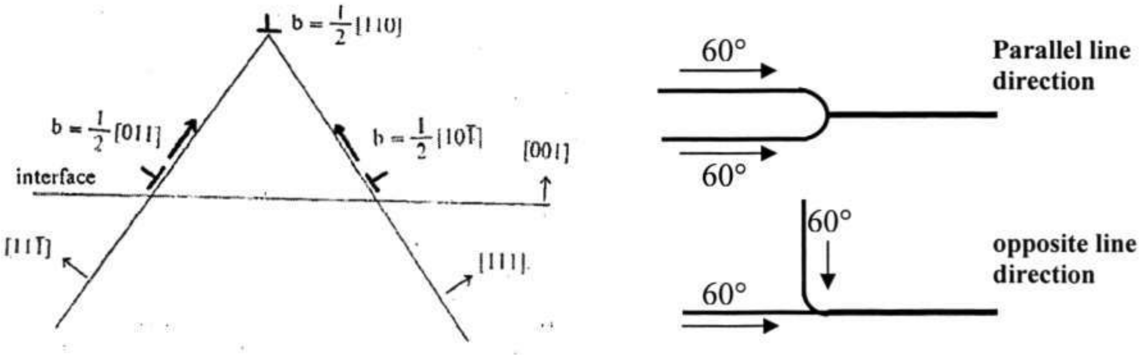

(a) Cross-section **(b) Plan-view**

Figure 2.3. Schematics of the formation of pure edge dislocations by reactions of two 60° MDs in (a) cross-section and (b) plan-view.

Total dislocations may be dissociated into partial dislocations, which are dislocations whose Burgers vector is not a lattice vector. The glide of partial dislocations leave a ribbon of stacking faults, usually in the cubic ABC stacking sequence of atoms along <111> direction. The partial dislocations bounding these stacking faults have Burgers vectors of a/6 <112>, or the Shockley partial. Total dislocations can dissociate if they can lower their energy according to the requirement that $\boldsymbol{b}^2$ is lower after the dissociation than before. For example, the following dissociation reaction is energetically favorable:

$$\frac{1}{2}[110] = \frac{1}{6}[121] + \frac{1}{6}[21\bar{1}] \qquad (2.5)$$

For dissociation from the 60° total dislocation, the two partials have $\theta = 30°$ and $\theta = 90°$, respectively. Since the misfit-releasing burgers vector components of these partials are lower than that of the total dislocations, they are not very effective in releasing mismatch strain.

2.3. Critical thickness and strain relaxation

The critical thickness theories establish a relationship between the strain energy and the dislocation energy. The most intuitive and general critical thickness framework was developed by Matthews and Blakeslee (MB) [6]. Relaxation takes place when the lattice mismatch stress σ_a exerts force on the threading dislocation arms, move the threading dislocation and increase the length of interfacial misfit (Fig. 2.4). The self-energy of misfit dislocation (MD), σ_T, produces a restoring stress/line tension, which acts to inhibit the growth of the MD. In addition, for partial misfit dislocations, there is a restoring force due to the energy of the stacking fault (SF) created by passage of the defects, σ_{SF}. The net stress is thus given by:

$$\sigma_{ex} = \sigma_a - \sigma_T - \sigma_{SF}$$

$$= \frac{2GS\varepsilon(1+\nu)}{(1-\nu)} - [\frac{Gb\cos\phi(1-\nu\cos^2\theta)}{4\pi h(1-\nu)}]\ln(\frac{\alpha h}{b}) - \frac{\gamma}{b} \qquad (2.6)$$

where G is the epilayer shear modulus, S is Schmidt factor, ε is the residual elastic strain, ν is the Poisson's ratio, b is the Burger's vector of MD, ϕ is the angle between the glide plane and interface normal, θ is the angle between Burger's vector and propagation direction, h is the epilayer thickness, α is the factor to account for the dislocation core energy, and γ is the SF energy.

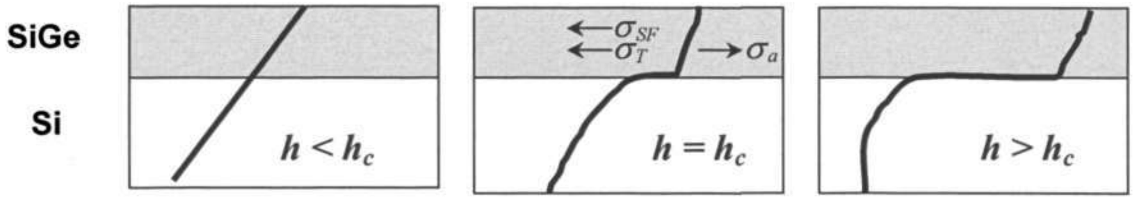

Figure 2.4. Schematic illustrations of the dislocation interaction that forms the basis of MB framework.

The magnitude of critical thickness is found by solving eq (2.6) for $\sigma_{ex} = 0$ and $h=h_c$. For total dislocations where $\gamma = 0$, this yields:

$$h_c = \frac{b(1-\nu\cos^2\theta)\ln(\alpha h_c / b)}{8\pi(1+\nu)\varepsilon\cos\lambda} \qquad (2.7)$$

At increasing $h > h_c$, increasingly larger MD density are favored, and correspondingly smaller amounts of residual elastic strain. For $h > h_c$, the equilibrium residual elastic strain ε_{eq} is found by solving equation (2.6) for $\sigma_{ex} = 0$ and $\varepsilon = \varepsilon_{eq}$. The variation of h_c with Ge concentration according to equation (2.7) is plotted in Fig. 2.5.

When the thickness of the epilayer is within the **stable** region, defined by the MB equation, the epilayer is strained and thermodynamically stable. Nevertheless, kinetic factors, which are not taken into account in the original MB framework, play a major role in defining the rate of introduction of MD. Activation barriers associated with the nucleation and propagation of MD greatly limit the rate of evolution of interfacial MD array at lower growth rates and temperatures [66]. This means that epitaxial layers substantially thicker than the MB thickness can be grown without generation of MD. The variation of critical thickness with growth temperatures is illustrated in Fig. 2.5 and defines the **metastable** region, where strain might be relaxed when sufficient external thermal energy is applied. A useful measure of the degree of metastability was defined by Dodson and Tsao [67], however, accurate prediction is difficult because the energy of dislocation nucleation do not exist due to different nucleation mechanisms (heterogeneous, homogenous and multiplication) [51,53].

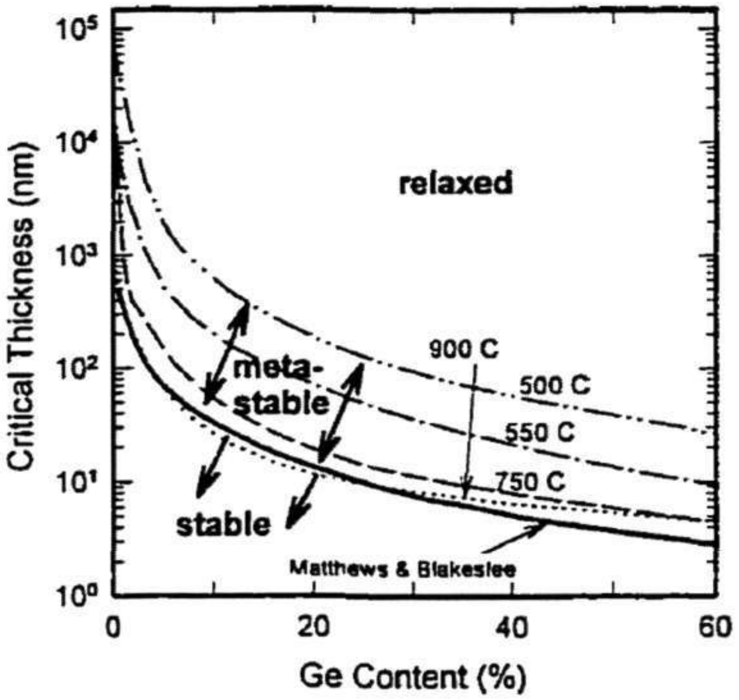

Figure 2.5. Plot of Ge fraction vs critical thickness, showing stable, metastable and relaxed regions of SiGe on Si (from D. Houghton [68]).

2.4. Dislocation nucleation, multiplication and termination

Generally, dislocation behavior in a heteroepitaxy system can be classified into nucleation, multiplication and termination. Dislocations can be nucleated from homogenous and heterogeneous sources. The lowest energy route to misfit dislocation formation is via the glide of preexisting substrate dislocations along the strained interface (homogenous sources) [69], and has been the principle behind the MB critical thickness. However, the dislocation density of the substrates nowadays, which are smaller than $10^5/cm^2$, are not enough to cause relaxation. Thus, relaxation must be facilitated by the multiplication of existing dislocations from heterogeneous sources, such as particulates [70], impurities [71] and stacking faults [72] found on the substrate, are responsible for dislocation nucleation.

Several models for dislocation multiplication have been proposed in the literature, but only three will be reviewed in this chapter: Hagen and Strunk [73], Frank-Read [74] and Modified Frank-Read [75,76] models.

a. Hagen and Strunk [73]

The interaction of two orthogonal 60° MDs (AB and CD) with identical Burgers vectors gliding on two {111} planes can lead to the elimination of the intersection point, resulting in two-L shaped dislocations (Fig. 2.6). One of the L shaped dislocations (AXD) glides towards the surface due to repulsion from the other L shaped dislocations (COB). Upon reaching the surface, AXD split into another 2 threading dislocations, hence the term multiplication.

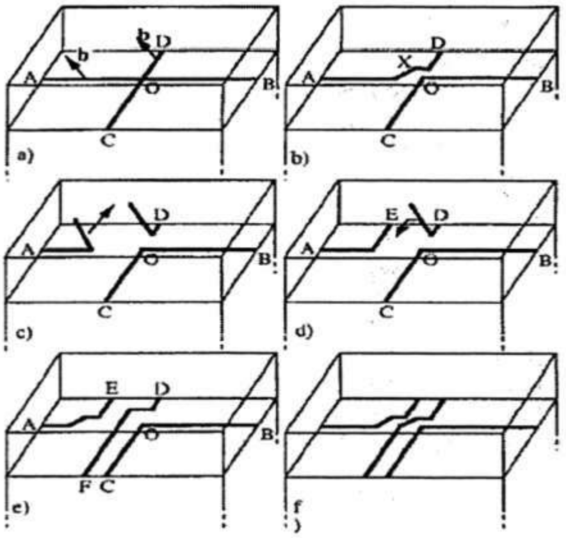

Figure 2.6. Schematic of dislocation multiplication proposed by Hagen and Strunk (after Beanland [77]).

b. Frank and Read [74]

The Frank Read mechanism is a way to generate dislocation starting with a single dislocation pinned at two ends. Possible configurations of Frank and Read sources in thin film are explained in Figure 2.7. First, a threading dislocation lies on its glide plane in segment AB in the layer, pinned at both A and B (a). The misfit stress causes the glissile segment AB to bow out (b). A segment of misfit dislocation is formed and the dislocation loop extends above and below the pinning points (c). The loop pinches off to form a half-loop and the original threading dislocation (d).

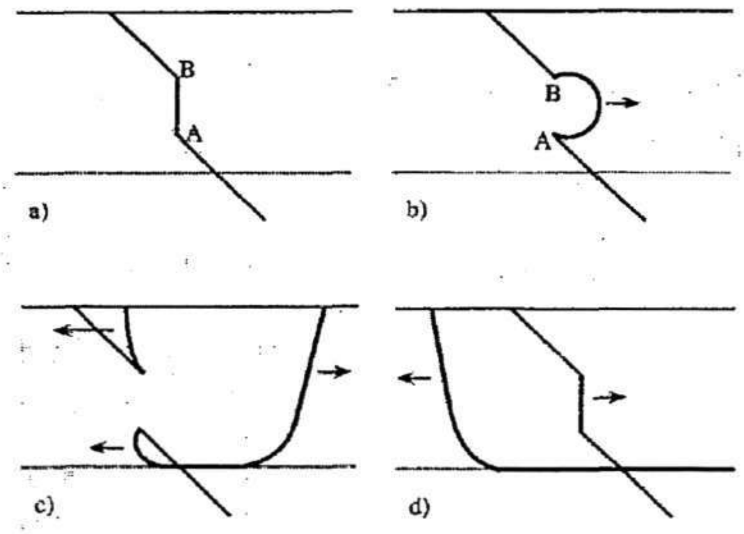

Figure 2.7 Schematic of Frank-Read dislocation multiplication in epitaxial system (after Beanland [77]).

c. Modified Frank-Read [75-76]

LeGoues et al. [75] and Lefebvre et al. [76] observed dislocation loops inside Si substrate that resemble the Frank-Read source. The formation of this loop as proposed by LeGoues et al. [75] is illustrated in Fig. 2.8.

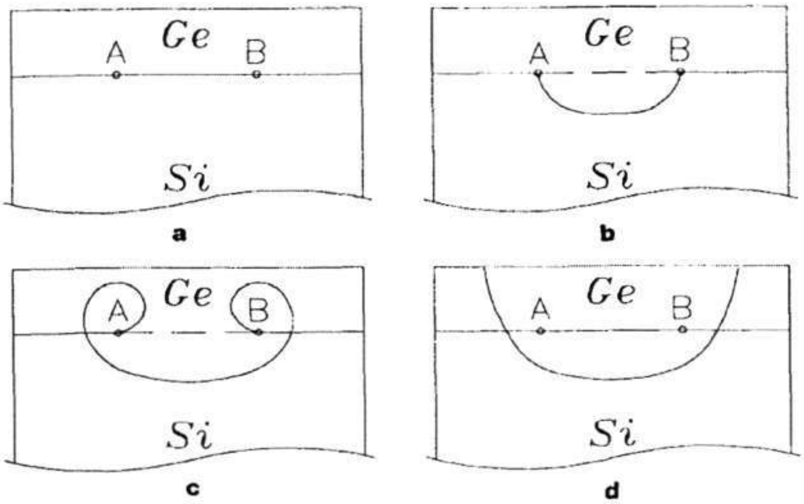

Figure 2.8 Formation of modified Frank-Read loop in SiGe/Si heterostructure (after LeGoues et al. [75]).

A segment of an interfacial dislocation pinned at two nodes by intersecting dislocations is shown in Fig 2.8(a). It will start operating as a Frank-Read source by bowing out into the substrate (Fig 2.8 (b). It will then loop into the Ge thin film until it reaches the surface, becoming in effect a half-loop (Fig. 2.8(c)). The two bowing dislocations formed a closed-loop as the original A-B dislocation and two threading arms are generated (Fig. 2.8(d)). The threading arms then move under the influence of stress and relieve strain.

In addition to dislocation multiplication, dislocation termination is an important phenomenon during the strain relaxation process. A mobile MD can terminate by one of the following mechanisms: a) gliding towards the wafer edge, b) blocking by another MD with similar Burgers vector, and c) annihilation with another MD with opposite Burgers vector. The first mechanism is the most desirable because if all MDs terminate at the wafer edges, in principle, the threading dislocation density will be zero. Nevertheless, it is very difficult, if not impossible, to provide sufficient energy for a dislocation to glide over an 8-inch wafer and assume no blocking by other dislocations.

Interaction with the stress fields of perpendicular misfit dislocations will lead to ‘blocking’ of the threading segment if the layer is thin. Fig.2.9(a) shows the blocking of glissile threading dislocations by MD lying at the interface, and Fig 2.9(b) shows the blocking by MDs lying out of the interface. Since MD propagation is blocked, it is clear that these interactions tend to prevent and even stop strain relief as the MD array increases and the residual strain decreases. It should be noted that, even though the residual strain may be sufficient to create new misfit dislocations, they will only form if there are enough dislocation sources. Both the dislocation blocking and low tendency of new dislocation nucleation are the reasons for the saturation of relaxation in a heteroepitaxy. This phenomenon is often referred to as ***work-hardening***.

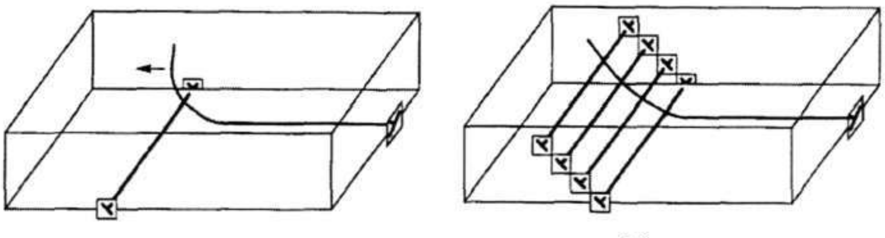
(a) (b)

Figure 2.9 Schematic illustration of dislocation blocking by (a) interfacial MD and (b) out of plane-MDs (after Beanland et al. [78]).

Annihilation of two MDs of opposite Burgers vectors result in a reduction of threading dislocation density because the two TDs react to form a single TD [79-83]. The condition for this annihilation process is that the relative motion between TDs must bring them within a reaction distance. It was shown that possible sources of motion include 'trajectory' motion of TDs with changing thickness [80-82], condensation of point defects at a TD leading to climb [80], and intentional growth of a strained layer [84]. Fig. 2.10(a) shows 2 immobile TDs having opposite Burgers vector when $h < h_c$. For $h > h_c$, it is energetically favorable for the TDs to increase the MD segment length and the TDs may fall within an annihilation radius r_A (Fig. 2.10(b)). The product of annihilation reaction has no threading segments and the resulting MD may have a change in orientation of its line but it must have a single Burgers vector, as shown in Fig. 2.10(c). If the TD segments do not have opposite Burgers vectors, but still have an attractive force, then the two TDs will 'fuse' and the resulting single TD will have a Burgers vector that is the sum of the Burgers vectors of the reacting TDs. Even though increasing thickness may promote TD annihilation, the final TDD is still considerably high (10^6-10^8/cm^2) [78]. Thus, to further reduce the TDD, various buffer layer methods have been proposed and the review is summarized in the next section.

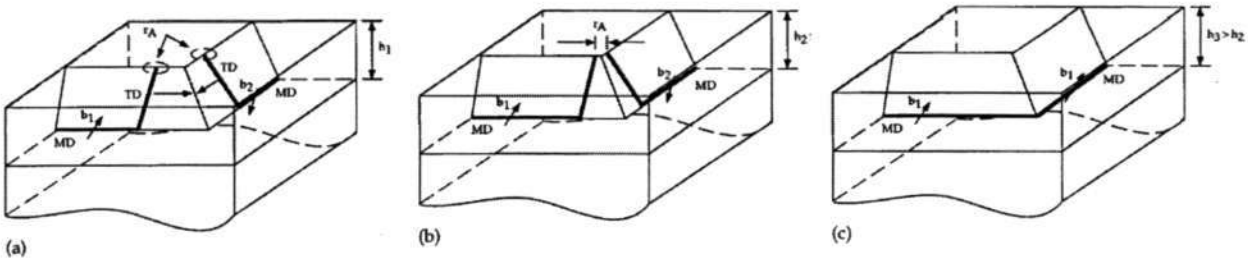

Figure 2.10 Schematic of motion and annihilation of TDs in heteroepitaxy (after Romanov et al. [84]).

2.5. Buffer layer methods for defect engineering

In this section, some of the most successful buffer layer methods are reviewed. Table 2.1 shows the comparison of the epitaxial quality of strained layer superlattice, low-T Si buffer, H^+ or He^+ implantation and forward graded SiGe buffer layers.

Table 2.1 A summary of widely-studied buffer layer concepts.

Method	Schematic	TDD (cm^{-2}) for x= 0.3	Roughness (nm)	thickness (nm) (Buffer+SiGe)
Strained Layer Superlattice [26-28]	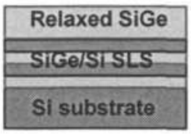	10^5 - 10^6	NA	< 1000
Low T-Si buffer [29-31]	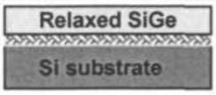	10^6 – 10^7	1-1.5	450-760
H^+ or He^+ implant + anneal[32,33]	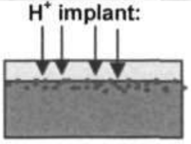	< 10^7 (for x<0.22)	NA	250
Forward Graded [34,35]	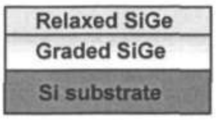	10^5 - 10^6	10-25	> 3000

a. Strained Layer Superlattice (SLS)

One of the earliest methods to reduce TDD is strained-layer superlattices (SLS), which consist of alternating layers of larger and smaller lattice constant material grown pseudomorphically on the substrate. The strain field inside SLS causes TDs to bend and form hair-pin dislocations which glide laterally and create dislocations at both interfaces of that layer in the superlattice. The advantage of SLS is the thickness is less than 1 μm, however, theoretical calculations show that the SLS is not effective in reducing TDD to lower than $10^6/cm^2$ [28].

b. H^+ implant and post-deposition anneal

H^+ or He^+ implantation below the uniform SiGe layer, followed by annealing, and subsequent strained Si epitaxial growth, make use of the defective region as a sink for the misfit pileup [32-33]. The high concentration of point defects brings the TDs within the annihilation radius, and thus increases the annihilation process. However, the high TDD of $10^7/cm^2$, and the defective region may increase substrate leakage current and affect the device performance.

c. Low-temperature Si buffer layer

A low-temperature Si buffer layer grown below the SiGe epilayer produces a high density of point defects because surface atom migration is significantly restricted during low temperature growth [29]. The method is effective in producing TDD on the order of $10^6/cm^2$. It was proposed that more effective TDD annihilation processes is a result of TDs being closer to each other and/or the enhancement of TD glide velocity [25]. However, the slow growth rate renders this technique less attractive for actual device manufacturing.

d. Forward graded SiGe buffer layer

Fitzgerald et al. [34] pioneered the use of a compositionally graded buffer layer, in which Ge concentration increases gradually, to grow relaxed SiGe film with a TDD of 10^5 /cm^2. The interfaces within the graded layer provide evenly-distributed MD nucleation sites and the residual strain [48, 86] increases the MD glide and blocks the upwards propagation of TD. LeGoues et al. [75] first discovered that MDs are multiplied by a modified version of Frank-Read sources and the loops propagate into the Si substrate. This multiplication mechanism greatly reduces the TDD in the SiGe layer. Furthermore, LeGoues [87] observed the TD annihilation mechanisms due to the zigzag network of dislocations, shown schematically in Fig. 2.11.

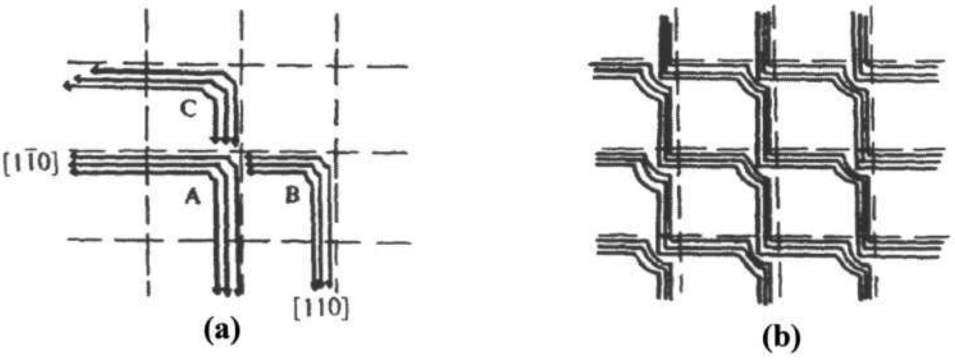

(a) (b)

Figure 2.11. Threading dislocation annihilation by zigzag motion of neighboring misfit dislocations (after LeGoues [87])

Assuming misfit dislocations first nucleate at A and are able to travel a long distance because there are few dislocations to pin it then no strain will be released. When source B generates misfit dislocations, the threading arms moving along the [1$\bar{1}$0] meet a huge obstacle at A. If both dislocations have opposite Burgers vectors, they will attract each other. Furthermore, in order to move past A, the dislocations nucleated at B have to glide to an area that is already relaxed. This would require a huge energy. On the other hand, these dislocations can cross-slip toward C, since this region is not relaxed yet. Each dislocation moving from C in the [110] direction encounters a matching thread, coming from B. The two threads are attractive because they have antiparallel Burgers vectors, and as a result the threading arms cancel out.

Even though the forward graded method has been considered one of the most successful and widely accepted, up to 5 μm-thick buffer layer is needed to grow a high quality SiGe layer. Earlier studies have found that the self-heating effect of a device on a relaxed SiGe buffer is proportional to the square root of the buffer thickness [36-37]. The limitation of this method will be further explained in Chapter 6.

2.6. SiGeC/SiGe heteroepitaxy

The SiGeC ternary system was originally proposed as a method to reduce compressive strain in SiGe/Si heteroepitaxy. Since carbon (a = 3.567 ´ , space group: Fd-3m) is smaller than Si and Ge, when incorporated in the substitutional sites, it reduces the intrinsic lattice constant [88,89]. Assuming a linear dependence of the intrinsic lattice constant $a_0(x,y)$ of $Si_{1-x-y}Ge_xC_y$ on the composition x and y between Si, Ge and diamond, one gets the following relationship:

$$a_0(x,y)=a_{Si}+(a_{Ge}-a_{Si})x+(a_C-a_{Si})y \tag{2.8}$$

where a_C is the lattice constant of diamond. Based on this linear interpolation it turns out that the compressive strain of 8.2% Ge can be compensated by 1% C in a pseudomorphic $Si_{1-x-y}Ge_xC_y$ layer on Si substrate [88].

The annealing behavior of SiGeC layers and superlattice structures have been investigated in the temperature range from 750 to 900 °C [90] and between 1000 and 1130 °C [50]. Plastic relaxation of SiGeC is retarded because of the dislocation pinning effect of C. However, C strongly increases the interdiffusion of Ge in Si [90-91]. For annealing temperatures at above 900 °C, the substitutional C diffuses and forms β-SiC precipitates [49-50]. Prior to the β-SiC precipitation, C diffusion via interstitials has also been reported [92-93].

Despite having a lot in common with SiGe, there are few reports of the use of SiGeC as buffer layers of relaxed SiGe. A relaxed SiGe with TDD below $10^5/\text{cm}^2$ was grown on a stepwise graded buffer based on a combination of SiGe and SiGeC [94]. This method relies on the retardation of dislocation glide in SiGeC because of the very strong local strain fields around the individual C atoms [95]. Delhougne et al. [96] inserted a 10 nm SiGeC layer between two layers of $Si_{0.78}Ge_{0.22}$ to provide a dislocation-nucleation site, and 83% relaxation was achieved after annealing. TDD was estimated to be ~ $10^6/\text{cm}^2$ from TEM observation. β-SiC was detected by FTIR but was not associated with the strain relaxation mechanism. Even though the precipitation of a new phase is often associated with coherency strain [97], it has not been taken into consideration. Furthermore, during the loss of coherency new dislocations might form [97], however, comprehensive study on the effect of β-SiC on dislocation behavior is not available. Obviously, the potential of SiGeC layer as a buffer layer has not been fully exploited.

Chapter 3:

Experimental Techniques

This chapter contains a brief summary of the Low-Pressure CVD and emphasizes on the characterization techniques used in this thesis. Characterizations of a heteroepitaxy system include strain quantification techniques, chemical analysis techniques, and epitaxial quality characterizations. More emphasis will be given on High-Resolution XRD (HR-XRD), Raman spectroscopy, and Transmission Electron Microscopy (TEM), which were used extensively in this project.

3.1. Low-Pressure Chemical Vapor Deposition (LP-CVD)

Chemical Vapor Deposition (CVD) is the process of *chemically* reacting a volatile compounds to be deposited with other gases, to produce a nonvolatile solid that deposits epitaxially on a suitably placed substrate. The basic sequential steps that occur in every CVD process are sketched in Fig. 3.1 and include:

a. Introduction of gases from the gas inlets into the reaction zone,
b. Chemical reactions in the gas phase to produce new reactive species and by-products,
c. Transport of gas to substrate,
d. Deposition of film: - adsorption (chemical and physical) of gas on substrate
  - diffusion of these species on the substrate
  - heterogeneous reactions leading to film formation,

e. Desorption of by-products, and

f. Removal of by-products

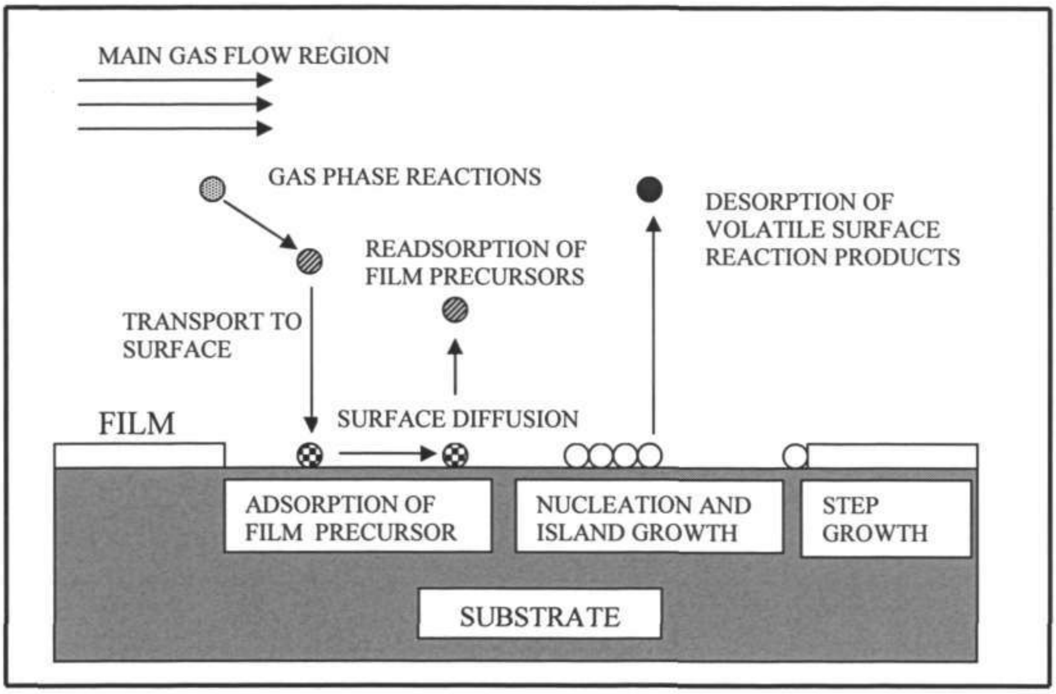

Figure 3.1. Sequence of gas transport and reaction processes contributing to CVD film growth (after Hitchman and Jensen [98]).

There are six main reactions that can occur during CVD deposition, depending on the types of source, i.e., pyrolysis, reduction, oxidation, compound formation, disproportionation, and reversible transfer. In the case of CVD for epitaxial film growth, the relevant mechanisms are pyrolysis and reduction. Pyrolysis involves the thermal decomposition of such gaseous species as hydrides, carbonyls, and organometallic compounds on hot substrates. Decomposition of silane into silicon and hydrogen is one example:

$$SiH_4(g) \rightarrow Si(s) + 2H_2(g) \qquad (650°C) \qquad (3.1)$$

The reactions commonly employ hydrogen gas to effect the reduction of oxygen-containing compounds. An important example is the reduction of $SiCl_4$ on single crystal Si wafers to produce epitaxial Si films according to the reaction:

$$SiCl_4(g) + 2H_2(g) \rightarrow Si(s) + 4HCl(g) \qquad (1200°C) \qquad (3.2)$$

The CVD system used in this project is the Low Pressure CVD (LPCVD). Lowering the pressure helps to increase the growth rate since pressure is inversely proportional to the gas diffusivity, according to the classical gas theory $D \approx T^{3/2}/P$. Low gas pressures enhance the mass flux of gaseous reactants and products through the boundary layer between the laminar gas stream and substrates. In particular, LPCVD is beneficial for low-T growth processes where the growth rate is usually slow. To compensate for low pressures of operation, the input reactant gas concentration must be correspondingly enriched to maintain comparable deposition rates.

A silicon epitaxial layer is usually grown from one of three precursors: SiH_2Cl_2 (DCS), SiH_4 (silane) or Si_2H_6 (disilane). The highest quality epitaxial layer is achieved by disilane, however, silane and DCS are more commonly used due to economical reasons. Silane exhibits higher growth rate than DCS. The precursors of SiGe layer are GeH_4 (germane) or Ge_2H_6 (digermane) and either silane, disilane or DCS.

The most widely adopted model for SiGe epitaxy from silane and germane precursors is [99]:

$$x/1\text{-}x = m\,(F(\mathrm{GeH_4})/F(\mathrm{SiH_4})) \qquad (3.3)$$

When DCS is used instead of Silane, the model becomes [110]:

$$x^2/1\text{-}x = m\,(F(\mathrm{GeH_4})/F(\mathrm{Si_2Cl_2})) \qquad (3.4)$$

where x is the germanium fraction, m is the pressure and T dependent constant, and $F(\mathrm{GeH_4})$ and $F(\mathrm{SiH_4})$ are the partial pressures of germane and silane respectively.

3.2. Strain Quantification techniques

Several techniques can be used to calculate strain in a heteroepitaxy system. The most-widely used are Raman spectroscopy, HR-Xray Diffraction (HR-XRD) and TEM techniques, namely Convergent Beam Electron Diffraction (CBED) and HR-TEM image processing. A comparison of these techniques is summarized in Table 3.1.

Table 3.1. Comparison of heteroepitaxy strain-measurement techniques

Parameter	Micro-Raman	HR-XRD/RSM	CBED	HRTEM image processing
What is measured	Raman shift	d_{hkl}	HOLZ line shift	Lattice spacing of Inverse Fast Fourier Transform
Precision	1E-5	1E-6	1E-4	1E-4
Depth resolution	20nm – 2 µm	10 µm	200 nm	< 100 nm
Lateral resolution	0.8 x 0.8 µm	100 nm x 50 µm	10 x 10 nm	2 nm
Sample preparation	none Non destructive	None Non destructive	0.5 day Destructive	0.5 – 1 day destructive
Measurement time	30 sec/point	15 – 30 mins	0.5 day	0.5 day
Data analysis	< 15 mins	< 15 mins	1 day	1 day
Good for	Fast data validation/ process monitoring	Accurate measurement for new process (blanket)	Accurate measurement of localized strain	Qualitative measurement of localized strain

The most precise technique is HR-XRD, with an accuracy of 10^{-6}, 4 orders magnitude smaller than the typical strain quantity (10^{-2}). However, its poor depth resolution makes it less suitable for strain measurement of thin heteroepitaxial layers. Raman spectroscopy offers a good compromise between measurement precision and depth resolution. Its lateral resolution is also sufficient for patterned structures. The TEM methods are presently the only ones known to measure localized strain in the channel, usually induced by a physical compression or tension from structures in close proximity, such as a silicon nitride etch stop layer, shallow trench isolation (STI) and SiGe source/drain [100-102]. Unfortunately, the poor precision, tedious sample preparation and complicated data analysis make the TEM methods less effective for regular analysis or process monitoring. Since all of the samples in this project are blanket wafers, strain measurements were performed by Raman and HR-XRD. The working principles and quantification procedures are presented in the following sections.

3.2.1. Raman spectroscopy

a. General introduction on Raman spectroscopy

When a sample is irradiated by intense laser beams with frequency of υ_o, the scattered light can be scattered elastically ($\upsilon_i = \upsilon_o$) and inelastically ($\upsilon_i = \upsilon_o \pm \upsilon_m$). The inelastic scattering process is called the Raman effect and υ_m is the vibrational frequency of a molecule that absorbs part of the incoming frequency. The υ_o - υ_m and $\upsilon_o + \upsilon_m$ lines are called the Stokes and anti-Stokes lines, respectively [103]. Thus in Raman spectroscopy, we measure the vibrational frequency (υ_m) as a shift from the incident beam frequency (υ_i).

Not all materials can scatter light inelastically, hence not all materials are Raman-active. The Raman selection rule states that if there is a change in polarizability during vibration, then Raman scattering takes place. Usually materials with covalent bond and/or a center of symmetric vibrations are Raman active. The polarization selection rules for back scattering of Si from (001) and (110) surfaces are given in Table 3.2. This table shows that only the z-polarized phonon can be observed for back-scattering from a (001) surface.

Table 3.2. Polarization selection rules for back scattering from a (001) and (110) surface (after I. De Wolf [104]).

Polarization		Visible		
e_i	e_s	R_x	R_y	R_z
Back scattering from (001)				
(100)	(100)	—	—	—
(100)	(010)	—	—	x
(1-10)	(1-10)	—	—	x
(110)	(1-10)	—	—	—
Back scattering from (110)		—	—	x
(1-10)	(001)	x	x	—
(1-10)	(1-10)	—	—	x
(001)	(001)	—	—	—

Fig 3.2 is the typical Raman spectrum obtained for strained Si samples grown on 1 µm thick of $Si_{0.75}Ge_{0.25}$ buffer layer and 2-µm thick of graded SiGe layer. The x axis is the wave number (ω) which is related to Raman frequency (υ) by $\omega = \frac{\upsilon}{c}$, where c is the velocity of light.

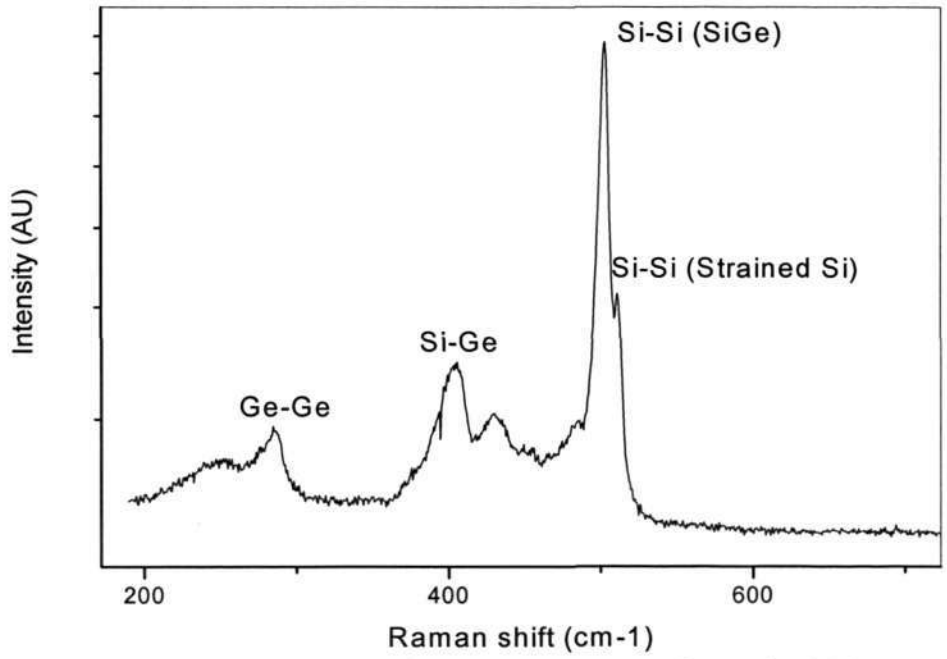

Figure 3.2. Typical Raman spectra of a strained Si

The three strong first order lines in this spectrum are due to nearest neighbor Ge-Ge (288.44 cm^{-1}), Si-Ge (406.64 cm^{-1}) and Si-Si from SiGe layer (502.02 cm^{-1}) atomic vibrations. Another peak at 511.26 cm^{-1} is the Si-Si vibration of the strained Si layer. The

Si-Si vibration peak is relatively weaker than the other as the thickness of the layer is much smaller than the extinction length of the laser wavelength in silicon. There are a few smaller peaks between Si-Ge and Si-Si vibration peaks, which can be explained in terms of localized Si-Si optical modes surrounded by an increasing number of Ge atoms [111].

b. Effect of stress on Raman frequency

Mechanical strain or stress may affect the frequencies of the Raman modes and lift their degeneracy. The wave numbers of the optical modes in the presence of strain can be obtained by solving the following secular equation [105,106]:

$$\begin{vmatrix} p\varepsilon 11+q(\varepsilon 22+\varepsilon 33)-\lambda & 2r\varepsilon 12 & 2r\varepsilon 13 \\ 2r\varepsilon 12 & p\varepsilon 22+q(\varepsilon 33+\varepsilon 11)-\lambda & 2r\varepsilon 23 \\ 2r\varepsilon 13 & 2r\varepsilon 23 & p\varepsilon 33+q(\varepsilon 11+\varepsilon 22)-\lambda \end{vmatrix} = 0 \qquad (3.5)$$

where p,q and r are the phonon deformation potentials, and ε_{ij} are the strain tensor components. The difference between the Raman frequency of each mode in the presence of stress, ω_j (j = 1,2,3) and in the absence of stress, ω_{j0} , can be calculated from the eigenvalues λ_j :

$$\Delta\omega j = \omega j - \omega jo \approx \frac{\lambda j}{2\omega jo} \qquad (3.6)$$

The polarization direction of each mode, in the presence of stress, is described by the corresponding eigenvectors of the secular equation. The strain tensor components are calculated using Hooke's law and give $\varepsilon_{11} = S_{11}\sigma$, $\varepsilon_{22} = S_{12}\sigma$ and $\varepsilon_{33} = S_{12}\sigma$, where S_{ij} are the elastic compliance tensor elements of Si. In the case of biaxial stress in the x-y plane, with stress components σ_{xx} and σ_{yy}, solving equation (3.5) and (3.6) leads to:

$$\Delta\omega_3 = \frac{1}{2\omega_0}[pS_{12} + q(S_{11} + S_{12})](\sigma_{xx} + \sigma_{yy}) \tag{3.7}$$

This is the only active Raman mode for back scattering from a (001) Si surface (Table 3.2). From this equation it follows that compressive biaxial stress will result in an increase in Raman frequency, while tensile stress will cause a decrease.

c. Raman spectroscopy instrumentation

The details on how Raman spectroscopy works is explained in Fig 3.3: when a laser hits the sample, the collision generates molecular vibration and energy is emitted in the form of light. The light coming from the inelastic scattering is transmitted through a filter, while the light coming from the elastic scattering is eliminated. The filter recognizes the inelastic light since its energy is much lower than the elastic one. The spectrometer/diffraction grating disperses the light onto a detector to generate the Raman spectrum.

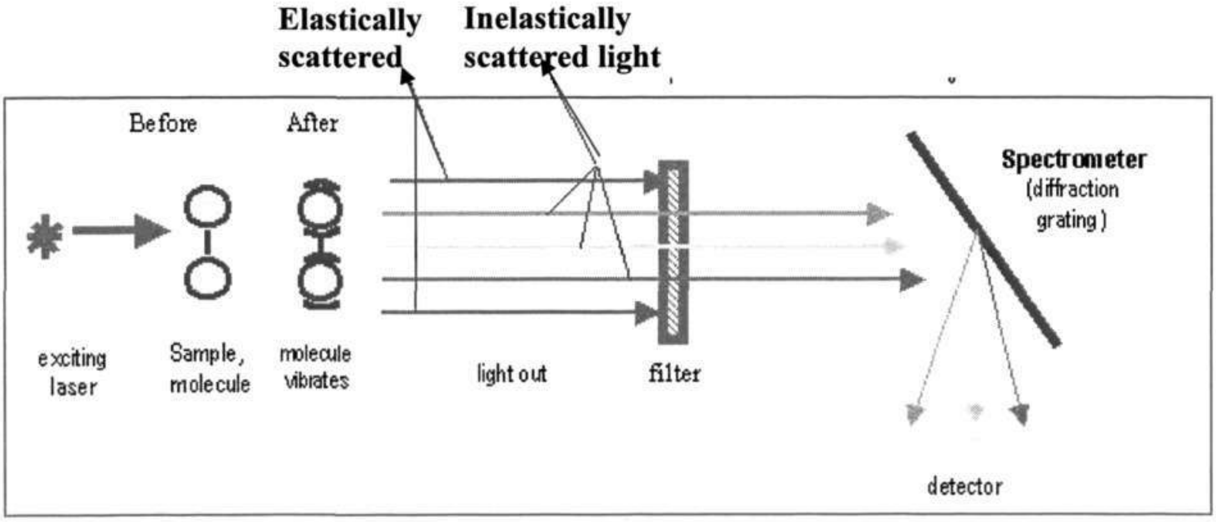

Figure 3.3. Schematic of the working principle of Raman spectroscopy.

The depth resolution of a Raman spectra is determined by the penetration depth of the laser wavelength. In general, a shorter wavelength results in a shallower penetration depth and is desirable for strain measurement of thin heteroepitaxy. For details of the relationship between penetration depth and laser wavelength, please refer to Appendix A. A Jobin Yvon T64000 triple-grating micro Raman system with a 514.5 nm line from an-argon ion laser was used in this project.

3.2.2. High Resolution X-Ray Diffraction

a. Bragg's law

Figure 3.4 illustrates the scattering of X-rays as it strikes atoms of a crystal.

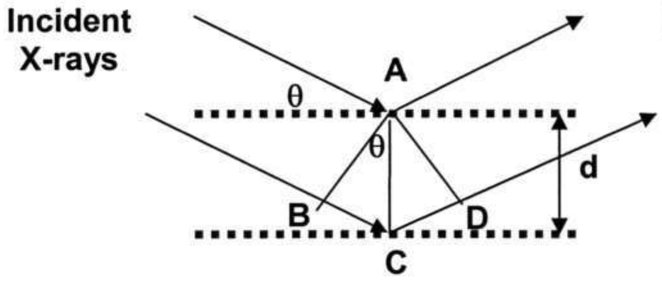

Figure 3.4. X-ray scattering in a crystal.

From the left rectangle, it is clear that: BC = d sin θ . If the emerging X-rays are in phase, the phase difference, nλ = BC + CD. Since BC = CD, nλ = 2BC. Substitutions lead to the Bragg's law:

$$2d_{hkl} \sin\theta = n\lambda \quad , \tag{3.8}$$

where d_{hkl} is the lattice spacing of plane (hkl), θ is the angle of incidence, n is an integer and λ is the X-rays' wavelength. The objective of an XRD experiment is to obtain d_{hkl} and calculate the cubic lattice parameter a, b, c by the following relationship:

$$\frac{1}{d^2} = \frac{h^2 + k^2 + l^2}{a^2 + b^2 + c^2} \tag{3.9}$$

b. Diffraction and reciprocal lattice

The diffraction of either photons or electrons (sometimes neutrons) is one of the most powerful techniques for surface structure determination. Unfortunately, the diffraction pattern is not a direct representation of the real-space arrangement of the atoms in a solid or on a surface. The most convenient way to link the real structure of the material to its diffraction pattern is through the reciprocal lattice. In real space, the lattice points represent the atomic arrangement within the crystal structure. In the reciprocal space, each point in the lattice represents a set of planes of the crystal (Fig. 3.5).

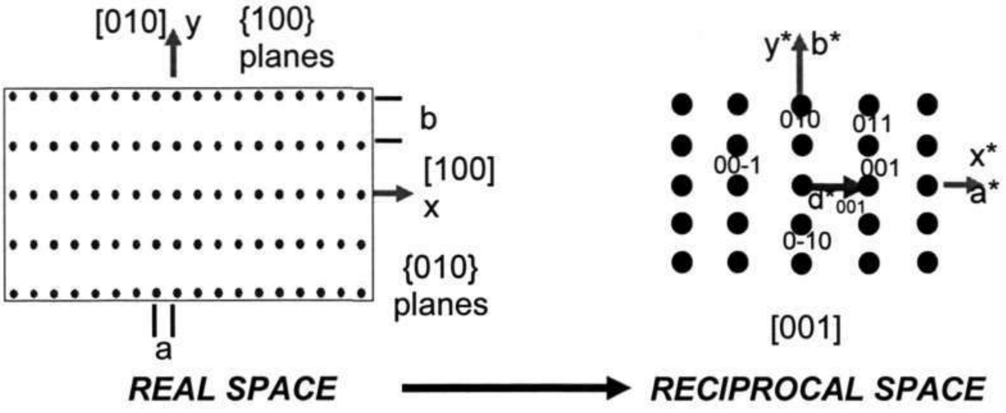

Figure 3.5. A crystal lattice representation in real and reciprocal space viewed from z axis.

In a real XRD experiment, diffraction can occur from crystal plane if the following criteria are satisfied:

1. The wavelength of the X-Ray source must be on the order of d_{hkl}, and in this case, a Cu source (λ=1.54 ′) was used.
2. The incident X-ray angle must be similar to the diffraction angle for the particular plane, which can be determined by Bragg's law.

3. The structure factor of the sample determines which planes will result in constructive interference. Both Si and SiGe have the diamond crystal structure (Fd-3m), which consists of two interpenetrating face center cubic sub-lattices. The structure factor of FCC is given as:

$$F_{hkl} = f[e^0 + e^{\pi i(h+k)} + e^{\pi i(h+l)} + e^{\pi i(k+l)}] \qquad (3.10)$$

   Therefore, planes that can contribute to constructive interference are those where h,k,l are *all even* or *all odd*. Another condition is (h=2n+1) or (h+k+l=4n), and where n is an integer.

Based on the above criteria and taking a Si wafer with an (001) surface, the accessible reciprocal space region in an HR-XRD experiment is shown as the white area in Fig. 3.6. In a HR-XRD rocking curve experiment, only 1 specific plane is diffracting at any one time, and the X-ray incident angle and the detector positions are fixed around a pre-determined angle to satisfy Bragg's law.

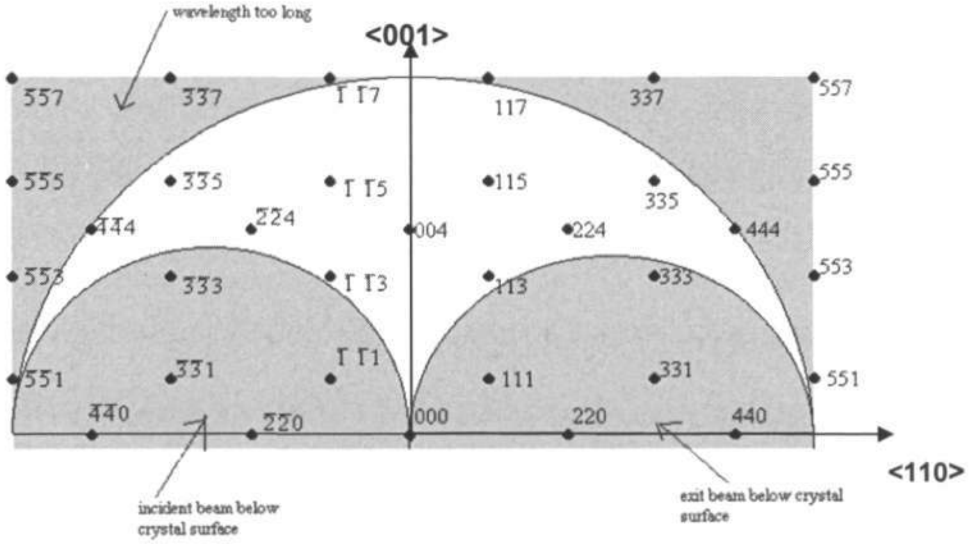

Figure 3.6. Accessible region in the Reciprocal space of Si in a typical HR-XRD experiment.

c. HR-XRD instrumentation

In principle, the differences between a conventional XRD and HR-XRD set-up are the following:

1. In a powder-diffraction experiment, the incident beam and detector are rotated, while the sample is fixed. In a HR-XRD, the incident beam is fixed at a certain angle, the sample is 'rocked' around that angle, and the detector follows the rotation of the sample.
2. HR-XRD uses a special beam conditioner that produces highly monochromatic X-ray source by controlling the divergence and wavelength spread via a combination of diffracting elements.
3. HR-XRD uses a high precision goniometer stage that allows fine rotation of 0.01°.

Figure 3.7 shows the set-up of a HR-XRD triple-axis instrument [107]. The first axis controls the beam conditioner, the second controls the specimen, and the third controls the analyzer. The detector measures the intensity scattered by the specimen over its acceptance angle. The analyzer is another series of reflections by crystals which further restrict the acceptance angle of the detector. The reduced acceptance increases the detector's sensitivity to the diffracting characteristics of the specimen. This enables determination of strain and mismatch from tilt or mosaic spread.

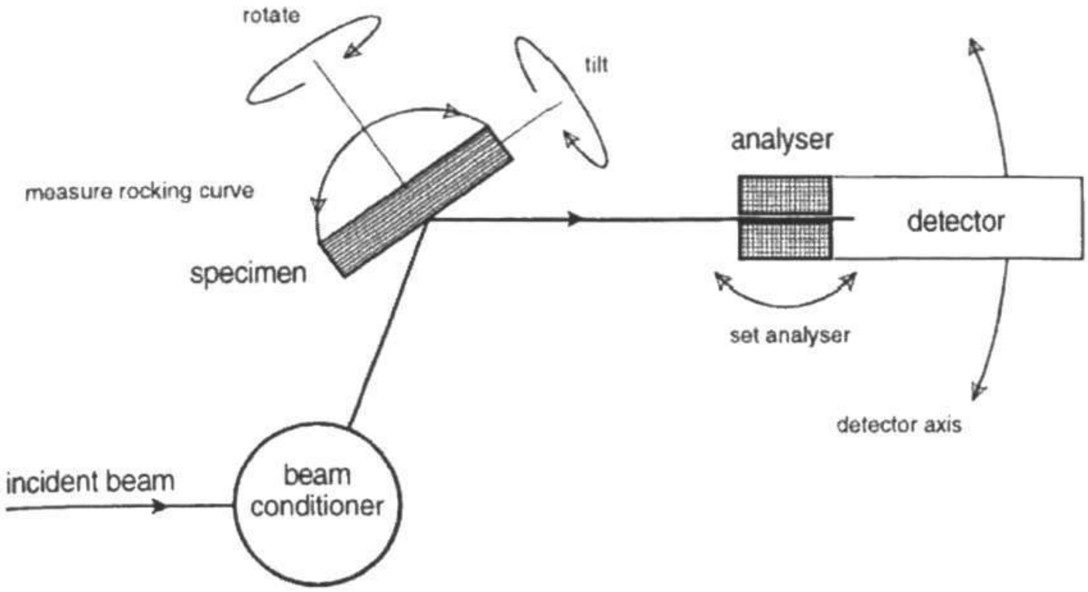

Figure 3.7. Triple-axis HR-XRD set-up (after Bowen and Tanner [107]).

d. Strain calculation from Reciprocal Space Map (RSM)

Figure 3.8 illustrates the RSM around (004) and (224) reflections for fully strained and fully relaxed SiGe on Si sample. The arrow in the RSM schematic shows the movement of SiGe reflections as relaxation increases. The shaded-oval is the reflection of a graded SiGe.

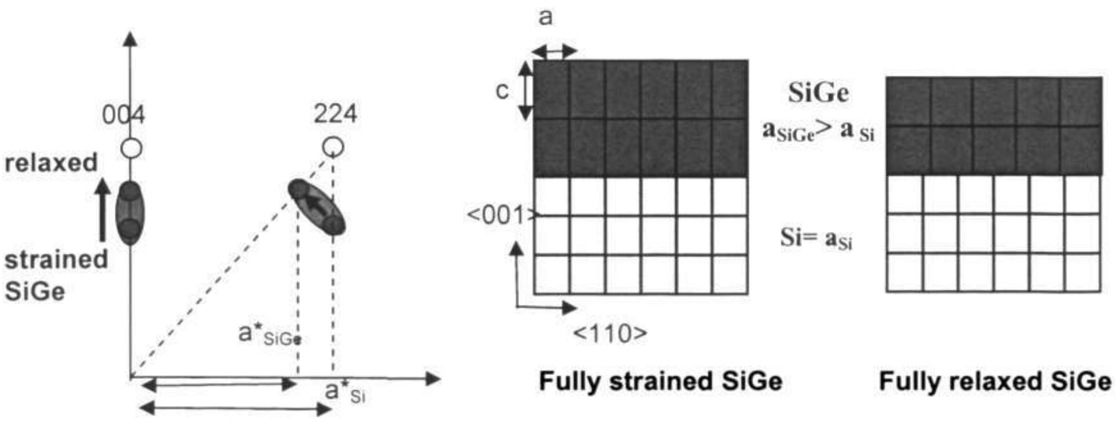

Figure 3.8. Illustration of (004) and (224) reflections of fully strained and fully relaxed SiGe in RSM and real-lattice.

Since reciprocal space is inversely-proportional to the real space, the reciprocal lattice parameters a^*_{Si} and a^*_{SiGe} are the ratio of the real lattice parameters a_{Si} and a_{SiGe}. The following equations give the ratio of a and c parameters:

$$a_{SiGe} = \frac{a^*_{Si}}{a^*_{SiGe}} a_{Si} \qquad c_{SiGe} = \frac{c^*_{Si}}{c^*_{SiGe}} c_{Si} \tag{3.11}$$

For a partially-strained SiGe with lattice parameters a_T and c_T, there is an equivalent lattice constant a_L assuming the SiGe is fully relaxed:

$$a_L = c_T\left[1 - \frac{2v(c_T - a_T)}{(1+v)c_T}\right] \tag{3.12}$$

where v is the Poisson ratio of SiGe (v = 0.28). The Ge concentration, *x*, can be determined by solving the quadratic equation:

$$a_L = 0.028x^2 + 0.2x + 5.431 \tag{3.13}$$

The amount of relaxation is defined as the ratio of the strain of the partially-strained sample, $f_{//}$, by the total strain if the layer is fully relaxed f_m. The expression for Relaxation (R) is given in the following equations:

$$fm = \frac{a_L}{a_{Si}} - 1 \tag{3.14}$$

$$f_{//} = \frac{a_T}{a_{Si}} - 1 \tag{3.15}$$

$$R = \frac{f_{//}}{f_m}.100\% = \frac{a_T - a_{Si}}{a_L - a_{Si}}.100\% \tag{3.16}$$

e. Strain calculation by (004) and (224) rocking curves

A rocking-curve is a 1-dimensional-version of RSM, as shown in Fig. 3.9.

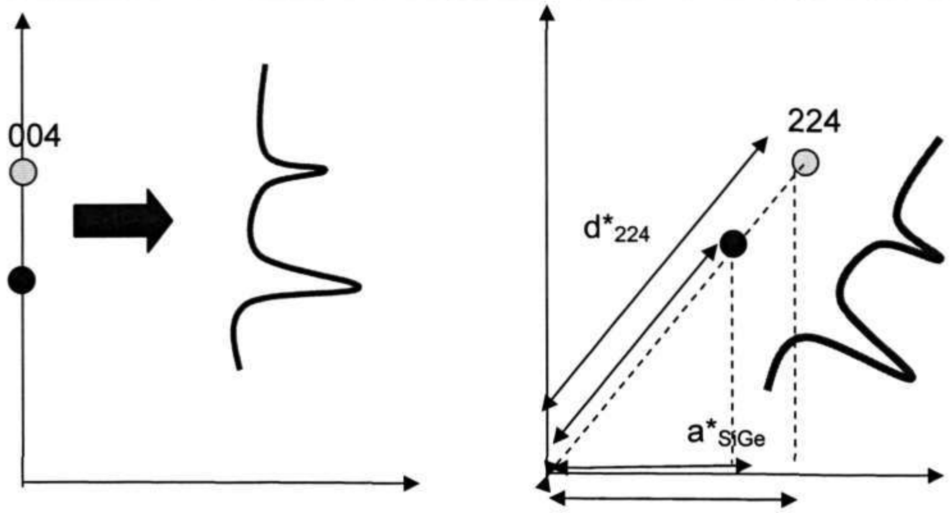

Figure 3.9. (004) and (224) Rocking curves from their respective Reciprocal Space Map.

Since the (224) rocking curve only represents the lattice spacing of the (224) planes, the (004) scan is necessary to determine c_{SiGe}. Fig. 3.10 shows the rocking curve of (004) scan with SiGe and Si reflections. The experimental X-ray mismatch is given by [107]:

$$m^* = \frac{\Delta d}{d_{Si}} = \frac{\Delta\theta}{\theta_{SiGe}} \tag{3.17}$$

c_{SiGe} is calculated by the following relationship:

$$c_{SiGe} = (1 + m^*)c_{Si} \tag{3.18}$$

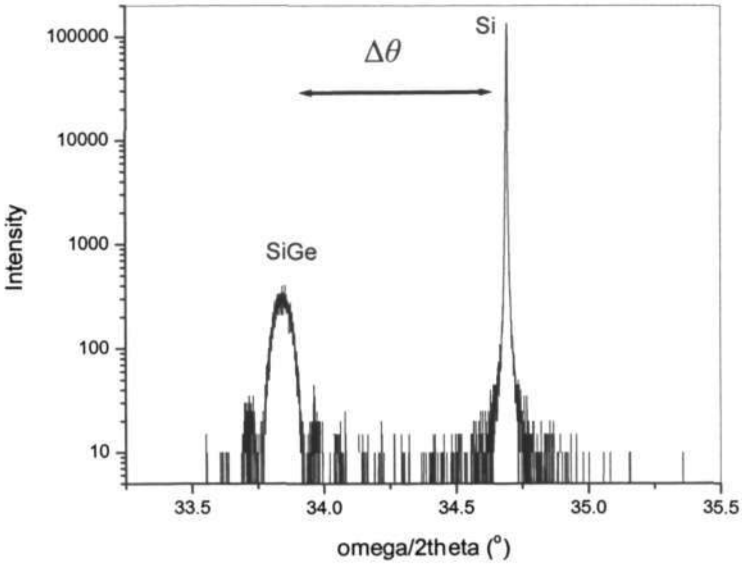

Figure 3.10. (004) Rocking curve with SiGe and Si reflections.

A similar procedure was carried out for (224) rocking curve to obtain a_{SiGe}. The Ge content and relaxation value can then be calculated.

3.3. Chemical characterization techniques

Even though HR-XRD can determine the amount of Ge, it is often necessary to have an independent chemical analysis, for example to determine the Ge profile in a graded layer or Ge diffusion after thermal annealing. The chemical analysis techniques used in this project are Rutherford Backscattering Spectroscopy (RBS), Secondary Ion Mass Spectroscopy (SIMS) and Auger Electron Spectroscopy (AES). A comparison of the performance of each technique is given in Table 3.3. RBS is most suitable for determining the Ge profile in a novel graded layer due to its excellent accuracy and depth resolution. After calibration, AES is a very convenient tool to detect Ge diffusion after annealing, while dynamic SIMS is best used to detect low concentration elements, such as C in SiGeC.

Table. 3.3. Comparison of chemical characterization techniques

Parameter	**RBS**	**AES**	**Dynamic SIMS**
What does it measure	Energy of backscattered He ions	Energy of Auger electrons	Secondary ions
Detection range	0.001-10 at% or 1E18 at/cc	0.1-1at % or 1E19 at/cc	0.0001-1at% 1E12-1E16 at/cc
Depth resolution	5 – 20 nm	2 – 20 nm	1- 20 nm
Lateral resolution (probe size)	≥ 1 mm	0.01 – 2 μm	≥10 μm
Calibration	NO	Yes	Yes

3.4. Epitaxial quality characterizations techniques

3.4.1. Atomic Force Microscopy (AFM)

The surface morphology of the heteroepitaxy is investigated by the Atomic Force Microscope (AFM) to identify the strain relaxation mechanism. A cross-hatch structure, which is usually associated with strain relaxation by misfit dislocations, 3-D islanding or pits due to Ge desorption can be observed.

3.4.2. Threading dislocation density (TDD) quantification

Etching is a powerful method in assessment of TDD because of its simplicity and high reliability [108]. Threading dislocation appearance is enhanced because the etchant diffuses faster into the TD 'pits', producing better contrast between the pit and the surface. Wright etch and Secco etch [46,47] were used in this project. The details of the composition and etching rate of these etchants can be found in Table 3.4. Both Wright and Secco etchants have an increased etching rate in SiGe samples [109,110]. After the samples were etched, TD observations and quantifications were performed with a Nomarsky microscope or a Scanning Electron Microscope (SEM).

Table 3.4. Chemical composition and etching rate of Wright and Secco etchants.

Parameter	**Wright Etch**	**Secco etch**
Recipe (all are part/vol)	$2HF + 2CH_3COOH + 1HNO_3 + 1CrO_3$ (4M) + 400 g/l solution + $2Cu(NO_3)_2.3H_2O$ (0.14M) + 33g/l of solution	2 HF + 1 $K_2Cr_2O_7$ (0.15M) + 4.4 g/l of solution
Etching rate in Si [108]	1.7 µm/ min	1.5 µm/min
Etching rate in SiGe [109]	2.5 µm/min	3 µm/min (for $0.15 < x < 0.4$)
Preferable planes	None (all uniformly-etched)	none

3.4.3. Transmission Electron Microscopy (TEM)

a. General principle of TEM

Transmission Electron Microscopy (TEM) is a method of forming an 'image' from the diffraction pattern of a sample illuminated by a high-energy electron beam. The resolution of TEM is < 2 Å, thus it is currently the only method capable of atomic-scale imaging. TEM images are formed in two stages as shown schematically in Fig. 3.11 [111]. *Stage A* consists of scattering of an incident electron beam by a specimen, followed by the formation of diffraction pattern at the back-focal plane by the objective lens. *Stage B* consists of the formation of the primary image by Fourier transform of the diffraction pattern and the magnification of the primary image by a series of projection lenses.

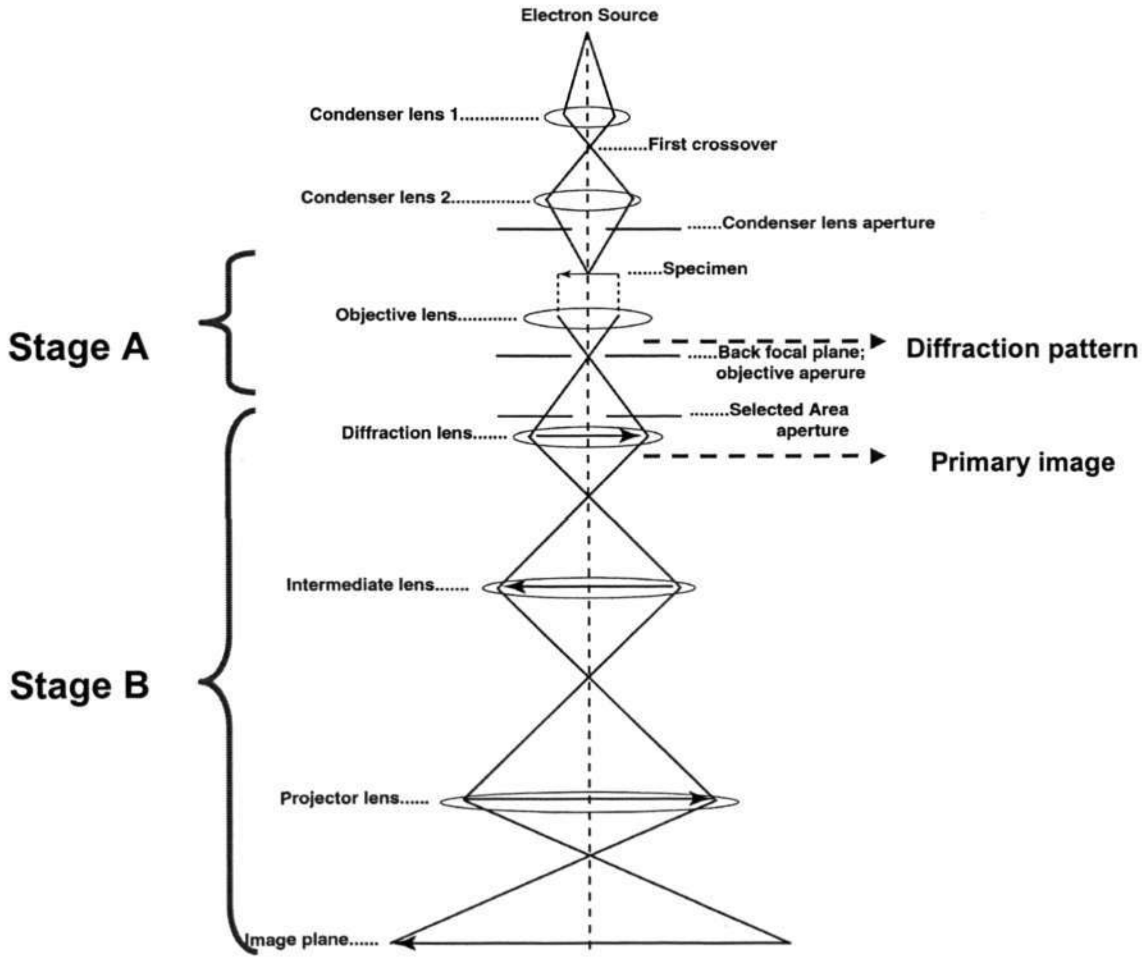

Figure 3.11. Schematic of TEM and the two stages of image formation.

Two types of TEM image can be formed by changing the strength of the intermediate lens. If the intermediate lens is focused to the back focal plane, the diffraction pattern is projected to the final image plane. If the intermediate lens is focused to the primary image at the diffraction lens, the real image is projected as the final image. The crystal plane can be diffracted and projected as an image if the plane is tilted to satisfy Bragg's law and intersects the Ewald sphere. In a diffraction experiment, it is important to recognize the diffraction pattern of the desired plane and tilt the specimen to this plane.

b. Crystallography of silicon

TEM investigations of SiGe/Si heteroepitaxy usually include plan-view and cross-section images. Both Si and SiGe have diamond structure (Fig. 3.12) and belong to space group Fd-3m. The diagrams in Fig 3.12 show the diffraction patterns of the (001) and (110) planes of Si, which are the planes perpendicular to the electron beam in plan-view and cross-section observations, respectively.

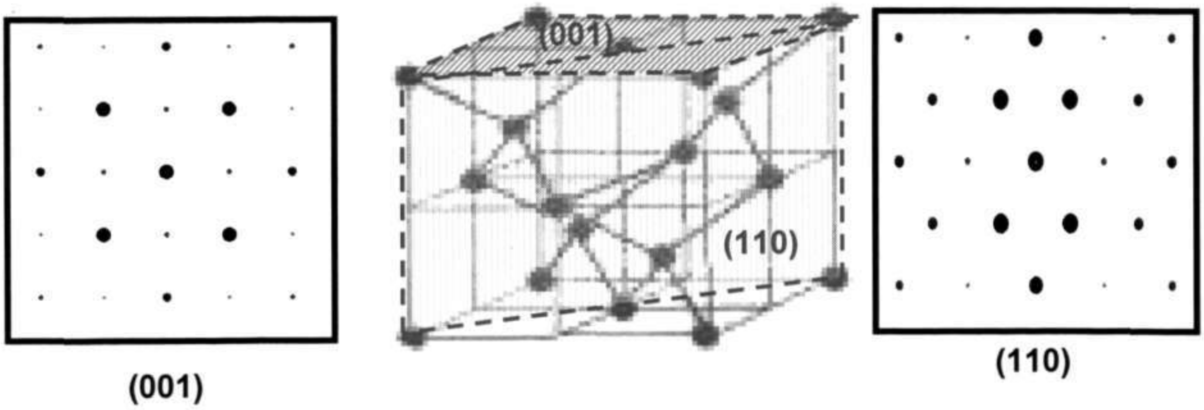

Figure 3.12. Crystal structure of Si unit cell and the diffraction patterns from (001) and (110) planes.

c. Imaging mode and contrast formation

There are two types of contrast present in TEM images: amplitude contrast and phase contrast, but one will tend to dominate.

1. Amplitude contrast:

- In a mass thickness contrast: areas with higher mass/thickness will scatter electrons more strongly

- diffraction contrast: various crystal planes will diffract the electrons differently, resulting in contrast.

2. Phase contrast: Many beams form the image due to phase changes between the forward scattered and diffracted beams. Small changes in the thickness, orientation, or scattering factor of the specimen, and variations in the focus or astigmatism of the objective lens will alter the appearance of the image.

Image contrast is obtained either by selecting specific electrons or excluding them from the imaging system. This selection is possible by inserting the objective aperture into the back focal plane of the objective lens. The schematic in Fig. 3.13 shows the diffraction patterns with objective aperture inserted on different diffraction spots and the resultant imaging mode.

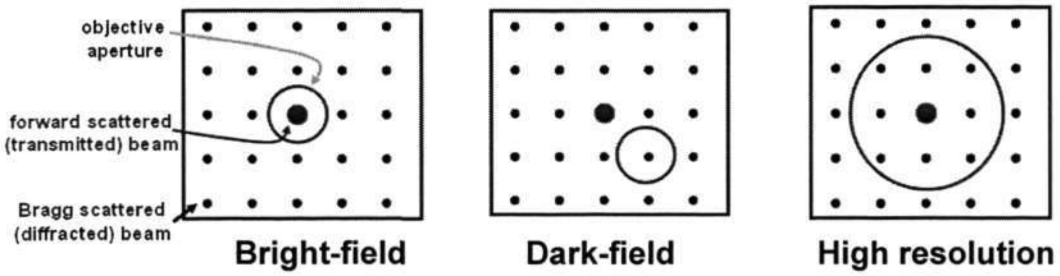

Figure 3.13. Objective aperture positions on a diffraction pattern for Bright-field, Dark-field and High-resolution imaging modes.

A bright-field image is formed by placing the objective aperture at the transmitted beam. The mass-thickness contrast is dominant in a bright-field image where the regions with higher mass/thickness will appear darker. A dark-field image is formed by placing the objective aperture on one of the diffracted beams. The diffraction contrast is dominant because the only plane contributing to the final image is the one selected by the aperture. A high-resolution image is formed by placing the objective aperture around the nearest diffracted beams to the forward beam. Since many crystal planes are included, the contrast mechanism is more complicated and phase contrast is dominant.

d. TEM instrumentation

TEM investigations in this work were performed at 200 kV on a JEOL JEM-2100F field emission electron microscope equipped with double-tilt holder, CCD and TV-rate camera, and LINK ISIS EDS X-ray micro-analyzer. Field-limiting apertures used for Selected Area Electron Diffraction (SAED) were 5, 20, and 60 μm in diameter. HRTEM images were collected using a high contrast objective aperture of 20 μm in diameter corresponding to a nominal point-to-point resolution of 1.7 Å. Electron diffraction patterns were calibrated repeatedly using external standards. Lattice parameters were determined repeatedly to check the hysteresis of electromagnetic lenses, obtaining values accurate to less than ± 0.1 % relative.

e. Sample preparation

The cross-section TEM samples were prepared by grinding a stack of epoxy-glued Si wafers to a thickness of ± 100 μm. The thinned sample was then stuck on a Cu grid before dimpling to a thickness of ± 20 μm. Afterwards, the sample was ion-milled from both sides to electron-transparent thickness regimes (20-100 nm). The plan-view TEM samples were prepared by cutting the Si wafer to a 3-mm discs and grinding from the back of the wafer. Dimpling and ion milling were carried out from the substrate side to protect the SiGe film.

Chapter 4:

Determination of Raman strain shift coefficients of strained Si and strained SiGe

Raman spectroscopy has been a preferred method to extract strain because of its ability to measure small area devices [112,113] and its surface sensitivity has been widely utilized to quantify strain in strained Si and strained SiGe on insulators [114-116]. In this chapter, the strain-shift coefficient of strained Si and strained SiGe, needed to quantify strain, are determined by a combination of HR-XRD and Raman spectroscopy measurements.

In a biaxial strained SiGe, strain in the growth plane (001) is given as: $\varepsilon_{//}^{StSiGe} = a_{st\text{-}SiGe} - a_{Si}/a_{Si}$. It is related to the Raman frequency shift ($\Delta\omega_{Si-Si}^{StSiGe}$) by the strain shift coefficient of Si-Si vibration in strained SiGe, b_{Si-Si}^{StSiGe}, according to the following relation [38]:

$$\Delta\omega_{Si-Si}^{St-SiGe} = (\omega_{Si-Si}^{St-SiGe} - \omega_{o\,Si-Si}^{bulkSi}) = -k.x + b_{Si-Si}^{StSiGe}.\varepsilon_{//}^{StSiGe} \qquad (4.1)$$

where k is an empirical constant and x is the Ge content. The term $k.x$ is used to take into account the phonon shift due to the Ge mass effect, while the $b\varepsilon$ term accounts for the frequency shift due to strain alone. Both ω_{Si-Si}^{StSiGe} and $\omega_{o\,Si-Si}^{bulkSi}$ can be obtained from the Raman spectrum of a typical strained $Si_{1-x}Ge_x$ on Si (Fig. 4.1), where in this particular spectrum, x=0.32.

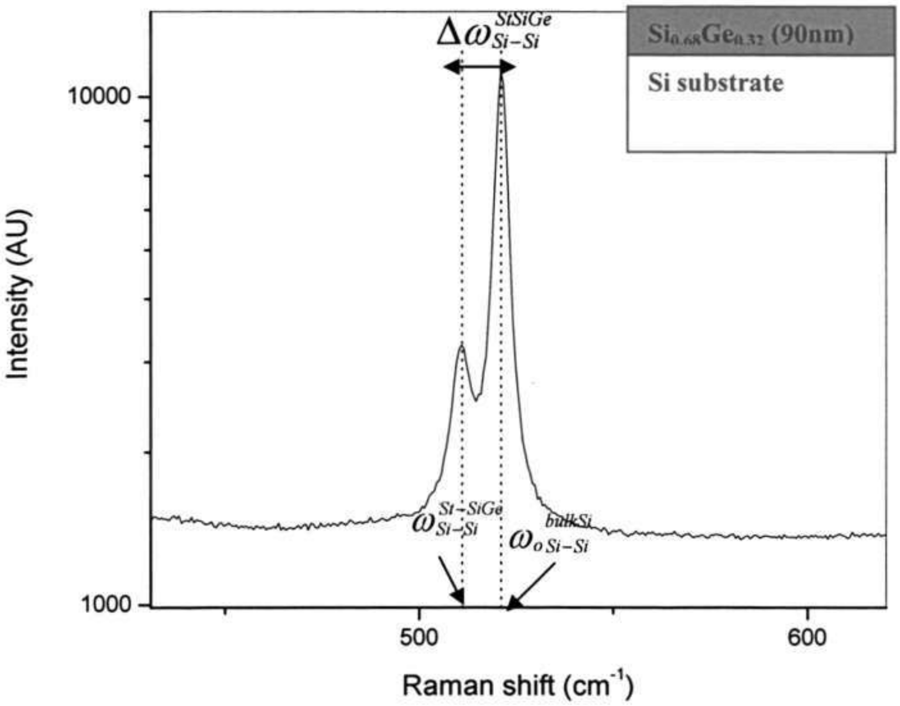

Figure 4.1. Enlarged version of Raman spectra of strained SiGe on Si substrate and the inset showing the schematic of strained SiGe samples.

The amount of strain in strained Si ($\varepsilon_{//}^{StSi}$) is related to the Raman frequency shift ($\Delta\omega_{Si-Si}^{StSi}$) by the strain shift coefficient of strained Si, b_{Si-Si}^{StSi}, according to the following relation [117]:

$$\Delta\omega_{Si-Si}^{StSi} = \omega_{Si-Si}^{StSi} - \omega_{o\,Si-Si}^{bulkSi} = b_{Si-Si}^{StSi}.\varepsilon_{//}^{StSi} \qquad (4.2)$$

where $\Delta\omega_{Si-Si}^{StSi}$ is the difference between the phonon frequency of strained Si (ω_{Si-Si}^{StSi}) and bulk Si ($\omega_{o\,Si-Si}^{bulkSi}$) (Fig. 4.2.). The spectrum in Figure 4.2 belongs to a 25 nm strained Si grown on relaxed $Si_{1-x}Ge_x$, where x=0.25.

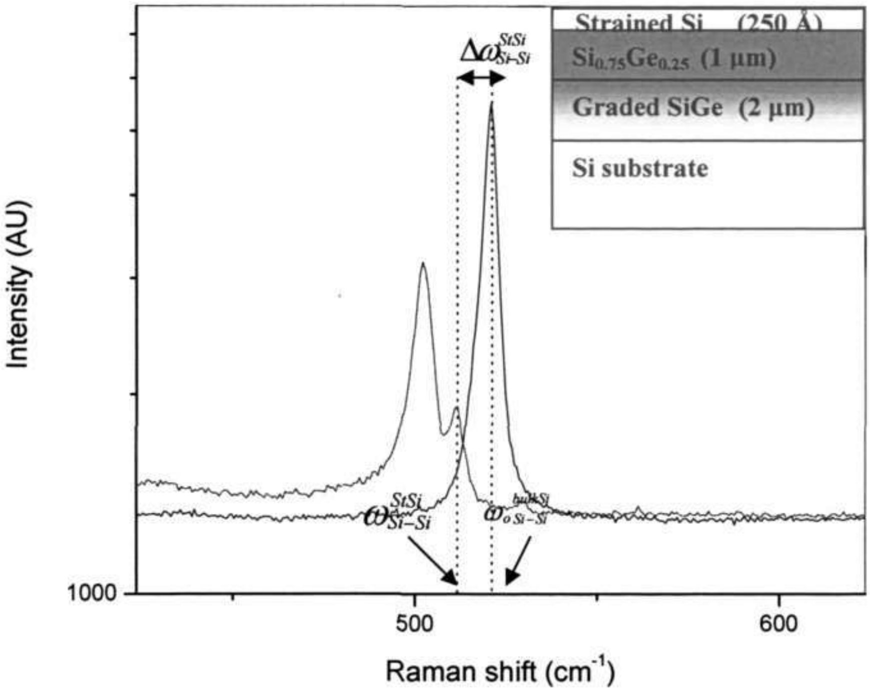

Figure 4.2. Enlarged version of Raman spectra of strained Si on relaxed SiGe and the inset showing the schematic of strained Si samples.

Even though b_{Si-Si}^{StSi} is crucial for accurate strain determination, it has not been reported before. Values quoted in the literature are derived from theoretical calculations [39], or estimated from b_{Si-Si}^{StSiGe} [38-45] , and the strain in strained-Si has been calculated based on these values [112-113]. In this chapter, for the first time, the direct measurement of the *b* coefficient of Si-Si mode in strained Si (b_{Si-Si}^{StSi}) is presented based on the correlation of HR-XRD and Raman spectra.

Three types of commercial wafers (inset of Fig 4.2) were used, each with 15%, 20% and 25% of Ge in the SiGe buffer layer, which correspond to different strain level in the strained Si. Symmetric (004) and asymmetric (115) rocking curves were obtained from a Bede Triple Axis HR-XRD to determine the Ge concentration and the relaxation in the SiGe layer. The Ge concentration agreed well with the Auger Electron Spectroscopy result and the relaxation values of SiGe in all samples are between 98-100%. The Raman spectra were taken from a triple-grating micro Raman system in a backscattering geometry using a 514.5 nm line from an-argon ion laser. It should be noted that the biaxial strain that splits the triply degenerate optical phonon mode at the Brillouin center is not a singlet with vibrational eigenvectors parallel to the strain axis and a doublet with eigenvectors perpendicular to that axis. In a backscattering geometry with [001] growth direction, only the singlet is observed, and thus all our Raman peaks correspond to the vibration along the (001) plane.

Based on equation 4.1, b_{Si-Si}^{StSi} is the slope of a plot of $\Delta\omega$ vs $\varepsilon_{//}$ for a series of samples with different strain conditions. Such plot is shown in Figure 4.3. Strain in Si ($\varepsilon_{//}$) is determined from the distance between the diffraction peak of Si substrate and strained Si in the HR-XRD rocking curve. $\Delta\omega_{Si-Si}^{StSi}$ was obtained from the difference between ω_{Si-Si}^{StSi} and the $\omega_{o\,Si-Si}^{bulkSi}$, which were obtained by performing Lorentzian curve fitting of the Raman spectra. The b_{Si-Si}^{StSi} coefficient was found to be -784 ± 4 cm^{-1}. This value falls within the range of the theoretical calculations of -723 and -832 cm-^{1} [39,40]. We should note that theoretical predictions are based on phonon deformation potential (p and q) obtained for uniaxial strained Si, and do not accurately represent the biaxial strain condition of our samples. In addition, even though some of the reported b_{Si-Si}^{StSiGe} are rather close to our measured value, it is principally incorrect to use b_{Si-Si}^{StSiGe} [38-45] to calculate strain in strained Si because b_{Si-Si}^{StSiGe} depends on Ge concentration, x. Thus, our measured strain shift coefficient for strained Si is a more representative value than the theoretical predictions and the generally used b_{Si-Si}^{StSiGe}.

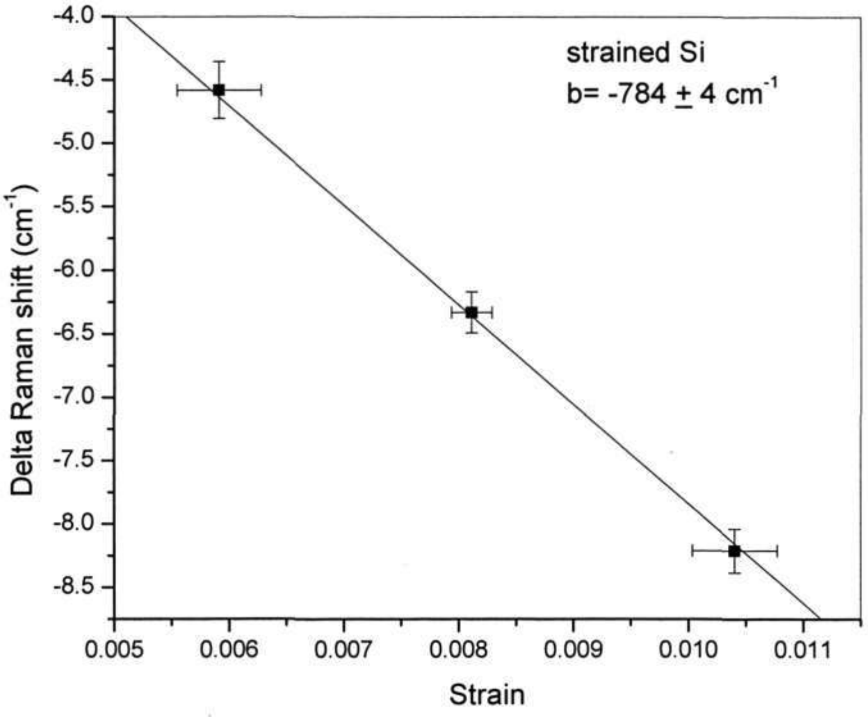

Figure 4.3. Delta Raman shift (between Si-Si vibration of strained Si and bulk Si) as a function of strain obtained from XRD. b is the slope of the linear fit.

Even though many have reported the measurement of b_{Si-Si}^{StSiGe}, there remains an unresolved issue of whether or not b_{Si-Si}^{StSiGe} is dependent on Ge concentration. The majority of the reported b_{Si-Si}^{StSiGe} were obtained with the assumption that b is independent of Ge concentration. The only comprehensive report on the b dependence on Ge concentration is that of Lockwood and Baribeau [117].

The theoretical definition of *b* suggests that it should depend on Ge concentration. For a biaxial strain, the b coefficient is given by [40]:

$$b = \frac{1}{2\omega_o}\left(-\frac{2C_{12}}{C_{11}}p + 2q\right) \qquad (4.3)$$

where ω_o represents the position of Si-Si peak in a fully relaxed SiGe ($\omega_{o\,Si-Si}^{bulkSiGe}$), p and q are phonon deformation potentials, C_{11} and C_{12} are the elastic stiffness constants of the epilayer. Since C_{11}, C_{12} and ω_o vary with Ge concentration [38,118], so should b_{Si-Si}^{StSiGe}. In other words, producing a similar amount of ε by 2 different methods (i.e. adding more Ge vs moderating Si-Si stretch by thermal annealing) would result in different $\Delta\omega_{Si-Si}^{StSiGe}$. Since the earlier reports used Ge to induce strain, the concentration and strain effects are coupled. The concentration dependence of b_{Si-Si}^{StSiGe} could thus be masked, possibly contributing to the large scatter in b_{Si-Si}^{StSiGe} values in the literature: from -455 to -1040 cm^{-1} [38-45]. This work aims to verify the *b* dependency on Ge concentration and to establish a relationship to quantify this dependency.

Table 4.1. Strain shift coefficient b of Si-Si vibrations from various sources.

Reference	**b (cm^{-1})**	**λ(nm)**	**Methods**
Present work	-784 ± 4	514.5	Si-Si in strained Si
Anasstasakis [39]	-832	1064	Theoretical calculation
Lockwood [117]	-715 ± 50	458	Extrapolation
Cerdeira [40]	-455		Si-Si in SiGe, independent of Ge
Tsang et al. [38]	-815 ± 48	Ar laser	
Dietrich [43]	-940	514.5	
Lu [44]	-931	514.5	
Halliwel [45]	-930 ± 90	457.5	
Holtz [42]	-1040 ± 23	351	

For the determination of b_{Si-Si}^{StSiGe}, three types of strained SiGe, with different Ge concentrations (15%,21% and 32%), were grown on Si substrates by Low Pressure CVD at 700°C using SiH_4 and GeH_4 as reactants. The thicknesses of all SiGe samples were kept slightly above their critical thicknesses in order to allow strain relaxation during thermal annealing. The structures of these samples are shown in the inset of

Fig 4.1. The Ge concentration was determined by HR-XRD and Rutherford Backscattering Spectrometry (RBS). All samples were annealed at temperatures between 800 – 1000 °C for 1 minute to induce strain relaxation, thus producing several strain values for each value of Ge concentration. Annealing was carried out in a Rapid Thermal Processing (RTP) machine such that strain relaxation via Ge diffusion was prevented and the Ge concentration remained constant after annealing, as confirmed by HR-XRD. Our AFM data (not shown) also shows a crosshatch structure, which indicates that strain relaxation is achieved by the formation of misfit dislocations. The Raman spectrum of each sample was then measured by using the Raman setting mentioned previously and the strain values were obtained from HR-XRD. The plots of $\Delta\omega$ vs $\epsilon_{//}$ for each sample are presented in Fig. 4.4, and the slope of each plot is the b_{Si-Si}^{StSiGe} of the particular $Si_{1-x}Ge_x$ sample. Together with b_{Si-Si}^{StSi} (i.e. x=0), we have clearly shown that b_{Si-Si}^{StSiGe} has a dependence on Ge, because if b_{Si-Si}^{StSiGe} is independent of Ge, these 4 plots will have similar slope.

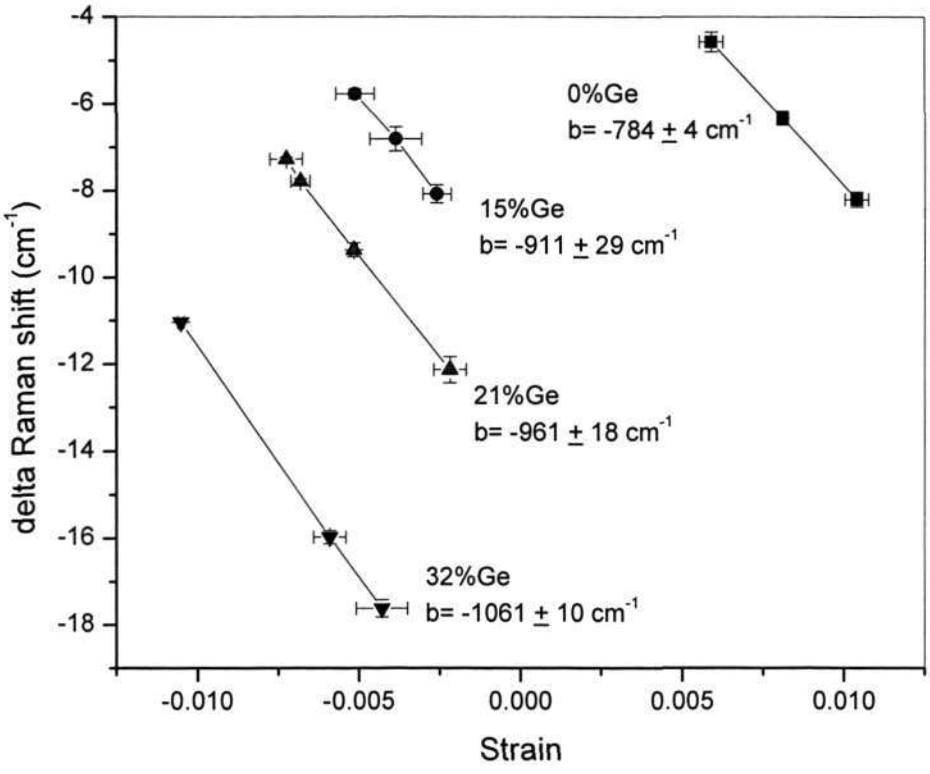

Figure 4.4. Delta Raman shift (between Si-Si vibration of strained SiGe and bulk Si) as a function of strain obtained from XRD for $Si_{1-x}Ge_x$, with x=0.15, 0.21, and 0.32 as well as the plot for strained Si samples.

To further illustrate the Ge dependence, we plot our measured b_{Si-Si}^{StSiGe} values as a function of Ge concentration in Figure 4.5. The best linear fit of our measured b_{Si-Si}^{StSiGe} values yields the empirical relation b=-773.8 – 897.7x, in close agreement with the result of Lockwood and Baribeau [117]. We believe that our fit is a better representation because we have used a wider span of data was used than Lockwood and Baribeau [117], especially including the experimental b value of strained Si at x=0. It is noted that the extrapolated value at x=0 is -773.8 cm^{-1}, is very close to our *measured* b_{Si-Si}^{StSi} of -784 cm^{-1}, thus confirming the accuracy of the empirical relation.

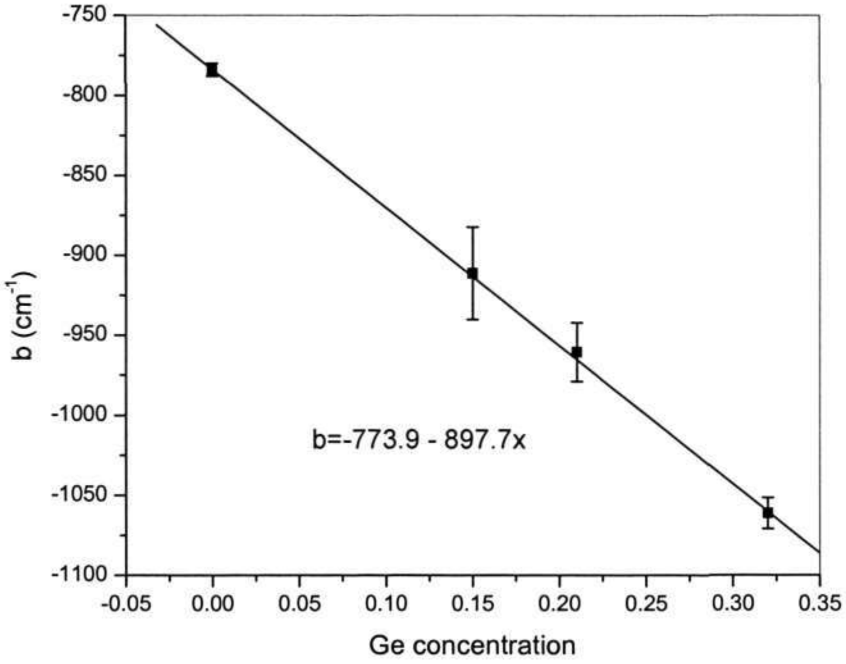

Figure 4.5. An empirical relationship of b values as a function of Ge concentration.

In summary, the first direct measurement of the Raman strain shift coefficient of Si-Si in strained Si, obtaining a measured value of -784 ± 4 cm^{-1}, has been presented. It has also been verified experimentally that b_{Si-Si}^{StSiGe} is a function of Ge concentration (x), consistent with its theoretical definition, and follows the empirical relation b= -773.8 – 897.7x for x<0.35.

Chapter 5:

Strain relaxation in a single epitaxial layer

Strain relaxation in heteroepitaxy begins when the thickness of the epilayer exceeds the equilibrium critical thickness [6]. The concept of critical thickness in a strained Si/relaxed SiGe/Si heterostructure is used in two different layers. The thickness of strained Si must be below the critical thickness to avoid strain relaxation. On the other hand, the thickness of relaxed SiGe must be beyond the critical thickness to promote strain relaxation, ideally maintaining a smooth surface and a defect-free interior. Stability beyond the critical thickness has been reported, usually by varying the epilayer thickness, because of the kinetic barrier to dislocation nucleation [17,25,51,53,78]. In this chapter, the stability of strained epilayers at thicknesses near the critical thickness is investigated during high temperature anneals, usually employed in the microelectronic manufacturing environment, to explore the limit of the strain relaxation. Two kinds of sample structures, i.e. strained Si on relaxed SiGe and metastable SiGe on Si substrate, were used and the strain relaxation mechanism was identified by different characterization methods. Discussions on each structure are presented in sections 5.1 and 5.2.

5.1. Thermal stability of strained Si on relaxed SiGe

One concern with strained Si is its thermal stability at high temperatures, where strain relaxation and Ge diffusion into the strained Si layer may become possible. If the strained Si relaxes, carrier mobility enhancement will not be obtained. Moreover, the presence of Ge in the channel region might create scattering centers that could degrade the carrier transport. Another consequence of Ge diffusion is the reduction of strained Si thickness.. A few studies on the thermal stability of strained Si have been reported [61,119,120]. Samavedam et al. [119] reported the elastic strain relaxation of strained Si; however the SiGe layer of their samples were not fully relaxed. The defects generated during the relaxation of these layers had a significant impact on the relaxation behavior of the strained Si layer. Sugii [61] focused on the Ge diffusion in strained Si, but did not discuss strain relaxation in details. Koester et al. [120] reported a comprehensive Raman study of both strain relaxation and Ge diffusion at high temperature, but did not show conclusive evidence of the Ge diffusion.

In this sub-chapter, High Resolution X-Ray Diffraction (HR-XRD), Raman spectroscopy and Secondary Ion Mass Spectroscopy (SIMS) are used to study the effect of thermal annealing on the strain relaxation and Ge diffusion of strained Si/$Si_{1-x}Ge_x$ ($x = 0.15$ to 0.25) substrates. The wafers used in this work were obtained from commercial sources and the basic layer structure is shown in Fig. 5.1. A 2 μm-thick, linearly graded SiGe layer was grown on p-type Si wafers. On top of the graded SiGe, 1 μm layer of uniform SiGe and 200Å of strained Si layer were grown. The Ge concentrations in the uniform SiGe layer of our samples are 15%, 20% and 25%. The samples were annealed in both furnace and RTA to study the effect of ramp up time on the strain relaxation and Ge diffusion. Furnace annealing was conducted at 800°C for up to 5 hours, and RTA annealing was conducted at 1000°C for up to 5 minutes.

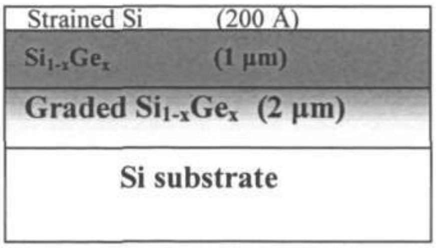

Figure 5.1. Schematic of the strained Si sample used in this experiment

The Ge content was also determined independently by Auger Electron Spectroscopy (AES). High Resolution XRD rocking curves were used to obtain the relaxation condition of the SiGe layer and the amount of Ge. The results are summarized in Table 5.1. The data indicate that the bulk SiGe layer underneath strained Si is fully relaxed, and the Ge concentration agrees well with the vendors' specifications.

Table 5.1. Specifications of the samples used in this experiment.

Sample	Ge content		Relaxation (%)
	AES	HR-XRD	HR-XRD
A15	15%	0.14-0.15	99-100
A20	20%	0.19-0.2	99.5-100
A25	25%	0.24-0.25	98-100

Figures 5.2. (a), (b), and (c), show the Raman spectra of furnace-annealed samples with 25%, 20% and 15% Ge in SiGe, respectively. No significant shift can be observed from the Si-

Si peaks in all spectra, indicating that the strain in the strained Si layer is stable throughout the annealing cycle.

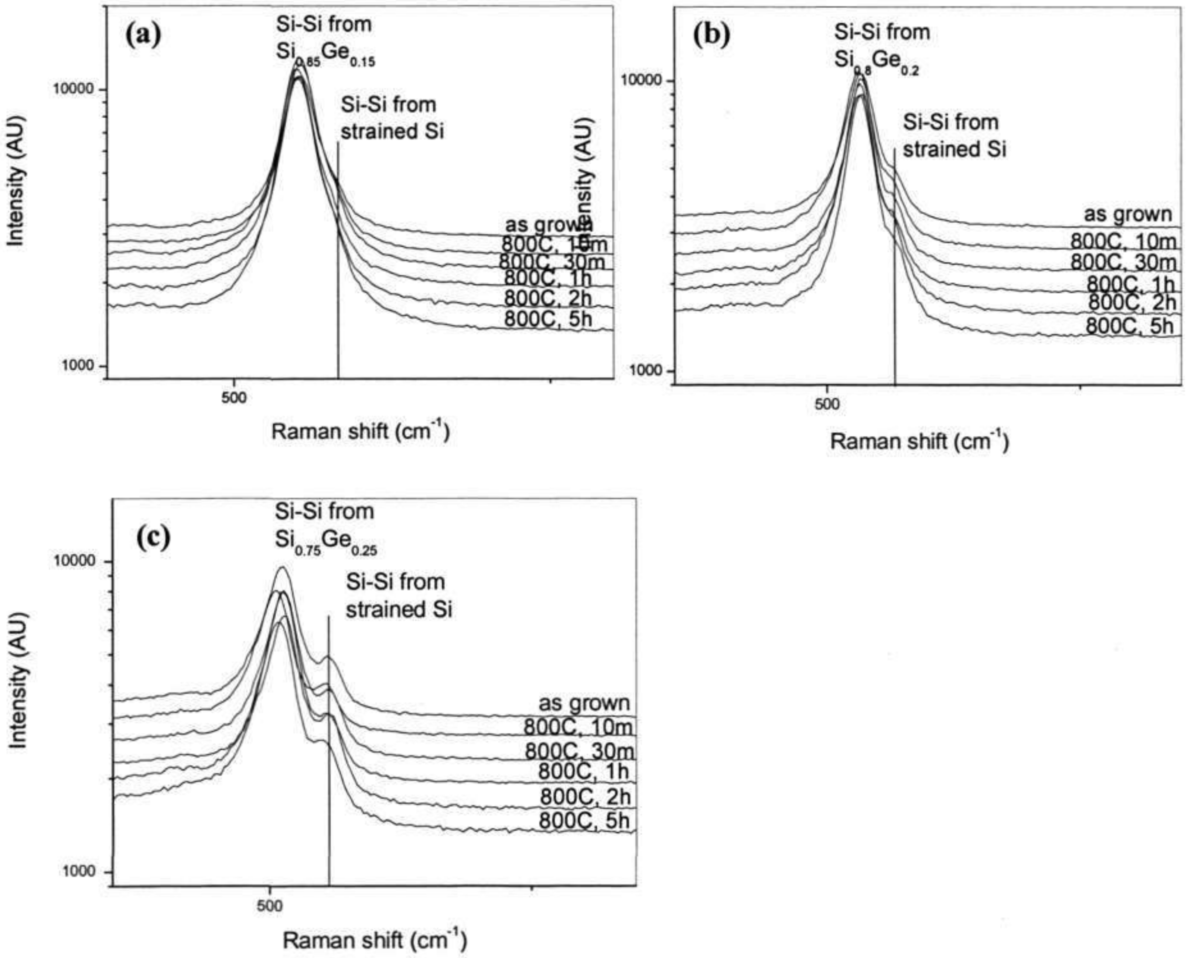

Figure 5.2. Raman spectra of sample (a) A15, (b) A20 and (c) S25 annealed at 800ºC for various time.

Figures 5.3. (a), (b), and (c) show the Raman spectra of samples A15, A20 and S25 annealed at 1000°C at different times. Annealing up to 1 minute at 1000°C does not result in any significant shift of the Si-Si peak in strained Si, and hence implies no strain relaxation.

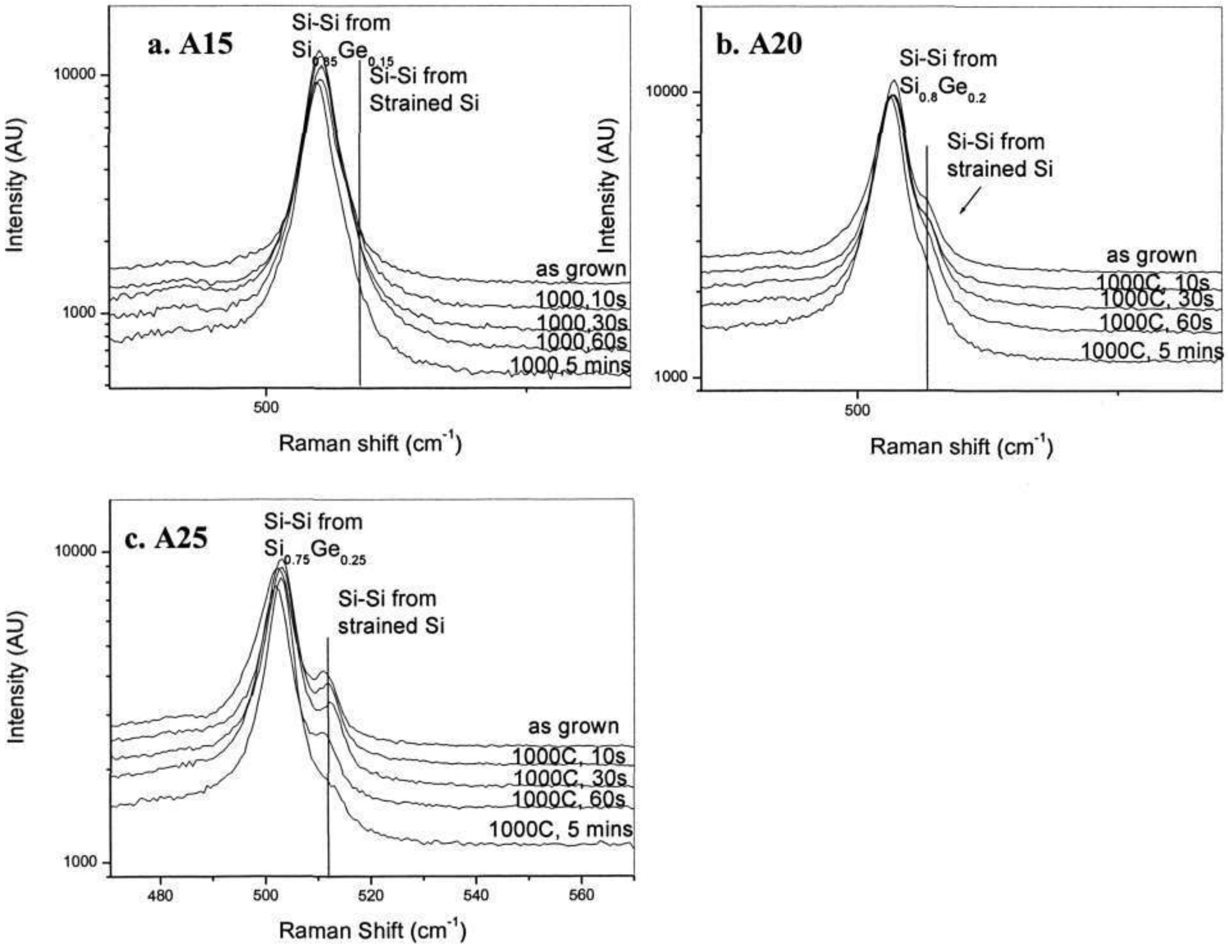

Figure 5.3. Raman spectra of sample a. A15, b. A20 and c. S25 annealed at 1000ºC for various time.

Strains in the strained Si layer after various annealing conditions were quantified according to the strain shift coefficient determined earlier in Chapter 4, and the result is presented in Figure 5.4. The closed symbols correspond to samples annealed at 1000°C, while the open symbols correspond to samples annealed at 800°C. The relatively-constant strain trends confirm that after annealing, strain relaxation does not take place within the sensitivity of the characterization technique.

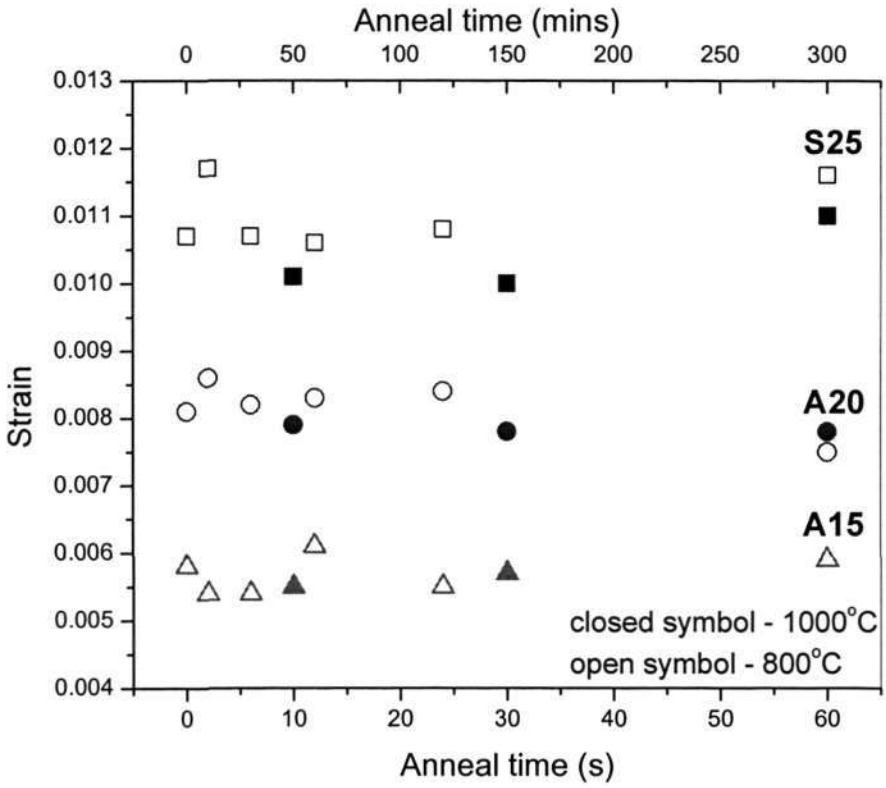

Figure 5.4. Strain in strained Si after annealing at various conditions.

According to the critical thickness defined by Matthews and Blakeslee [6], only A15 has a strained Si thickness lower or equal to the critical thickness, and thus this strained Si sample layer is thermodynamically stable. On the other hand, the thickness of strained Si layer in both A20 and A25 are higher than their respective critical thicknesses

At the same time, dislocation decoration observations revealed no significant increase in dislocation density in these films. Together, these results indicate that strained silicon layers can retain misfit strain without generating misfit dislocations at thicknesses beyond that prescribed by the equilibrium theory of heteroepitaxial growth. Thermodynamically, these strained Si layers should be considered metastable. The absence of strain relaxation accompanied by misfit dislocation generation suggests that substantial kinetic barriers exist for dislocation nucleation in these films.

Even though there is no shift in the Si-Si vibration, samples annealed at 1 and 5 minutes show a significant intensity reduction (Figures 5.3. a,b,c). Since the relative intensities are roughly proportional to the relative numbers of corresponding bond types, the intensity reduction can be explained as the thinning of the strained Si layer. To prove that Raman intensity reduction is indeed due to Ge diffusion, we performed SIMS on all samples annealed at 1000°C (not shown). Figure 5.5. shows the SIMS spectrum of sample A25 before and after annealing at 1000°C for 5 mins. It is shown from SIMS that Ge diffuses up to 4-5 nm into the strained Si layer after annealing of 1000°C for 5 minutes. At this diffusion depth, Ge will not change the properties of gate oxide grown on strained Si. However, in real device fabrication, where multiple high temperature anneals may be performed, more Ge might diffuse into the strained Si region. This problem can be avoided by minimizing the high temperature anneal during fabrication. Nevertheless, in another strained Si based structure, such as strained Si on strained Ge for a dual-channel device [14,15], the strained Si thickness is on the order of 5 nm. If Ge diffusion cannot be avoided, Ge will not only degrade the gate oxide quality, it will also reduce the electron mobility enhancement in strained Si.

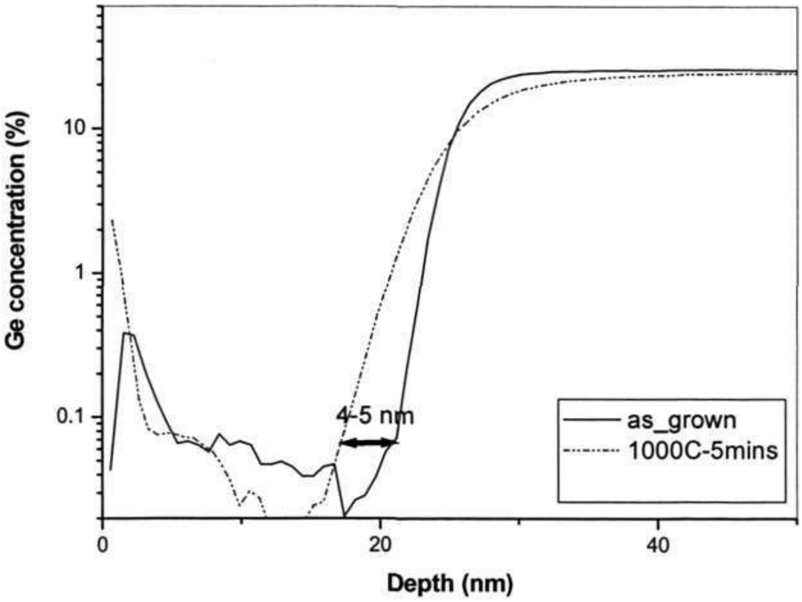

Figure 5.5. SIMS spectra of sample S25 before and after annealing at 1000°C for 5 mins.

To conclude, the thermal stability of strained Si/SiGe heterostructures has been studied under different annealing conditions. It is found that strain in strained Si is intact for annealing up to 1000 °C for 5 minutes, even though slight diffusion of Ge into strained Si is detected. Hence, the use of strained Si substrates at higher temperatures is likely to be limited by Ge diffusion rather than strain relaxation.

5.2. Strain relaxation of metastable SiGe on Si

In SiGe epitaxial heterostructures, there are a range of 'metastable' thicknesses in which the SiGe layer is strained as grown, but when sufficient thermal energy is applied, relaxation will take place by the formation of dislocations. Previous studies have focused on the onset of strain relaxation, that is, the nucleation of new misfit dislocations [121], but few focused on the relaxation of the metastable film after thermal processing. Matthews and Blakeslee [6] have predicted the onset of strain relaxation by the formation of misfit dislocations under equilibrium conditions. Even though their approach has been regarded as one of the finest, their critical thickness values are lower than most of the reported experimental values [17,25,51,53,78]. Fischer et al. [122] calculated the incomplete strain relief at the end of thermal relaxation process of a metastable SiGe/Si heterostructure by taking into account the surface relaxation effects and elastic interactions between straight misfit dislocations. Even though Fischer's theory has invited some criticism [123,124], many experimental critical thicknesses [125-127] agree well with his prediction. In this sub-chapter, SiGe epilayers with different Ge concentrations and thicknesses are used to study the onset and extent of relaxation as well as the corresponding relaxation mechanisms. Experimental results suggest that surface relaxation may be dominant during the initial relaxation of a metastable film for thicknesses larger than the equilibrium critical thickness. After annealing, the strain relaxation of the metastable SiGe samples was quantified and the dominant relaxation mechanisms were identified by different characterization techniques. Evidence of the saturation of relaxation via misfit dislocation generation was discovered, suggesting a work-hardening phenomenon.

A series of strained $Si_{1-x}Ge_x$ on Si samples, with $x = 0.04 - 0.21$, were grown by LP-CVD at 700°C, with SiH_4 and GeH_4 as precursors. The Ge concentration was determined by Rutherford Backscattering Spectrometry (RBS). The thickness (h) range is between 900-1300´ as determined by High Resolution XRD (HR-XRD) and RBS. Except for SiGe4, the thickness of the other samples is slightly higher than the equilibrium critical thickness [6], and thus is classified as metastable strained SiGe. Some of the samples were rapid-thermal-annealed at 900°C and 1000°C, which is the higher end of the thermal budget of a typical IC manufacturing process, at various durations. The strain conditions before and after annealing were quantified by HR-XRD. The surface morphology and roughness were observed by Atomic Force Microscopy (AFM), while the threading dislocation density (TDD) was determined by chemically etching the surface, and observation by Nomarsky optical microscopy and SEM. Auger Electron Spectroscopy (AES) was used to investigate the Ge profile before and after annealing.

The symmetric [004] rocking curves of the as-grown samples, with $x = 0.11$, 0.14 and 0.21, are shown in Figure 5.6. The lattice fringes of the SiGe peak indicate the high epitaxial quality of the SiGe layers. The in-plane lattice constant of the SiGe layer can be determined from the separation between the Si and the SiGe peaks. As the Ge content has been determined independently by RBS, the strain relaxation can be quantified. The strain relaxation degree is defined as,

$$R \equiv \frac{a_{//,SiGe} - a_{Si}}{a_{SiGe} - a_{Si}}, \tag{5.1}$$

where $a_{//,SiGe}$ is the in-plane lattice constant of SiGe layer, and a_{SiGe} and a_{Si} are the bulk lattice constant of SiGe and Si, respectively.

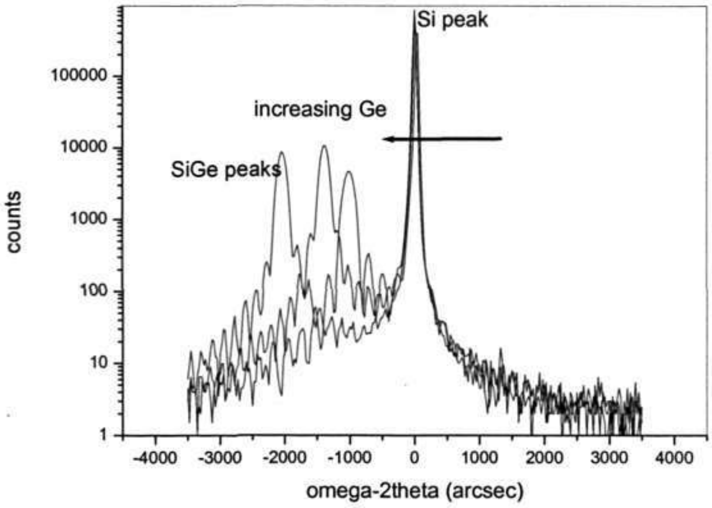

Figure 5.6. (004) rocking curves of SiGe11,SiGe14 and SiGe21.

The degree of strain relaxation of all as grown samples was quantified from their rocking curves and the results are summarized in Table 5.2 and plotted against *x.h*, which is equivalent to inherent misfit strain, in Fig. 5.7.

Table 5.2. Epitaxial quality of as-grown samples.

Sample	x	h (Å)	Relaxation (XRD)
SiGe4	0.038	924	0.12
SiGe6.5	0.065	937	0.29
SiGe10	0.1	1243	0.17
SiGe11	0.111	950	0.23
SiGe12	0.118	1177	0.22
SiGe13	0.134	1069	0.18
SiGe14	0.142	1338	0.15
SiGe16	0.161	986	0.24
SiGe21	0.211	1200	0.16

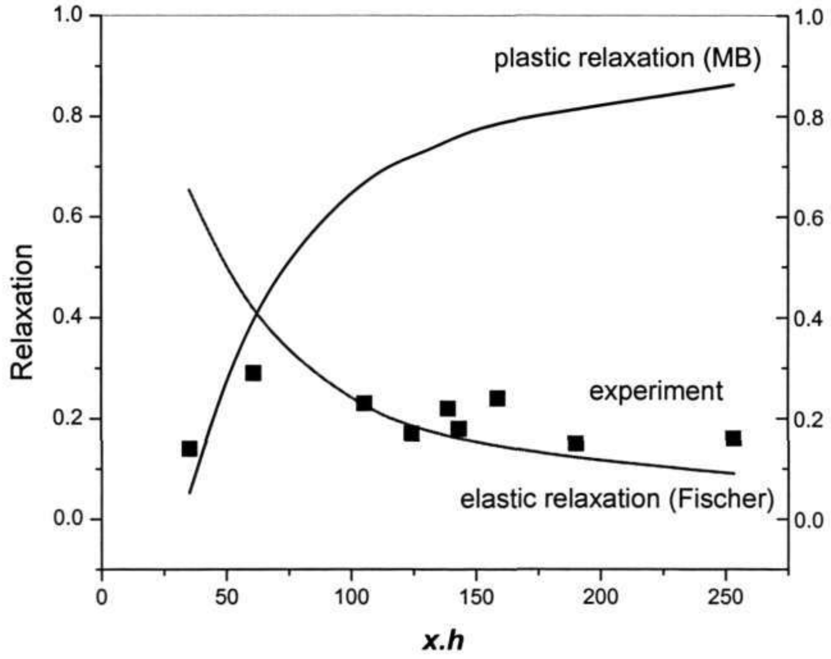

Figure 5.7. Comparison of the relaxation between experimental and theoretical predictions [6,122] plotted as a function of inherent strain (*x.h*).

The experimental data in Fig. 5.7 shows that as *x.h* increases, the relaxation degree increases to a maximum before decreasing and saturating. The trend can be explained by taking into account the relaxation due to misfit dislocations and elastic surface relaxation. The degree of relaxation due to misfit dislocations was calculated based on the excess stress expression adopted from the original MB framework [6]. The relaxation degree due to surface relaxation (γ_{el}) as proposed by Fischer et al. [122] is given by:

$$\gamma_{el} = \frac{b\cos\lambda}{0.0836xh} \qquad (5.2)$$

where b is the magnitude of the Burger's vector, λ is the angle between the Burger's vector and the propagation direction of the misfit dislocation, x is Ge concentration, and h is epilayer thickness. Figure 5.7 shows that when *x.h* satisfies the metastability criteria (in this case, $x.h > 50$), the degree of relaxation is closer to Fischer's prediction. However, Fischer's theory does not accurately predict the relaxation degree of the sample with $x.h < 50$, whose thickness is slightly smaller than the equilibrium critical thickness [6]. This observation implies that surface relaxation, if any, does not rise to infinity when $h < hc$ because SiGe is thermodynamically stable in its strained condition. The absence of *hc* in Fischer's surface relaxation formulation suggests the model is flawed and needs to be revised. For SiGe with $x.h > 150$, the measured relaxation values are higher than the elastic relaxation values, suggesting that the contribution of misfit dislocation formation to the entire relaxation is more significant at high misfit strain.

The strain conditions of selected samples, i.e. those with x=0.11, 0.14 and 0.21, after annealing at 900 and 1000°C were determined by HR-XRD and the results summarized in Fig 5.8.

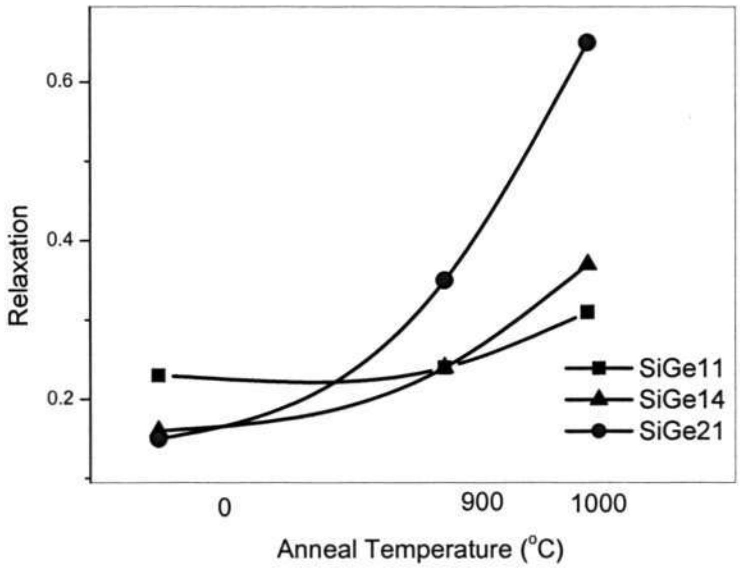

Figure 5.8. The relaxation of SiGe at different annealing temperatures.

After annealing, more relaxation is observed for samples with greater Ge contents because as the Ge content (and thus strain energy) increases, dislocation nucleation is more favored to reduce the overall energy in the heterostructure. Thus for the same amount of applied thermal energy, the extent of relaxation is different. To identify the different relaxation mechanisms, both threading dislocation density (TDD) and surface roughness of the annealed samples were determined and the results are summarized in Table 5.2. Figure 5.8 shows that the rate of relaxation of SiGe21 is higher than the other samples, however this relaxation is not accompanied by a significant increase in dislocation density or surface roughness (Table 5.3). It is possible, then, that another relaxation mechanism such as Ge interdiffusion, has taken place.

Table 5.3. Roughness and TDD of selected samples before and after annealing

	Sample	**as grown**	**900°C**	**1000°C**
Roughness (Å)	SiGe11	0.492	0.57	0.769
	SiGe14	0.5	0.595	1.08
	SiGe21	1.278	1.469	1.57
TDD (/cm^2)	SiGe11	<1.6E+04	1.12E+05	1.74E+05
	SiGe14	<1.6E+04	1.18E+05	2.24E+05
	SiGe21	5.00E+04	7.00E+04	4.76E+05

Auger Electron Spectroscopy was performed on SiGe21 before and after annealing and the result confirms the occurrence of Ge diffusion at the SiGe/Si interface (Fig. 5.9). It is deduced that in a metastable SiGe, full relaxation cannot be achieved by misfit dislocation only. This observation confirms an earlier prediction [122] and observations [128], which suggested that the saturation of strain relaxation is due to the dislocation blocking or pure elastic interaction between dislocations.

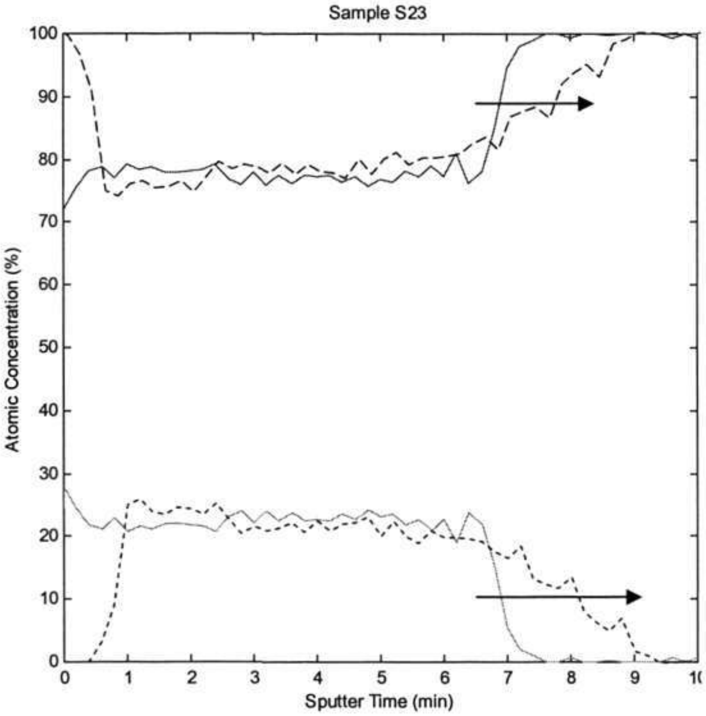

Figure 5.9. AES profile of SiGe21 before and after annealing at 1000°C for 1 minute.

In addition, it should be noted that the first Ge and Si signals of the annealed samples are obtained at a longer sputter time and there is a slight increase of Ge concentration at the surface (Fig. 5.9). This observation is attributed to unintentional oxidation during annealing resulting in a SiO_2 layer on the surface. It has been reported before that the oxidation of a SiGe layer may induce Ge segregation below SiO_2 [129,130].

Figure 5.10 shows the morphological change of SiGe21 before and after annealing at different conditions. After 1000 °C anneal, the cross-hatch structure, which can be related to misfit dislocations [131], are clearly observed. However, a higher magnification image reveals the presence of lighter-contrast clusters (inset of Fig. 5.10 (b)), which are suspected to be the Ge rich regions formed during oxidation [132].

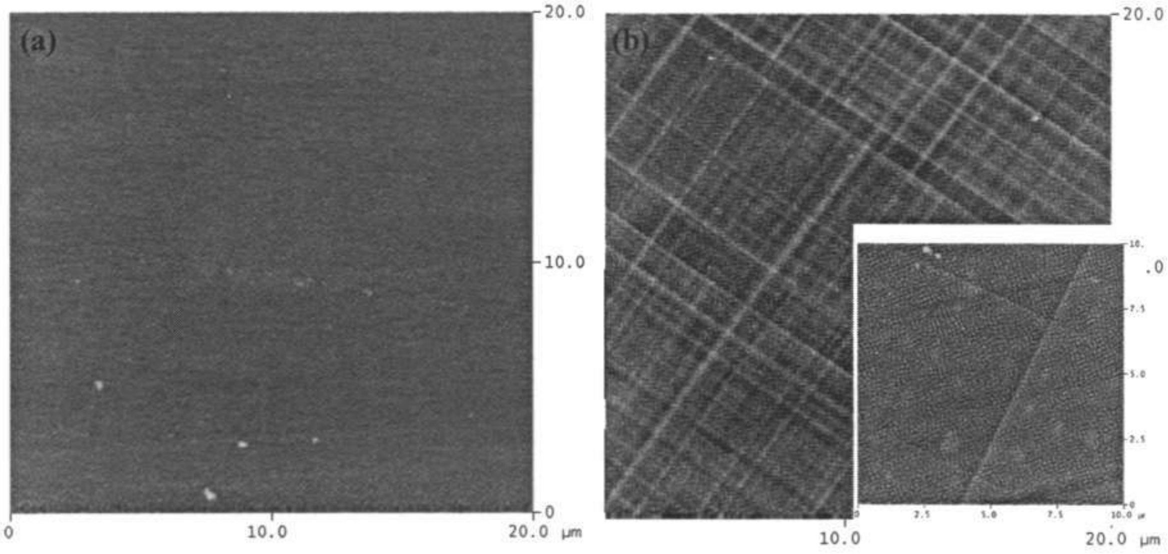

Figure 5.10. AFM images of SiGe21 (a) before and (b) after anneal.

The relaxation of metastable SiGe varies as a function of the inherent in-grown misfit strain in the system. The initial relaxation of as grown SiGe layer decreases with increasing Ge content, while the final amount of relaxation after post-annealing increases with Ge content. We attribute this to the role of surface relaxation, which could be dominant for samples with low Ge concentration and thickness. Different relaxation mechanisms were observed at different annealing conditions. Relaxation via misfit dislocation formation is observed at a lower annealing temperatures, and relaxation via Ge diffusion dominates at a higher annealing temperatures. Our results show that metastable strained SiGe cannot achieve full relaxation by the formation of misfit dislocations alone, possibly because of a work hardening phenomenon.

5.3. Chapter Summary

Strain relaxation mechanisms of strained Si and SiGe epitaxial layer after various annealing treatments have been investigated and the following conclusions can be drawn:

1. When the epilayer thickness is less than 2 times the MB thickness ($t < 2\ t_{MB}$), strain is stable up to 1000 °C for 5 minutes because of the kinetic barrier of dislocation nucleation.
2. When the epilayer thickness is larger than 10 times MB thickness ($t > 10\ t_{MB}$), experimental results suggest that surface relaxation is responsible for the initial relaxation, and after annealing at 900 °C, strain relaxation takes place by misfit dislocation generation and followed by Ge diffusion.

Chapter 6:

A novel concept of *reverse-graded* buffer layer for relaxed SiGe heteroepitaxy

Strained-channel transistors have attracted much attention recently in the Si industry because of strain-introduced mobility enhancement for both electrons and holes [4,5]. A traditional way of introducing strain into Si is to epitaxially grow Si on relaxed SiGe layers. Manufacturing such virtual substrates with good quality is however not trivial. A significant numbers of buffer layer methods have been proposed in order to grow relaxed SiGe with minimum threading dislocation density (TDD) and surface roughness, yet thermally stable at high temperatures. A review of these methods, as well as their advantages and disadvantages, has been presented in Chapter 2. So far, none of the reported buffer layer approaches meet the stringent requirements of the SiGe substrate for strained-channel transistors [29-35].

In this chapter, we present a novel concept of a reverse-graded SiGe buffer layer, in which a thin epitaxial buffer layer with a reversed Ge composition gradient, i.e. the Ge composition decreases from the substrate to the growing surface. This chapter is organized into four sub-chapters. In sub-chapter 6.1, the rationale of this method is explained theoretically by an equilibrium relaxation model. In sub-chapter 6.2, the growth and characterization of a reverse-graded SiGe heterostructure is demonstrated successfully for the first time. The strain relaxation and TDD reduction mechanisms of the RG heterostructure is discussed in sub-chapter 6.3, and finally, the thermal stability of this heterostructure are established in sub-chapter 6.4.

6.1. Equilibrium distribution of dislocations and residual strain in reverse-graded heteroepitaxy systems

Tersoff [48] proposed a quantitative picture of the role of grading, by calculating the equilibrium distribution of dislocations and residual strain in compositionally graded films. His model provides a design for the growth of high-quality FG heteroepitaxy layers and the proposed relaxation mechanism has been widely-accepted.

In a uniform composition epitaxial layer, the lattice misfit, f, between the film and the substrate is accommodated by misfit dislocations (MD) at the film/substrate interface. The residual in-plane strain, ε, is related to λ, the density of MDs per unit length by the following relationship: $\varepsilon = -(f - b_{//}\lambda)$, where b is the Burgers vector of the strain-relieving MD. The negative sign represents compressive strain. In a forward graded layer, the MDs are distributed along the film thickness with a MD cross-sectional density per unit area, $\rho(t)$, at a given distance t, from the film/substrate interface (t=0). The residual strain is generalized in the following form:

$$\varepsilon(t) = -[f(t) - b\int_{0}^{t}\rho(\tau)d\tau] \tag{6.1}$$

Where $\varepsilon(t)$ and $f(t)$ are the depth profiles of the residual plane strain and the lattice misfit, respectively. If the heterostructure is fully-strained, the dislocation-term is zero, and $\varepsilon(t) = f(t)$. If the heterostructure is fully-relaxed, $\varepsilon(t) = 0$, and differentiation of equation 6.1 yields the MD density (MDD) profile as given by:

$$\mu(t) = \frac{1}{b_{//}} d \frac{f(t)}{dt} \tag{6.2}$$

In a forward-graded layer, there exists a "critical thickness", t_o, below which $\varepsilon(t) = 0$, and the MDD profile is given by equation (6.2). Above t_o, the residual strain is the difference between the misfit strain and the amount of strain released up to t_o. The strain profile is given by:

$$\begin{aligned} &\varepsilon(t) = 0 && \text{for } 0 \leq t \leq t_o \\ &\varepsilon(t) = -\,[f(t) - f(t_o)] && \text{for } t_o \leq t \leq t_b \end{aligned} \tag{6.3}$$

where t_b is the total thickness of the FG layer. During growth, the thickness t_o changes dynamically following the generation of MD. However, in order to compute the final surface lattice parameter, it is sufficient to calculate t_o at the end of growth as given in equation (6.3). The residual strain increases the force on TD arms and facilitates the glide of MDs towards the wafer edge. As strain is mainly released by glide, less dislocation nucleation events would take place and the net TDD is reduced. Moreover, the possibility of TD annihilation would increase with enhanced TD movements.

Based on the above theory, one can predict the misfit dislocation distribution and residual strain for a given grading rate. The following schematics show the effect of grading on the dislocation and residual strain distribution.

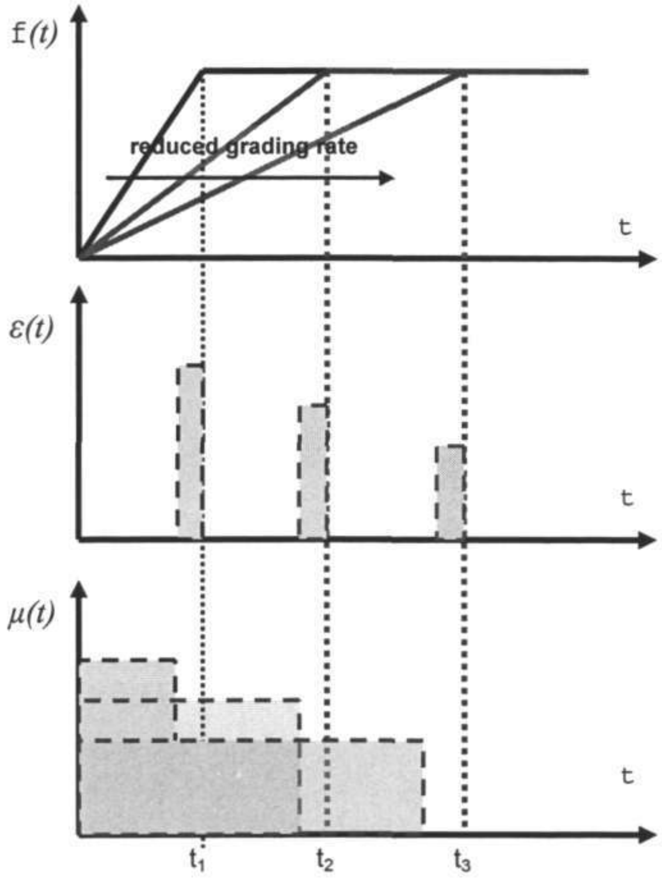

Figure 6.1. Schematic of the effect of grading rate on the residual strain and misfit dislocation distribution in a forward-graded buffer layer.

Figure 6.1 shows that a reduced grading rate results in a reduction of residual strain and a decrease of MDD. The main assumption in the above theory is that the system behaves in equilibrium condition, neglecting the kinetic barrier of dislocation nucleation and propagation, as well as dislocation interactions under stress. All of which has a strong dependence on growth conditions, such as wafer cleanliness, temperatures, growth rate and film thickness. As a consequence, even though it is theoretically possible to design a thin FG buffer by increasing grading rate (Fig. 6.1), previous experimental work suggests that a high-quality FG buffer layer requires a minimum thickness of 1 μm [86,133-139]. Attempts to reduce FG thickness by increasing grading rate resulted in extremely high TDD and roughness [138,139]. A summary of the reported epilayer quality vs grading rate is presented in Figure 6.2.

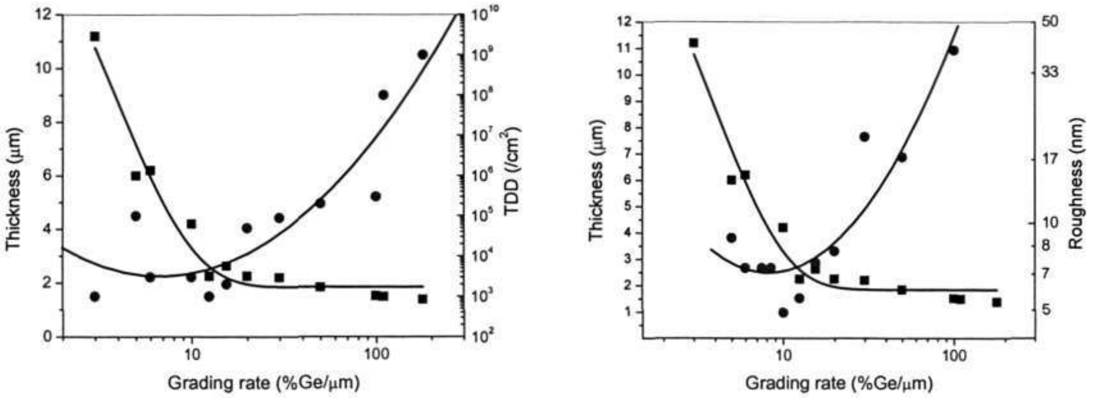

Figure 6.2. Summary of reported TDD and roughness values (red circles) [86,133-139] as a function of grading rate in forward graded SiGe heterostructures. The thickness of corresponding data point is also given in another axis.

The experimental observations were consolidated by an empirical model [78,140], which predicted the amount of residual strain at $t > t_o$. The model predicts that 90% strain relaxation can only be achieved if the thickness of the top uniform layer is 1μm and the minimum thickness of the FG buffer is 1 μm, giving a total minimum thickness of 2 μm. The FG buffer below this thickness does not have enough mismatch energy to initiate the nucleation of dislocations across the interfaces of the buffer layer. Most of the MDs will nucleate at the Si/buffer interface and the film stack behaves more closely to the uniform composition film. This fundamental limitation remains a challenge in the integration of FG buffer concept into real commercial devices because of the thermal dissipation issues discussed earlier [36-37].

In this section, Tersoff's equilibrium model has been extended to predict the distribution of dislocation and residual strain in a reverse-graded SiGe buffer layer. The qualitative approach shows that the dislocations can be localized at the Si/RG interface and a substantially-large residual strain is generated. The implication of this finding suggests that a thin buffer layer can be exploited to grow a high-quality relaxed SiGe layer.

A reverse-graded buffer layer starts with the highest lattice-mismatch layer at the Si interface and decreasing mismatch as the thickness increases. The lattice-mismatch profile of the RG layer as a function of thickness, t, is given by:

$$f(t) = f_o - d\frac{f(t)}{dt}.t \qquad (6.4)$$

where f_o is the lattice mismatch at the RG/Si interface. The residual strain profile can be represented by the following three cases:

$$\begin{array}{lll} \text{Case 1:} & \varepsilon(t) = f(t) & \text{for } 0 < t_{RG} < t_{MB} \\ \text{Case 2:} & \varepsilon(t) = -[f(t) - b\int_0^t \rho(\tau)d\tau] & \text{for } t_{MB} < t_{RG} < t_{M/S} \\ \text{Case 3:} & \varepsilon(t) \approx 0 & \text{for } t_{RG} >> t_{M/S} \end{array} \qquad (6.5)$$

where t_{MB} is the Matthews-Blakeslee critical thickness [6] for the total strain energy in the RG layer, and $t_{M/S}$ is the maximum metastable thickness, which depends on the growth conditions [68]. Equation (6.5) implies that the RG layer is fully strained when $0 < t_{RG} < t_{MB}$, partially relaxed when $t_{MB} < t_{RG} < t_{M/S}$, and fully relaxed when $t_{RG} >> t_{M/S}$. Since the objective of growing an RG layer is to introduce relaxation, case 1 is not desirable and the minimum RG thickness is $t_{RG} = t_{MB.}$ Full relaxation of RG (Case 3) is also not desirable because less residual strain would be generated. Moreover, a large thickness must be used to create the supersaturation of strain energy necessary for dislocation nucleation, similar to the FG case. In other words, a maximum grading rate and a minimum thickness would be required to achieve good quality heteroepitaxy. Thus, only a metastable RG is potentially beneficial and will be explained further.

The MD density profile of a metastable RG is given by:

$$\mu(t) = \frac{1}{b_{//}}(f_0 - d\frac{f(t)}{dt}) \qquad \text{for } t_{MB} < t_{RG} < t_{M/S} \qquad (6.6)$$

This equation implies that if $f_o > d\frac{f(t)}{dt}$, the highest MDD in the buffer layer is located at the Si/RG interface, i.e. $t = 0$, and reduces to a constant at $t > 0$. Based on the discussions above, the design rule of a RG layer can be determined by looking at the effect of grading rate on MDD distribution and residual strain. In a RG layer, the grading rate can be varied by:

a) keeping f_o constant and changing t, or

b) keeping t constant and changing f_o.

Both cases will be considered in the following illustrations.

a) f_o =constant, t increases

The effect of grading rate on the residual strain and MDD is illustrated in Fig.6.3 for $t_{MB} < t_{RG} < t_{M/S}$. For simplicity, the positive and negative signs for tensile and compressive strains are omitted, but its effects on the TD behavior will be further explored in the subsequent section.

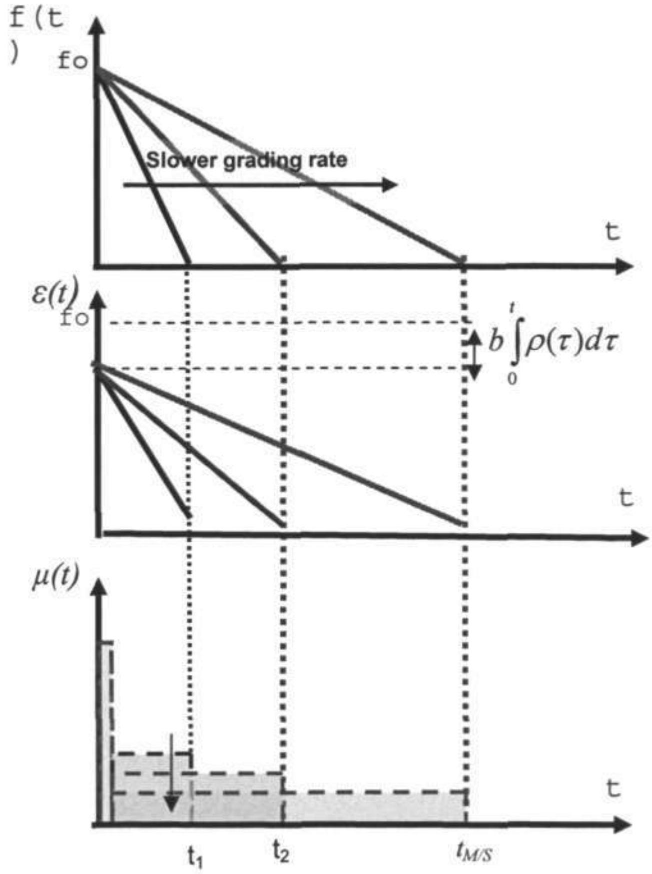

Figure 6.3. Schematic of the effect of grading rate on the residual strain and misfit dislocation distribution in a reverse-graded buffer layer.

Figure 6.3 shows that MDD at $t = 0$ is not affected by increasing grading rate, because f_o is constant in all three cases. At $t > 0$, MDD decreases as the grading rate decreases and the minimum happens at $t = t_{M/S}$, giving the maximum RG thickness. The minimum RG thickness is t_{MB} and it decreases as the total energy in RG increases, which can be achieved by increasing f_o as will be illustrated next.

b) t_{RG} =constant, f_o increases

For a given t_{RG}, the grading rate, $d\frac{f(t)}{dt}$,can be increased by increasing f_o, as illustrated in Figure 6.4. It shows that when f_o (and thus $d\frac{f(t)}{dt}$) increases, the MD density at t=0 increases and MDD at $t > 0$ decreases. This situation is desirable because roughness may be reduced if MD is further away from the SiGe surface. The magnitude of residual strain (the area under the curve) also increases as f_o increases. At some points, the residual strain sign might also change to the opposite direction. The consequence of this situation is explained next.

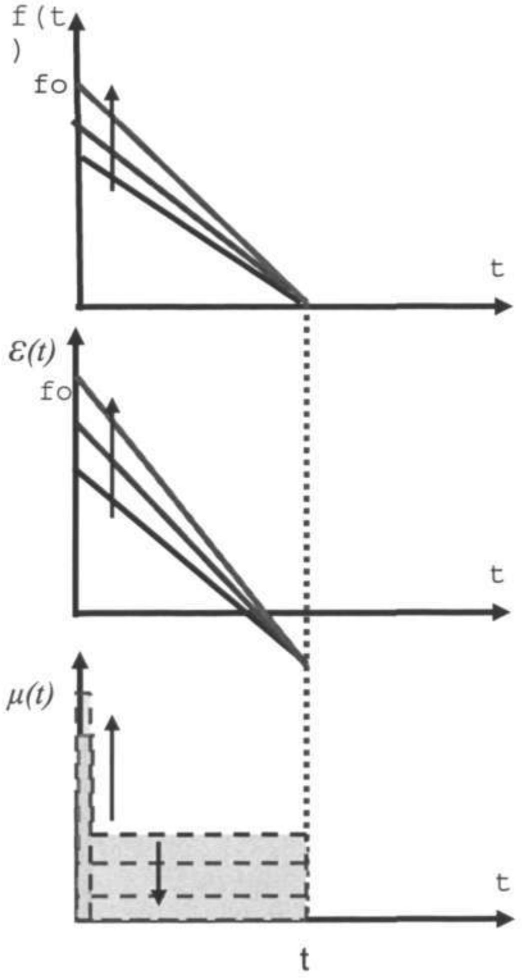

Figure 6.4. Schematic of the effect of f_o on the residual strain and misfit dislocation distribution in a forward-graded buffer layer.

The residual strain distribution depends on the initial mismatch, f_o, grading rate and the amount of strain relieved by dislocations (equations 6.4 and 6.5). Given similar grading rate and amount of strain relaxation, the effect of f_o on the residual strain distribution is illustrated in Fig. 6.5. The calculation assumes all MDs are confined at t=0 where relaxation is maximum and the RG layer is fully strained.

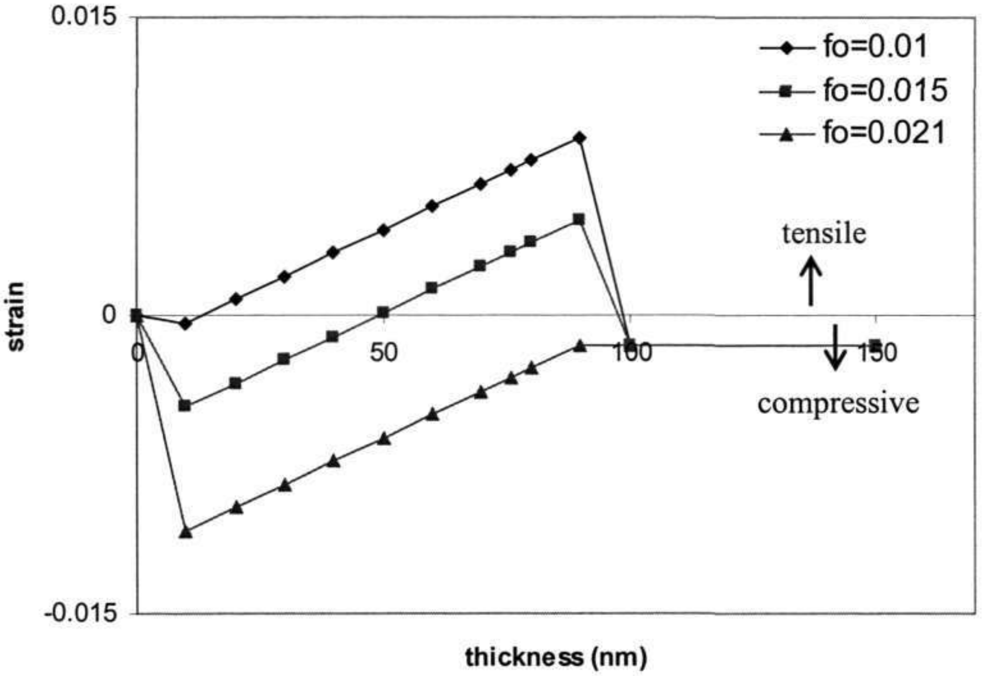

Figure 6.5. The residual strain distribution in a 90-nm RG layer with different f_o.

The tensile and compressive residual strains exert forces in opposite directions on the TD arm (Fig 6.6). When all residual strain is compressive as in the FG case, the TD glide direction is given in Fig. 6.6 (a). When the magnitude of compressive strain is equivalent to the tensile strain, the TD arm is pinned and glide is prohibited (Fig. 6.6 (b)). This is an undesirable situation as relaxation might progress by nucleation of new MDs and the probability of TD annihilation would be reduced. Finally, when all residual strain is tensile, glide still dominates in the opposite direction (Fig. 6.6 (c)). One concern about a tensile residual strain is the tendency of the dissociation of 60° MD into partials [108]. If this reaction dominates, the efficiency of strain relaxation could be reduced because the Burger's vector of the partials is smaller than that of 60° MDs [51,108]. Therefore, the low TDD-strain relaxation might be best realized by using a compressive residual strain.

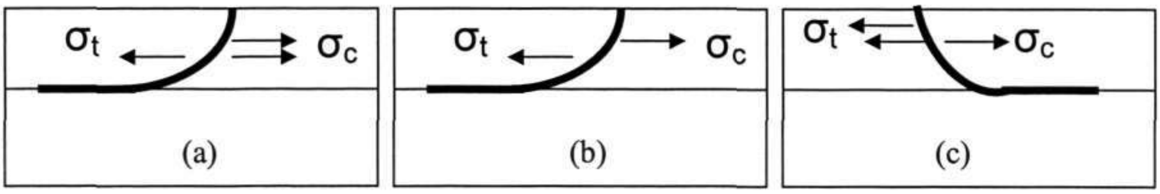

Figure 6.6. Schematics of TD behavior under different ratio of tensile and compressive strains.

Based on the above analyses, the following working hypotheses can then be constructed:

1. Misfit dislocation and residual strain distribution

When a RG buffer is used to introduce relaxation, MDs prefer to nucleate at the RG/Si interface and a residual strain is generated across RG. If most of MDs are confined away from the SiGe surface, roughness could possibly be improved. It is also postulated that a compressive residual strain may assist the reduction of TDD by promoting glide of MD towards the wafer edge and by increasing the possibility of TD annihilation.

2. The thickness range of an effective RG layer is $t_{MB} < t_{RG} < t_{M/S}$.

The minimum RG thickness is t_{MB} and it decreases as the total strain energy in RG increases, which can be achieved by increasing f_o. In other words, the grading rate does not limit the thickness of the buffer layer and f_o , the interfacial mismatch, which is only bound by accessible experimental conditions, is the limiting factor. This advantage can be exploited to grow a thin buffer layer for high quality relaxed SiGe. The maximum thickness is $t_{M/S}$, which is reported experimentally to be less than 100 nm [68]. This thickness range is still 10x thinner than the state-of-the art FG layer, thus providing a strong motivation to demonstrate the RG heterostructure.

6.2. Growth and characterizations of the novel reverse-graded SiGe heteroepitaxy

In this section, the reverse-graded concept is demonstrated in a SiGe/Si heteroepitaxy. The epitaxial growth was done on 8-inch Si (001) substrates in a commercial LPCVD system using SiH_4 and GeH_4 as sources. Before growth the Si substrate was baked in H_2 to promote native oxide desorption. The reversed Ge composition gradient was introduced by ramping down GeH_4 flow during growth to 0 sccm, starting with Ge concentration of around 35%. A SiGe layer with uniform Ge composition was then grown immediately following the buffer growth with constant GeH_4 flow. Different GeH_4 flows were used in order to get different Ge compositions. In some samples, a Si layer was deposited right after the SiGe layer growth by stopping GeH_4 flow. The samples were then characterized by Auger Electron Spectroscopy (AES), high resolution X-ray Diffraction (XRD), Transmission Electron Microscopy (TEM), Atomic Force Microscopy (AFM). A Wright etch of about 70 nm SiGe was carried out to obtain a statistical value of the threading dislocation density in the top SiGe layer with constant Ge composition.

Table 6.1 summarizes our results on different Ge compositions, which are comparable to, or even better than, the previously reported data [141].

Table 6.1. Epitaxial quality of the as-grown relaxed SiGe on RG buffer.

Ge composition (%)	Strain relaxation degree	Threading dislocation density ($/cm^2$)
14	86	3×10^4
25	85	4×10^5
32	86	8×10^5

To illustrate the RG buffer concept, the following discussion concentrates on one sample with ~ 32 % Ge in the relaxed SiGe layer. The thickness of this relaxed SiGe is 170 nm and on top of this layer, a 250 Si layer was grown. The quality of the relaxed SiGe layer grown on this kind of buffer was then characterized in terms of strain relaxation, threading dislocation density, as well as surface roughness. First, the reversed Ge composition profile for the buffer layer is confirmed by AES measurement (Fig. 6.7).

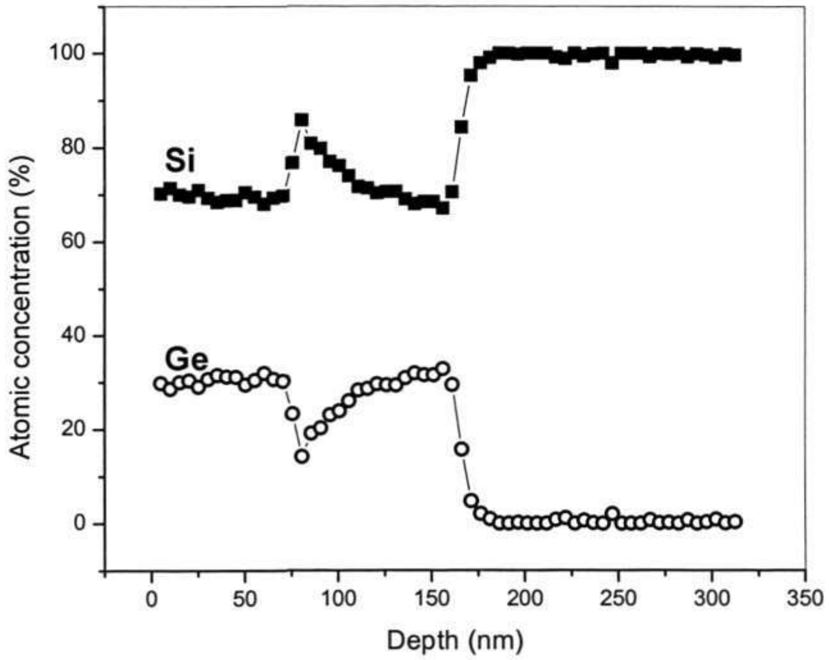

Figure 6.7. AES depth profile of Si/Ge composition for the sample with reversed Ge composition gradient.

Although the Ge composition was designed to decrease from ~35 % at the Si substrate side to 0 at the surface of the buffer layer, due to the limited depth resolution, it shows a decrease from 32% to 14%. Note that the figure shows only part of the top SiGe layer with uniform Ge composition. Secondly, the quality of the uniform Ge layer was investigated.

Strain relaxation in the uniform Ge composition layer was determined by XRD. Figure 6.8 shows (004) XRD rocking curve of the sample.

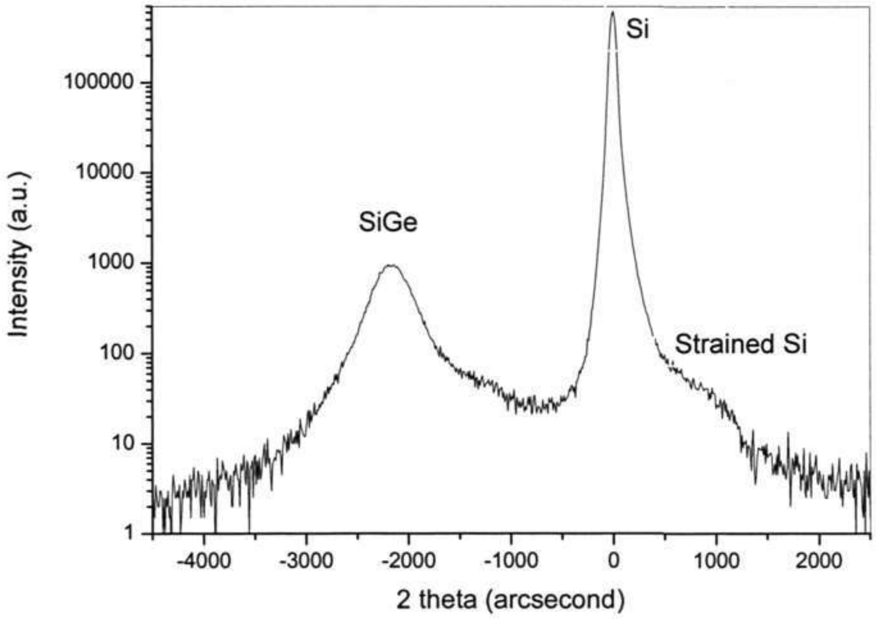

Figure 6.8. Symmetric (004) XRD rocking curve for the RG sample.

The peak at around -2200 arcsec originates from the relaxed SiGe layer, with broad intensity at around -2000 arcsec due to the graded SiGe layers. In combination with a (115) XRD rocking curve (not shown here), the Ge composition could be determined to be 32%, consistent with AES measurements. The strain relaxation degree, $R \equiv \frac{a_{//,SiGe} - a_{Si}}{a_{SiGe} - a_{Si}}$, where $a_{//,SiGe}$ is the in-plane lattice constant of SiGe layer, a_{SiGe} and a_{Si} are the bulk lattice constant of SiGe and Si, respectively, is measured to be 86%. Deviation of Vegard's Law for the lattice constant versus Ge composition was taken into consideration in our analysis. The peak around 1500 arcsec is from the thin Si cap, indicating tensile strain, which was further confirmed by Raman spectroscopy (not shown). The position of the tensile strained Si peak is consistent with the HR-XRD measurement on the relaxation degree if the Si layer is assumed to be fully strained.

Fig. 6.9 shows an AFM image of the sample. The long, regular-spaced cross-hatch pattern indicates uniform strain relaxation by misfit dislocation and few threading dislocations, consistent with the etch experiments. The Root-Mean-Square (RMS) roughness in the AFM image (20x20 μm^2) shown in Fig. 6.9 is 1.11 nm, which is better than the value readily obtained by other buffer techniques [141,142]. This low RMS value confirms our earlier hypothesis that roughness could be reduced since most of the misfit dislocations are located away from the surface. The cross-hatch pattern is believed to result from the introduction of misfit dislocations, and their stress fields impact on the local epitaxial growth rate [141,143].

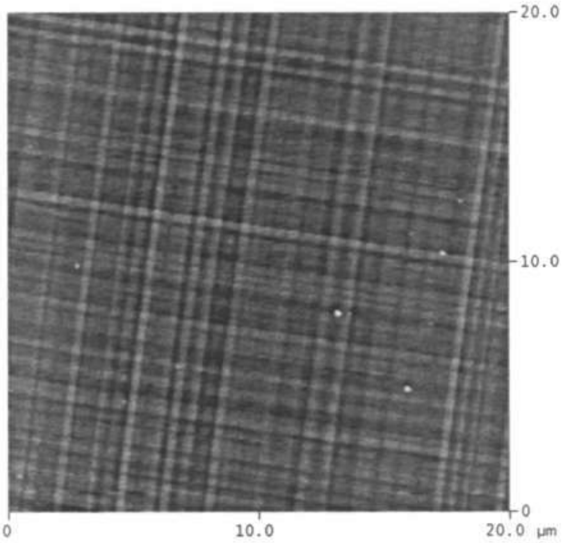

Figure 6.9. AFM image of the sample surface showing a cross-hatch pattern of misfit dislocation network.

The distribution of MDs can be observed from the cross-sectional TEM image of this sample (Fig. 6.10). The inset shows the HR-TEM image of the SiGe buffer layers which is free of defects.

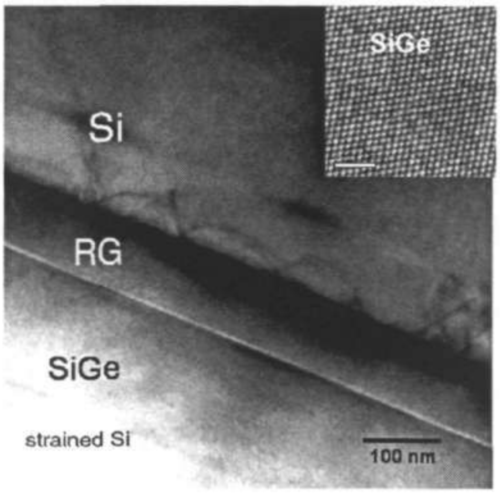

Figure 6.10. Cross-sectional TEM image of the RG heterostructure and the HR-TEM image of the SiGe layer.

The thin SiGe buffer layer (around 90 nm thick) is visible because of the reversed Ge composition gradient, and compositional contrast between the buffer and top SiGe layer. The top SiGe layer is around 170 nm thick. The most striking feature of the TEM picture is the absence of threading dislocations in the relaxed SiGe area. A conservative estimation of the threading dislocation density yields a value $<1\times10^{6}$ cm^{-2}. A Wright etch was performed, and the etched sample was investigated by optical microscope to get a reliable statistical value over larger areas (>0.002 cm^{2}). The threading dislocation density was counted to be 8×10^{5} cm^{-2}. Misfit dislocations can be clearly seen at the interface between the Si substrate and the RG layer, indicating significant strain relaxation. This observation confirms the earlier hypothesis which predicts that TD glide should take place at the RG/Si interface, where the mismatch strain is the highest. In addition, the absence of MD across the RG layer suggests that there should be a residual strain in the RG layer, affirming the metastable hypothesis. The residual strain along the RG depth may act as threading dislocation filters, reducing the threading dislocation density in the upper SiGe layer with uniform Ge composition, as we observed.

To confirm the presence of residual strain in the RG buffer, Reciprocal Space Maps (RSM) of the RG heterostructure with a final Ge concentration of 25% were carried out. A symmetric scan (004) was performed to check for the presence of tilt between SiGe and Si substrate, and the result is shown on Fig. 6.11. The two peaks are aligned parallel to each other, with negligible deviation in Qx, and thus negligible tilt.

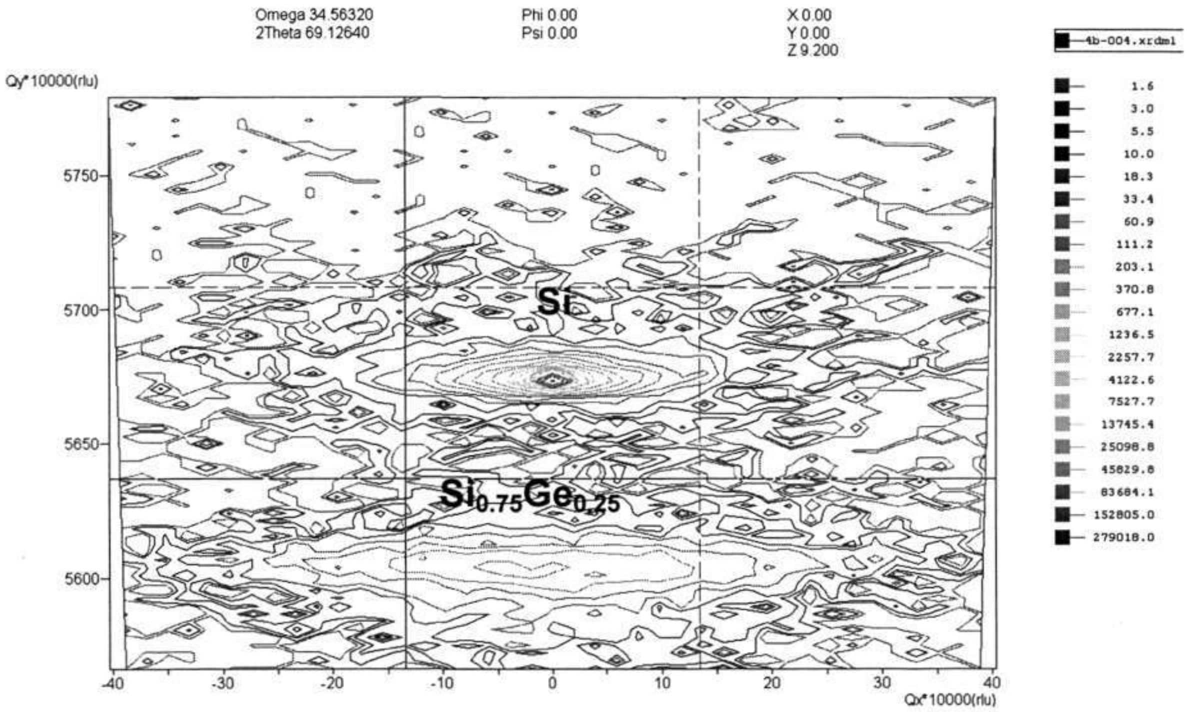

Figure 6.11. A (004) reciprocal space map scan of RG heterostructure.

The asymmetric scan (224), labeled to indicate the main layers in the heterostructure, is shown in Fig. 6.12. The RSM clearly shows the partially-relaxed RG layer, superimposed on the relaxed SiGe peak. Residual strain of the RG layer can be determined by extracting the lattice parameters from RSM. However, since the lattice parameters are a function of Ge content and relaxation, an independent RBS measurement was carried out to determine the Ge content profile across the RG layer.

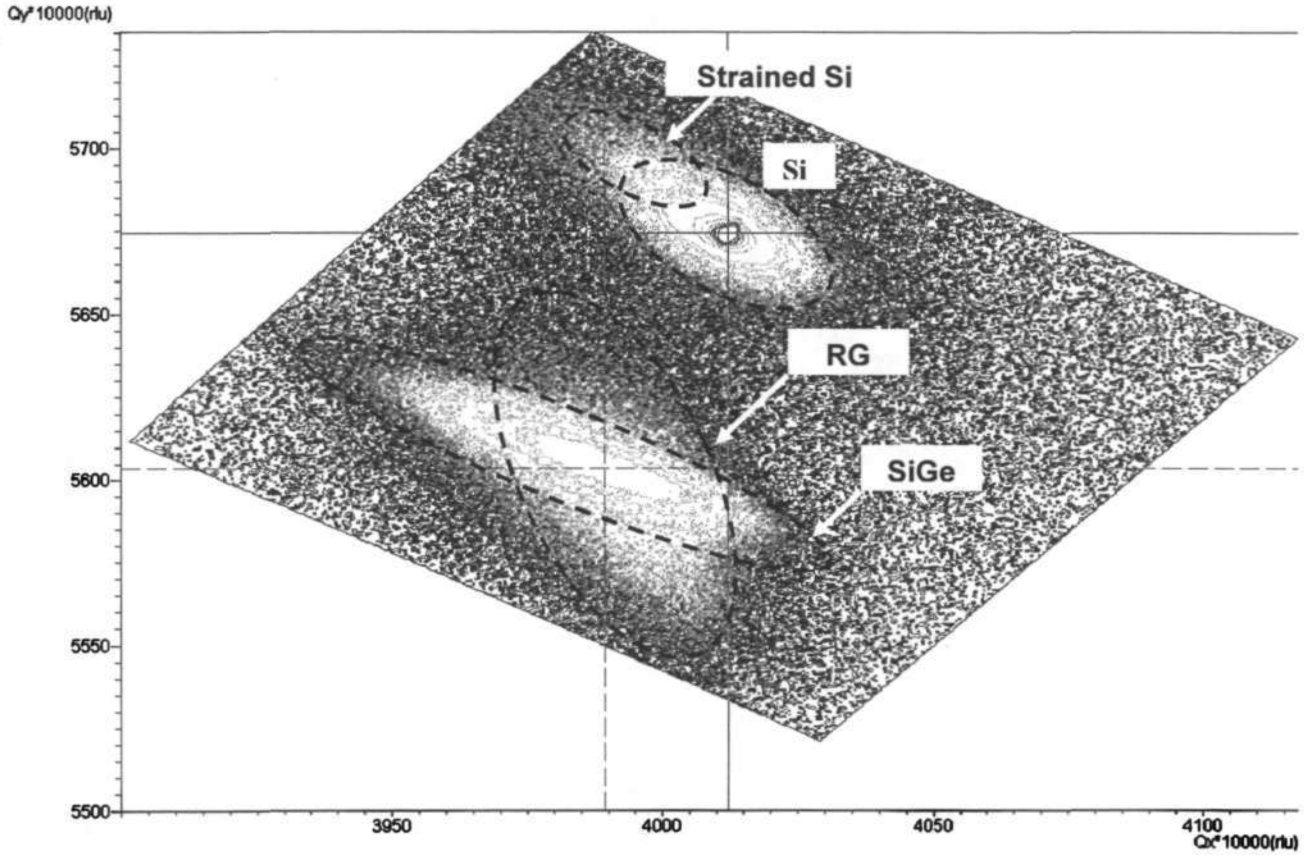

Figure 6.12. A (224) reciprocal space map scan of RG heterostructure.

Fig. 6.13 shows the RBS spectrum of the same sample used for the RSM measurement. Three elements, Si, Ge and O, are detected and their normalized yields vary according to the atomic mass. Trace of oxygen is detected because a thin SiO_2 residue has formed at the strained Si interface. The Ge signal shows the reverse-graded layer and a fit of the above profile results in a linear grading from $x = 0.4$ at the Si/RG interface to $x = 0.15$ at the RG/SiGe interface. The thickness of the RG layer is 90 nm, consistent with the cross-section TEM image (Fig. 6.10). The Ge concentration depth profile from the RBS spectrum is plotted in Fig. 6.14. Both Ge concentration from RBS and lattice parameters from RSM fit are used to calculate the amount of residual strain in the RG layer, and the result is shown in Fig. 6.14. The calculation detail for the RSM experimental fit is given in Chapter 3.

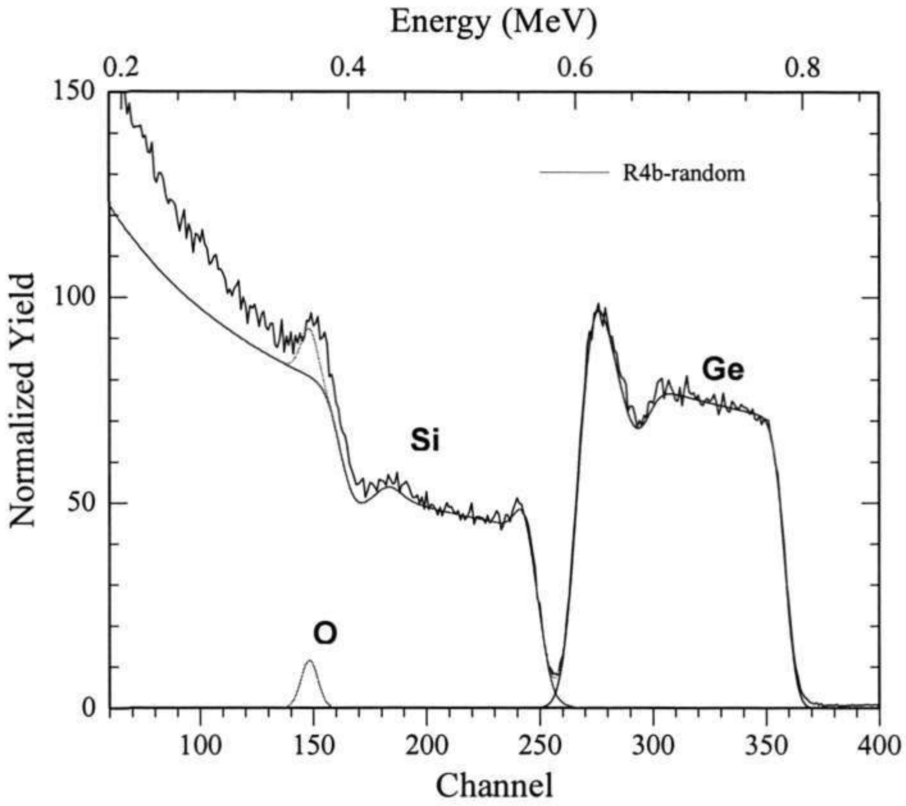

Figure 6.13. RBS spectrum of the RG heterostructure.

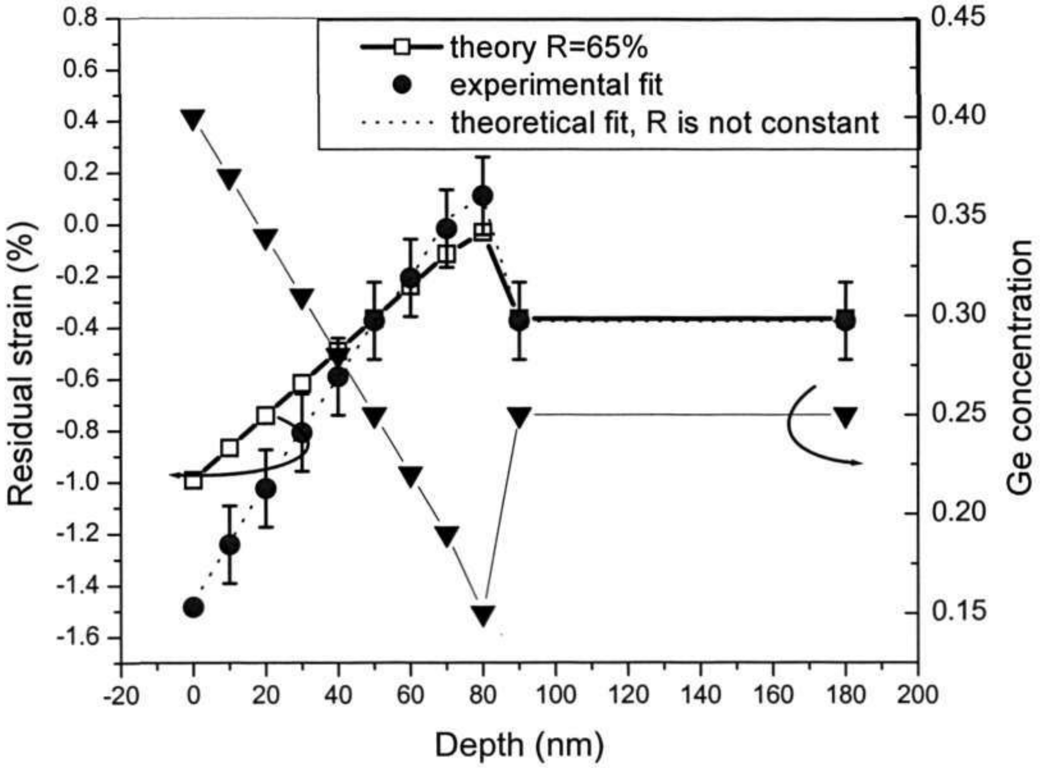

Figure 6.14. Depth-profile of residual strain and Ge concentration inside the RG heterostructure.

The theoretical residual strain fit was calculated by the following equation:

$$\varepsilon(t) = f(t) - (R \times 0.0418x) \qquad (6.7)$$

where R is the degree of relaxation and x is the Ge content of the top uniform SiGe layer. The second term of this equation represents the total amount of strain released by all MDs, or equivalent to the second term in equation (6.1). The open square is the theoretical fit calculated by assuming R to be constant across the RG layer. It is obvious that this fit is close to the experimental results at $t > 40$ nm, but deviates at $t < 40$ nm. This implies that the amount of strain released by the RG layer is not uniform, and more strain is released by the region near the Si substrate. Another theoretical calculation was performed with the assumption that R is not constant and is represented by the dotted line.

Fig. 6.14 shows that the experimental residual strain trend of the RG layer agrees well with the theoretical calculation, and the negative sign shows the strain is compressive, which is expected for growth of SiGe on Si. The top part of the RG layer near the SiGe interface is under tensile strain because the Ge concentration is smaller than that in the uniform SiGe layer. The residual strain of the uniform layer is close to 0, or corresponds to 80% relaxation, consistent with the rocking curve result presented earlier (Fig.6.8) This important observation confirms our earlier hypothesis that a relaxed SiGe can be grown on a metastable (i.e. partially-strained) RG layer as long as MD can be nucleated at the RG/Si interface, shown earlier by cross sectional-TEM (Fig. 6.10).

Fig. 6.14 also shows that the magnitude of the residual strain is considerable (> 1%), and about 10 times larger than that observed in FG layer [86]. The residual strain in RG and FG is compared by the analytical calculations discussed earlier (sub-chapter 6.1). For a simple direct comparison, the grading rate and final relaxation in both buffer systems are assumed to be similar and the effect of the residual strain sign shall be ignored. In this analysis, the FG buffer is linearly graded from 0% Ge to 25% Ge (strain=0.0105) and the RG buffer is linearly graded from 25% Ge to 0% Ge over a thickness of 90 nm. Figure 6.15 clearly shows that the residual strain in RG is larger than FG because MDs are confined at the RG/Si interface and the RG layer is metastable. On the other hand, the uniformly-distributed MDs across the FG layer cause an almost full relaxation of this buffer layer and consequently small residual strain.

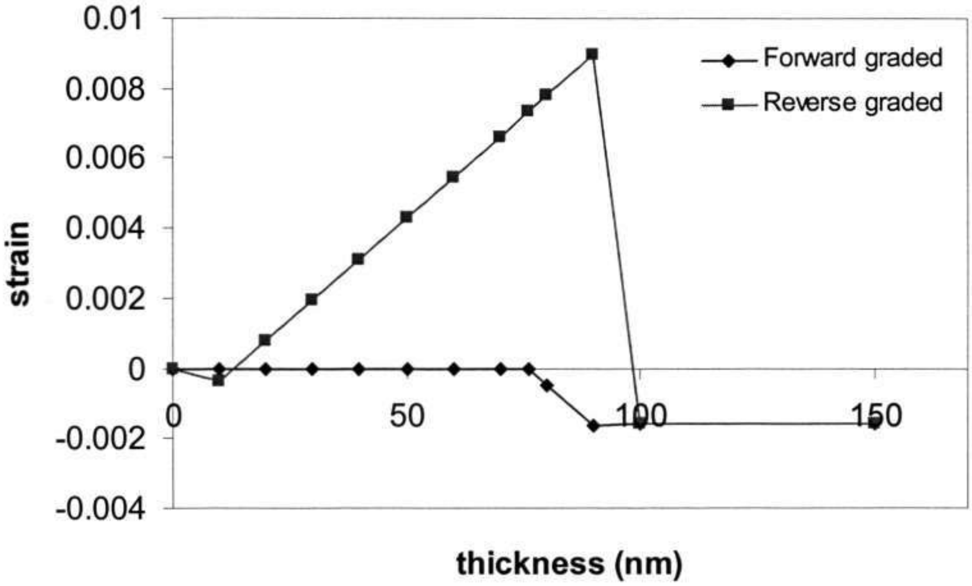

Figure 6.15. Analytical comparison of the residual strain in FG and RG buffers.

In summary, we have demonstrated that a relaxed SiGe layer with smooth surface and low threading dislocation density can be fabricated, using a thin (~90 nm) SiGe buffer with reversed Ge composition gradient. This section has verified two important hypotheses:

1) misfit dislocations are confined at the RG/Si interface as shown by cross-sectional TEM, and

2) the reverse-graded buffer contains a large residual strain as shown by RSM.

The strain relaxation and the TDD reduction mechanisms will be further explored by TEM in the next section.

6.3. Strain relaxation and TDD reduction mechanisms of the reverse-graded heteroepitaxy

It is generally observed that strain can be released through a series of mechanisms, commonly classified as i) roughening of the epitaxial surface film, ii) diffusion across the film/substrate interface, and iii) the introduction of misfit dislocations [51,53]. In our RG system, strain relaxation by roughening of the epitaxial surface film can be ruled-out because the AFM image on Fig. 6.9 shows a flat interface, free from 3-D islands signature of the roughening mechanism [53]. This observation is, in itself, remarkable because growth of SiGe with $x > 0.3$ often results in the roughening of the epitaxial film [17]. Relaxation by diffusion across the film/substrate interface can also be ruled out since the cross sectional-TEM image (Fig. 6.10) shows distinct contrast at the RG/SiGe interface. Figure 6.10 shows the presence of dislocation loops which could release part of the strain. The cross-hatch pattern of the AFM image in Fig.6.9 gives strong qualitative evidence that misfit dislocation is the strain-relief mechanism in the RG heterostructure. A more quantitative justification can be obtained from plan-view TEM images by measuring the average distance between misfit dislocations. In this section, the strain relaxation mechanism of the RG heterostructure would be explained.

Figure 6.16 shows the cross-sectional TEM images taken from locations with different sample thicknesses. As the TEM sample thickness increases (from figure a to d), more dislocations can be observed in the Si substrate because there is more volume contributing to the diffraction. However, no threading dislocations towards the surface can be observed in all images.

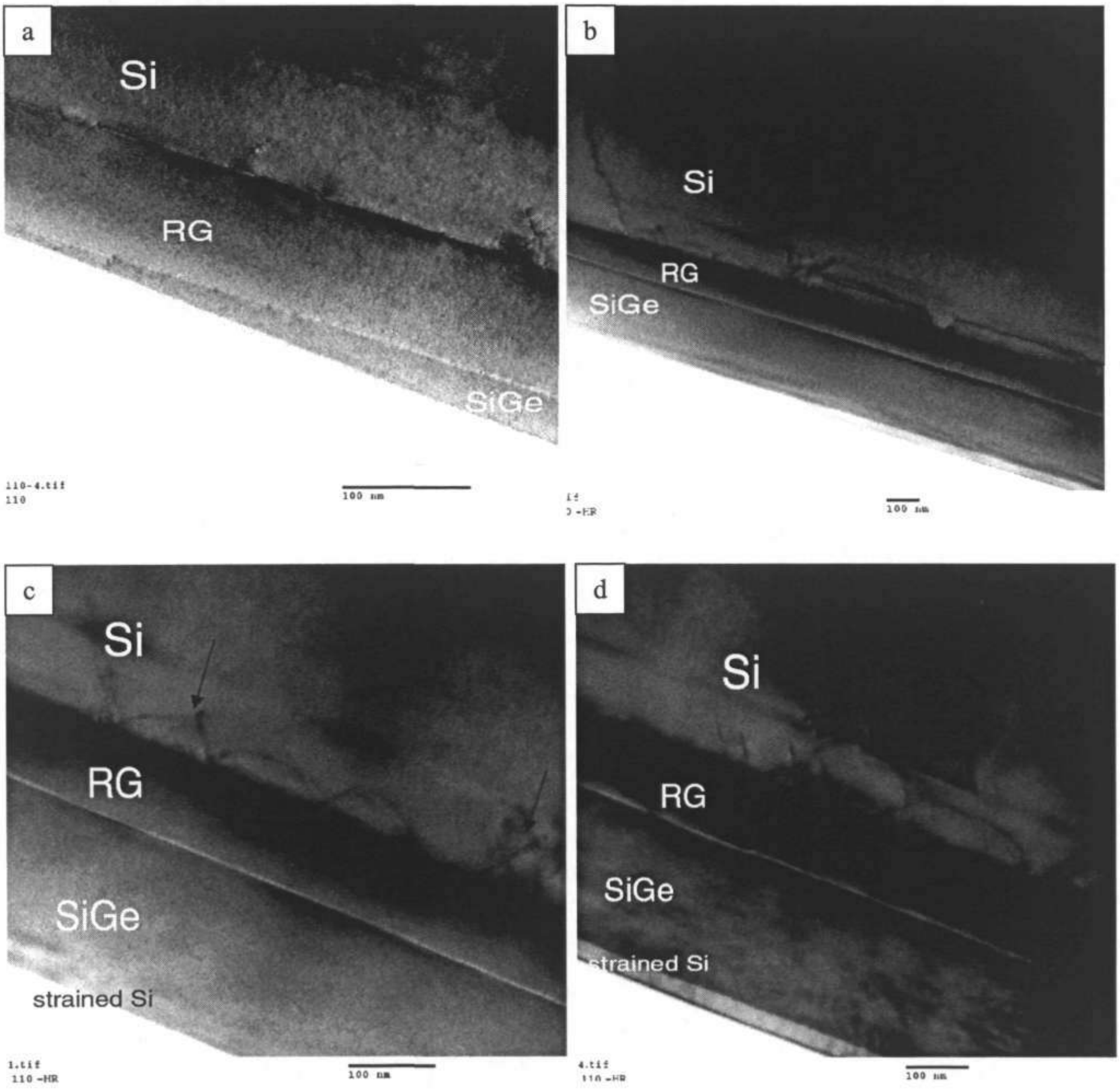

Figure 6.16. Cross-sectional TEM image of the RG heterostructure of different TEM sample thicknesses.

Figures 6.16. c and d show the presence of stacking faults as indicated by arrows. A HRTEM image of the stacking faults is shown in Fig. 6.17

Figure 6.17. HR-TEM image of a stacking faults in the Si substrate

These stacking faults are generated from the movement of Shockley partials, which is the product of 60º MD dissociation. The glide of the stacking faults in at the RG/Si interface may release strain, however since the magnitude of the Burger's vector of the partials is smaller than perfect dislocations, their role in strain relaxation is less significant [108].

The dislocation loops observed in Figs. 6.16 b and c resemble those generated by the activation of Frank-Read sources reported by LeGoues et al. [75] and Lefebvre et al. [76]. A schematic of this mechanism can be found in Fig. 2.8 (Chapter 2). The bowing of the dislocation segment to form a Frank-Read loop takes place when the applied shear stress, τ, exceeds a critical shear stress, τ_c, which is expressed by [108]:

$$\tau_c = \frac{Gb}{2L} \qquad (6.8)$$

where *G* is the shear modulus of the material, *b* is the Burger's vector component of the dislocation, and *L* is the length of the AB segment. L can be estimated to be the average distance between two dislocations, i.e. 82 nm in this case. Taking G to be 66 GPa for $Si_{0.75}Ge_{0.25}$, τ_c is 0.16 GPa, equivalent to a strain of 0.24%. The residual strain calculated from RSM (Fig. 6.14) is much larger than this critical strain, rendering the operation of Frank-Read loop possible.

The amount of strain relaxation by misfit dislocation (ε_{misfit}) can be related to the distance between MDs (L_{MD}) by the following relationship [53]:

$$\varepsilon_{misfit} = \frac{b}{L_{MD}} \tag{6.9}$$

where b is the Burger's vector component of the strain-relieving dislocation. For a mixed 60° misfit dislocation, $b = 0.39/\cos 60 = 0.195$ nm. The plan-view TEM image in Fig 6.18 shows a network of orthogonal MDs at two different interfaces. To understand the contrast in this figure, the cross-section schematic of the plan-view TEM sample is shown as the inset. Since the thinning procedure of the specimen consisted of a) dimpling, which resulted in the wedge shape, and b) ion-milling from the substrate side to keep the top SiGe intact while achieving electron-transparent thickness, the SiGe/RG interface is thinner than the RG/Si interface. During observation from zone axis [001] the thinner SiGe/RG interface appears brighter than the thicker RG/Si interface (Fig 6.18).

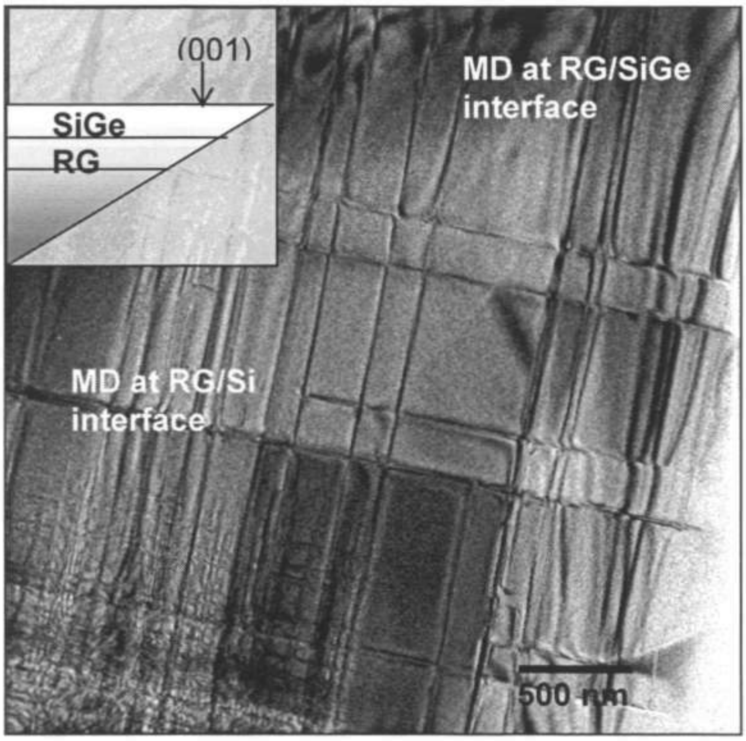

Figure 6.18. Plan-view TEM image of different interfaces in the heterostructure. The inset illustrates the TEM sample thickness and the direction of the electron beam.

It is clear that the MDs are located at both interfaces, but that most of them are located at the RG/Si interface. From the average distance of the MDs, the amount of strain released at the SiGe/RG interface accounts for <10% of the total relaxation of the heterostructure, while those at the RG/Si interface accounts for ~30% and the MFR loops release the remaining 25% strain. In the RG, as the %Ge composition decreases, so does the built-up residual strain and the elastic energy, thus reducing the gliding of existing TDs and preventing the nucleation of new MDs at the RG/Si interface. At the RG/SiGe interface, where the %Ge is changed abruptly from 14% to 25%, a new built-up strain source facilitates the gliding of the residual TDs (coming from the underneath RG/Si interface) as MDs. The MDs generated at this interface are almost exclusively the product of the TDs glide, as the necessary MDs (which is translated to more TDs) to relieve strain have been already nucleated at RG/Si interface. The low MD density at this interface (<

10^4/cm^{-1}) increases TD velocity glide and the annihilation probability with another TD of opposite Burgers vector as studied extensively by Romanov et al.[80-84]. It should be noted that the secondary glide might also take place at the interface where the strain direction changes from compressive to tensile. However, since this reaction must take place in a very short (growth) time before a relatively higher compressive uniform SiGe layer is deposited, the glide at this interface is limited and less significant. On the contrary, the TDs reduction at the RG/SiGe interface is quite efficient. The MD elongation velocity is in fact strongly favored by the low friction and dislocation pinning probability during the TD glide. The average TD glide distance is shown in Fig 6.18 to be > 3 μm, larger than the TEM image width, while the residual TDD in the top SiGe layer, obtained by microscope observation on etched-samples, is on the order of $<10^5$/cm^2 (see Fig 6.19). This is a quite remarkable result for a 90nm thick layer especially when coupled with a 1.1nm surface roughness.

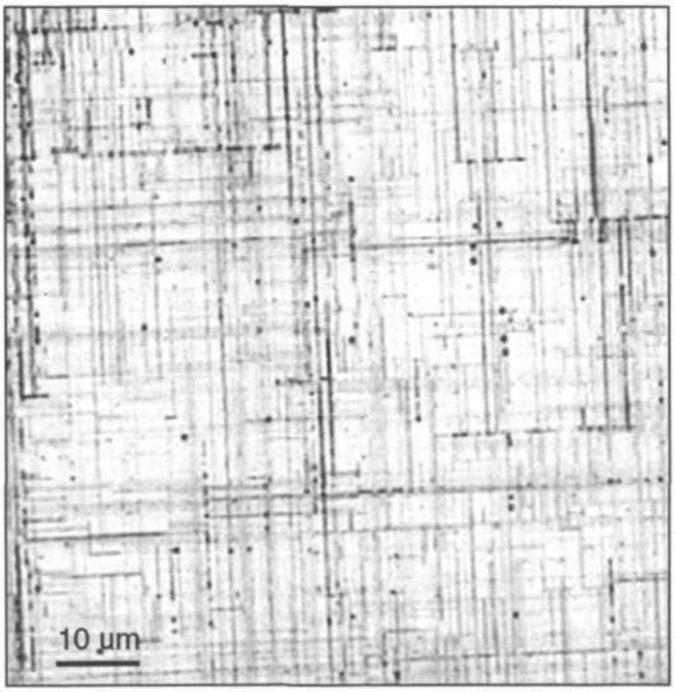

Fig 6.19. Optical microscope image of the relaxed SiGe surface after Wright etch.

In summary, all of the evidence above shows that strain relaxation in the RG heterostructure is accommodated by MDs, formed mostly at the RG/Si interface and some at the SiGe/RG interface, as well as MFR loops in the Si substrate. The decreasing %Ge in the RG decreases the MD generation rate, resulting in lower MD at the second SiGe/RG interface where the residual interfacial tensile strain facilitates 1) long MD glide and 2) TD annihilation. Strain relaxation of lattice-mismatched heterostructures with minimum TDD can thus be achieved by providing two interfaces: the first for MD nucleation and majority strain relief, and the second for TD annihilation.

6.4. Thermal stability of the reverse-graded SiGe heteroepitaxy

It has been established in the previous section that the residual strain in the RG layer plays an important role in reducing the TDD. Previous work has reported that during the high temperature anneals encountered in a typical semiconductor fabrication, strain relaxation of strained SiGe [144], strained Si [119] and diffusion of Ge into strained Si layer (chapter 5.1) might take place. Since the presence of residual strain in the RG layer is needed to achieve low TDD and nucleation of new dislocations might take place during strain relaxation, it is essential to characterize the thermal stability of the residual strain in the RG layer. Moreover, the relaxation of strained Si and Ge diffusion into the strained Si layer may mitigate the carrier mobility gain of the strained Si channel [145,146]. This section is dedicated to the study of the epitaxial quality of the RG structure before and after annealing at various temperatures to explore the feasibility of integrating the RG heterostructure to a real wafer manufacturing environment.

Annealing was conducted at 800, 900 and 1000 °C for 1 minute each in N_2 ambient in a rapid thermal processing (RTP) system. The as-grown and annealed samples were then characterized by Auger Electron Spectroscopy (AES), High-resolution X-ray diffraction (HR-XRD), Transmission Electron Microscopy (TEM) and Atomic Force Microscopy (AFM). A Wright etch of about 70 nm SiGe, followed by Nomarsky microscopy was carried out to obtain statistical data on threading dislocation density in the top SiGe layer with constant Ge composition. The stability of the strained Si layer was investigated by micro-Raman spectroscopy with a laser wavelength of 514.5 nm. For this thermal stability study, the focus is on the sample with 32 % Ge content.

The extent of relaxation of the SiGe layer after annealing was quantified by using a combination of symmetric and asymmetric X-ray rocking curve scans (Fig. 6.20).

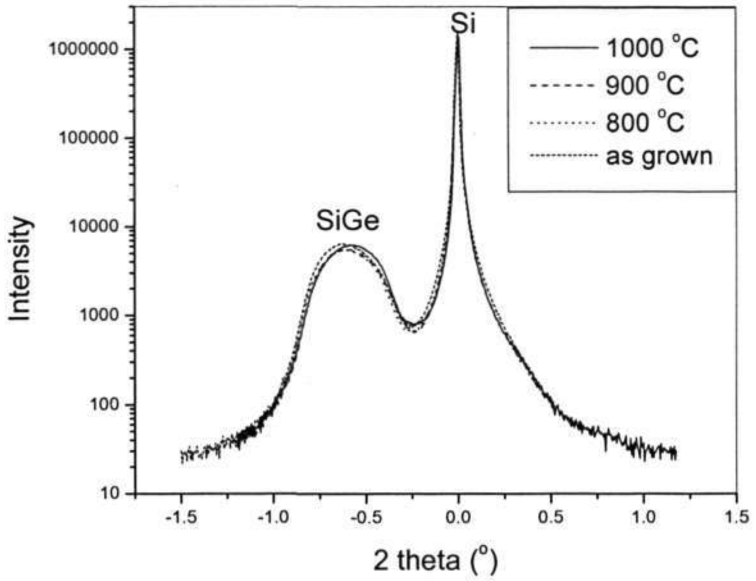

Figure 6.20. Symmetric (004) rocking curves of the samples before and after annealing showing insignificant SiGe peak shift.

The rocking curves reveal two significant peaks attributed to the Si substrate and SiGe layers. The SiGe peaks of the symmetric scans do not shift significantly after annealing, which implies qualitatively that the SiGe layer is stable and experiences no further relaxation after annealing up to 1000 °C. The strain relaxation degree, obtained from a combination of symmetric (004) and asymmetric (115) rocking curves, is tabulated in Table 6.2.

Table 6.2. Epitaxial quality of the samples after anneals at various temperatures.

Annealing condition	Ge content (%)	Relaxation (%)	Roughness (nm)	TDD (cm^{-2})
as grown	32	86±14	1.21	8×10^5
800 °C	32	83±10	1.34	1.13×10^6
900 °C	32	84±8	1.12	1.20×10^6
1000 °C	32	88±9	1.39	1.60×10^6

The relaxation of the as grown and annealed samples shows values between 83 % and 88 %, which is well within the measurement error. The roughness of the samples is < 1.5 nm, and superior to the other buffer methods [143], while the threading dislocation density (TDD) is $< 1.6 \times 10^6/cm^2$, comparable to other buffer systems [25]. The epitaxial quality of this heterostructure is clearly superior to that of uniform composition SiGe directly grown on Si substrate. For example, $Si_{0.68}Ge_{0.32}$ directly grown on Si substrate at temperatures beyond 550 °C show strain relaxation by severe surface roughening [17,53]. Lower growth temperatures can avoid surface roughening, but only at the expense of high TDD (10^7-$10^9/cm^2$) [25,147-149].

Figures 6.21 (a) and (b) show the plan-view TEM images of the sample before and after annealing at 1000 °C, respectively. Some irregular black fringes are formed due to the thickness contrast, originating from the non-uniform TEM sample thickness. An orthogonal misfit dislocation network, with comparable length and density, can be observed on both images, implying no further strain relaxation by misfit dislocations takes place after anneal. This result is consistent with the HR-XRD results described earlier. The saturation of relaxation behavior can be explained by considering the interaction between misfit dislocations. At the later stage of plastic relaxation, a large quantity of misfit dislocations have formed, thus reducing the distance between adjacent misfit segments. When two dislocations of similar Burgers vector are in proximity, there will be a repulsive stress between the dislocations that inhibits further glide [51]. As the dislocation propagation is inhibited, the excess strain in the system cannot be relieved. To further relax the SiGe layer, one could increase the thickness of the SiGe layer. However, this successful preliminary study suggests a possibility of growing good quality high-lattice mismatched epitaxial films with total thicknesses of less than 0.5 μm. As a comparison, to obtain a relaxed $Si_{0.7}Ge_{0.3}$ by using forward graded buffer layer, both equilibrium calculations and experimental results showed that at least 5 μm of graded and relaxed SiGe layer must be grown [86,142].

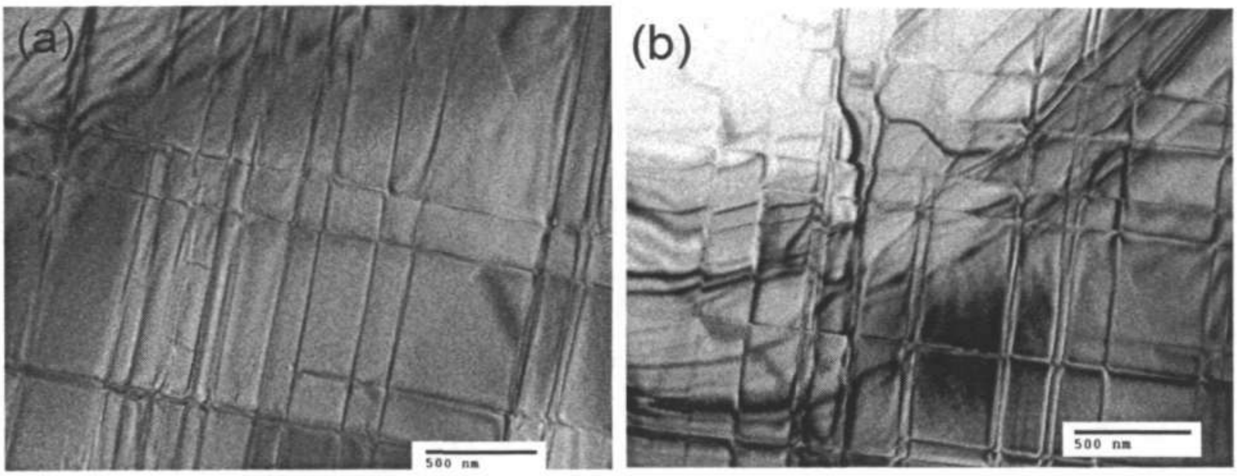

Figure 6.21. Plan-view TEM image of the sample (a) before and (b) after anneal at 1000ºC showing no change in misfit dislocation density and length.

The dislocation behavior inside the epitaxial layer is observed by TEM cross-section in Fig. 6.22, which shows the Si substrate, reversed graded (RG) layer, relaxed SiGe layer and a thin strained Si layer.

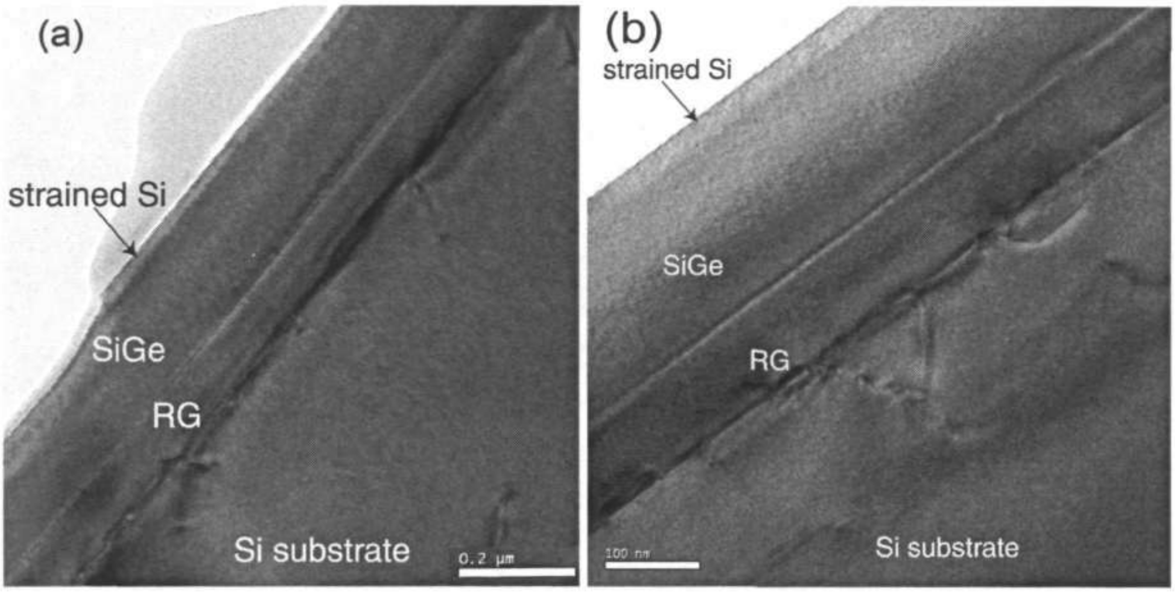

Figure 6.22. Cross-sectional TEM image of the sample (a) before and (b) after anneal at 1000°C showing dislocations only at the RG/Si interface.

The darker region at the Si/RG interface is associated with a large number of misfit dislocations, which creates a dislocation-induced strain field and diffraction contrast. It is noted that the dislocations are contained at the interfaces, and not distributed across the graded layer as in the case of forward grading [75]. It is postulated that the high-mismatch interface provides a much more favorable site for dislocation nucleation due to the accumulation of free energy, and the residual stress within the RG layer exerts forces that suppress the upwards propagation of threading dislocations. Fig. 6.22 (b) shows the cross-section TEM image of the sample annealed at 1000°C, wherethe accumulation of defects at the RG/Si interface is evident. Even though more defects can be observed in the Si substrate they do not thread towards the top SiGe layer. This observation implies that the residual stress in the RG layer remains stable after annealing at 1000 °C, and the TDD on the top SiGe does not increase significantly, confirming our etching experiment (Table 6.2). The stability of the residual strain in the RG layer may be due to the reduced driving force for dislocation nucleation after a substantial amount of strain has been released.

The thermal stability of the strained Si layer was also investigated by Raman spectroscopy. Figure 6.23 shows the Raman spectra of the sample before and after annealing at various temperatures.

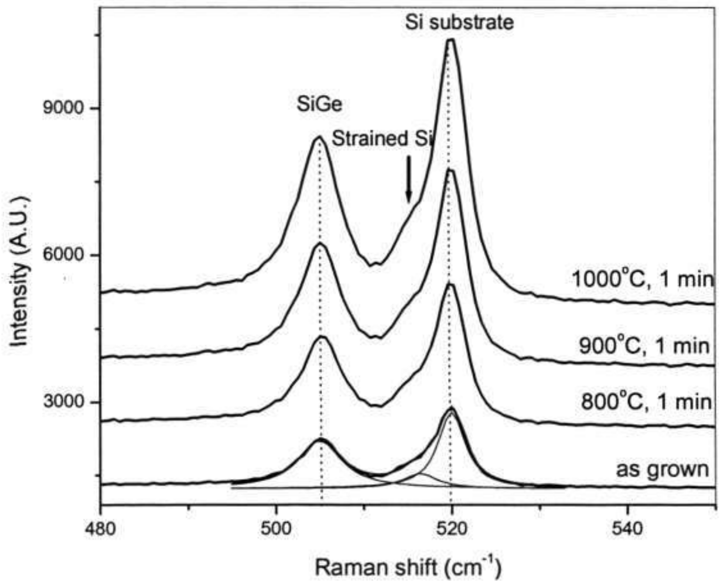

Figure 6.23. Raman spectra of the samples before and after annealing.

According to the position of the strained Si peak, the amount of strain in strained Si is quantified to be 0.7 % by using the b for strained Si obtained in Chapter 4. It is obvious that the position of strained Si peaks of all samples remain fixed, implying that strain is conserved after annealing. Moreover, the intensity of the strained Si peaks remain relatively unchanged after annealing, implying that the thickness of strained Si layer was not reduced by Ge out-diffusion. This observation was confirmed by our SIMS experiment (not shown), where Ge diffusion into Si is estimated to be < 5 Å, which is within the crater-depth measurement error. Similar results have also been reported previously [120]. Finally, on Fig 6.22 (b), the clear interface between strained Si and relaxed SiGe indirectly confirms the negligible Ge diffusion.

In summary, we have investigated the thermal stability of the reverse-graded buffer/ relaxed SiGe/ strained Si heterostructure under various annealing conditions. HR-XRD shows no additional relaxation of the heterostructure after annealing up to 1000 °C. No additional dislocation nucleation and propagation can be observed by cross-section and plan-view TEM, as well as threading dislocation-count by etching. In addition, the strained Si layer is not relaxed after annealing nor degraded by Ge diffusion. Finally, the stability of this heterostructure may imply that the film stack has reached a near-equilibrium condition and the RG heterostructure is a suitable candidate for the growth of strained Si and/or Ge layers for future CMOS devices.

6.5. Chapter Summary

In this chapter, a novel concept of reverse grading in SiGe heteroepitaxy system has been proposed and demonstrated. The summary of this chapter is as follows:

1. It is postulated that a thin graded buffer layer can be realized by using the novel reverse-graded concept, under metastable conditions. If most misfit dislocations are confined at the RG/substrate interface and a significant residual strain is present, a relaxed epitaxy layer with low TDD and roughness can be grown on top of this buffer layer.
2. This idea is demonstrated successfully in a SiGe/Si heteroepitaxy, where a 90 nm, 85% relaxed SiGe has been grown with a TDD of ~10^5/cm^2 and a roughness of 1.1 nm.
3. Strain relaxation takes place by misfit dislocations at the RG/Si interface and inside the Si substrate, which is formed by MFR mechanisms. Evidence for residual strain is shown by RSM and its role in TDD reduction has been explained.

4. Finally, this heterostructure is stable up to 1000°C with no further relaxation in SiGe and strained Si.

In conclusion, all of the above investigations favor the implementation of this novel heterostructure for future strained-channel transistors.

Chapter 7:

A novel SiGe/SiGeC buffer layer for low-dislocation-density relaxed SiGe

Strain relaxation of relaxed SiGe on a novel SiGeC/SiGe superlattice buffer layer is demonstrated after annealing at high temperatures. The idea stems from the fact that SiGeC decomposes into SiC precipitates when annealed at 900 °C and above [49,50]. A combination of SiC precipitates and strain field in the superlattice are thought to provide enough force to pin threading dislocations. Furthermore, the different lattice constants of SiC and the SiGe matrix may create coherency strain that transforms the epitaxial mismatch strain into localized discrete strain, resulting in a net reduction of misfit dislocation density. The growth and characterization of this heterostructure is presented in sub-chapter 7.1. An unusual phenomenon of strain relaxation accompanied by TDD reduction has been discovered and associated with the formation of SiGeC domains. In sub-chapter 7.2, the role of SiGeC domains in TDD reduction is further explained by plan-view TEM study.

7.1. Investigation of threading dislocation reduction phenomenon in SiGe/SiGeC heterostructure

It is generally observed that strain can be released through a series of mechanisms, commonly classified as i) the roughening of the epitaxial surface film, ii) the diffusion across the film/substrate interface, and iii) the introduction of misfit dislocations [51,53]. Strain relaxation by misfit dislocation is usually observed in the growth of high quality relaxed epitaxial layers, such as relaxed $Si_{1-x}Ge_x$ for the subsequent growth of strained Si for sub 90 nm transistors [25,34]. Nevertheless, the termination of the misfit dislocations at the interface forms threading dislocations, which was found to degrade room temperature mobility [7] and increase leakage current [8]. As strain relaxation progresses via misfit dislocation generation, the threading dislocation density (TDD) increases as well [17,25,51,53]. The present work shows a reverse trend, i.e. the threading dislocation density *decreases* as the strain relaxation increases. This phenomenon is observed on a $Si_{0.77}Ge_{0.23}$ layer grown on top of alternating $Si_{0.77}Ge_{0.23}$/ $Si_{0.76}Ge_{0.23}C_{0.01}$ buffer layers. In addition, after annealing at 1000°C, the top $Si_{0.77}Ge_{0.23}$ layer relaxes to 85 % of its bulk lattice constant with a TDD of ~10^4/cm^2, which, to our knowledge, is one of the lowest dislocation density ever attained [17,25,51,53,78].

The epitaxial growth of the alternating $Si_{0.77}Ge_{0.23}$/$Si_{0.76}Ge_{0.23}C_{0.01}$buffer layers was carried out on eight-inch Si (001) substrates in a commercial Low Pressure-CVD system. After baking the Si substrate in H_2 for desorption of native oxide, the first layer of $Si_{0.77}Ge_{0.23}$ was grown followed by another layer of $Si_{0.76}Ge_{0.23}C_{0.01}$; the Ge and C concentrations were obtained using high resolution x-ray diffraction (XRD) by fitting symmetric [004] and asymmetric [115] rocking curve scans. The thickness of both the buffer and the uniform $Si_{0.77}Ge_{0.23}$ layers was determined from cross-section transmission electron microscopy (TEM) images. The schematic of the heterostructure is shown Fig. 7.1.

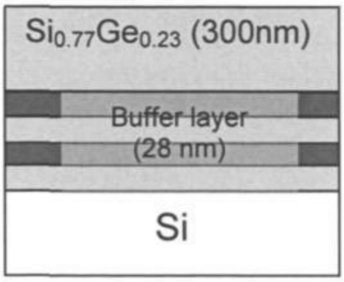

Figure 7.1. The schematic of the sample with a buffer layer consisting of SiGe/SiGeC alternating layers.

The sample was cut into several pieces and annealed at temperatures ranging between 800 and 1000 °C for 1 hour in a N_2 atmosphere. A Wright etch of about 50 nm $Si_{0.77}Ge_{0.23}$, followed by observations by Nomarsky microscopy were carried out to get a statistical value of the threading dislocation density in the top SiGe of all samples. For each annealed sample, at least 3 pieces were etched separately and TDD were counted repeatedly. Secondary ion mass spectroscopy (SIMS) analyses were performed on selected samples to obtain the compositional distribution of Ge and C before and after annealing. High-resolution (HR) TEM investigations were performed at 200 kV on a JEOL JEM-2100F field emission electron microscope. Lattice parameters, here reported in Å, were determined repeatedly to check the hysteresis of electromagnetic lenses, obtaining values accurate to better than ± 0.1 %.

Figure 7.2 shows the [004] rocking curves of the samples at different annealing temperatures. Both the right-shift and the broadening of SiGe peak after annealing indicate the relaxation of the SiGe layer and the presence of misfit dislocations respectively [107]. By using both [004] and [115] scans, the amount of strain relaxation as defined by: $R \equiv \frac{a_{//,SiGe} - a_{Si}}{a_{SiGe} - a_{Si}}$, where $a_{//,SiGe}$ is the in-plane lattice constant of $Si_{1-x}Ge_x$

layer, and a_{SiGe} and a_{Si} are the bulk lattice constants of $Si_{1-x}Ge_x$ and Si, respectively was quantified. Figure 7.2 clearly shows that the relaxation increases as the annealing temperature increases and, after annealing at 1000°C, about 85 % relaxation is observed.

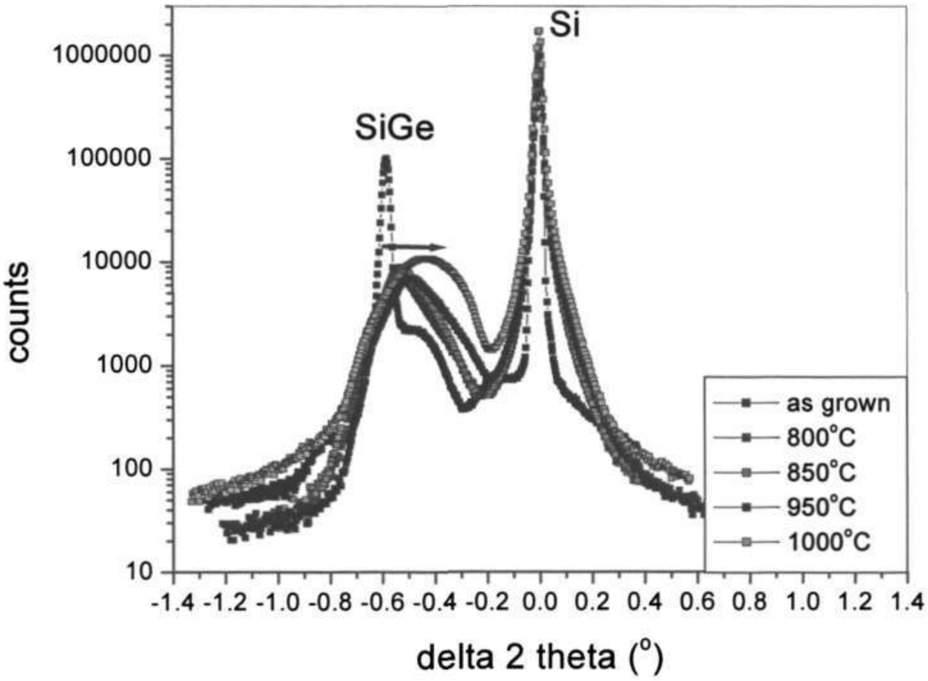

Figure 7.2. High resolution XRD spectra of the sample, showing a right-shift of SiGe peak after annealing at various temperatures.

The trends of relaxation degree and TDD *vs* annealing temperature are plotted in Fig. 7.3. It shows that when annealing at T < 800°C, TDD increases as relaxation increases, as expected in the case where strain relaxation is mainly accommodated by the formation of misfit dislocations terminating as threading dislocations [51]. However, at anneal T > 800°C, TDD decreases as relaxation increases. This remarkable observation prompts us to infer that the role of misfit dislocations in releasing strain has been reduced beyond this annealing condition.

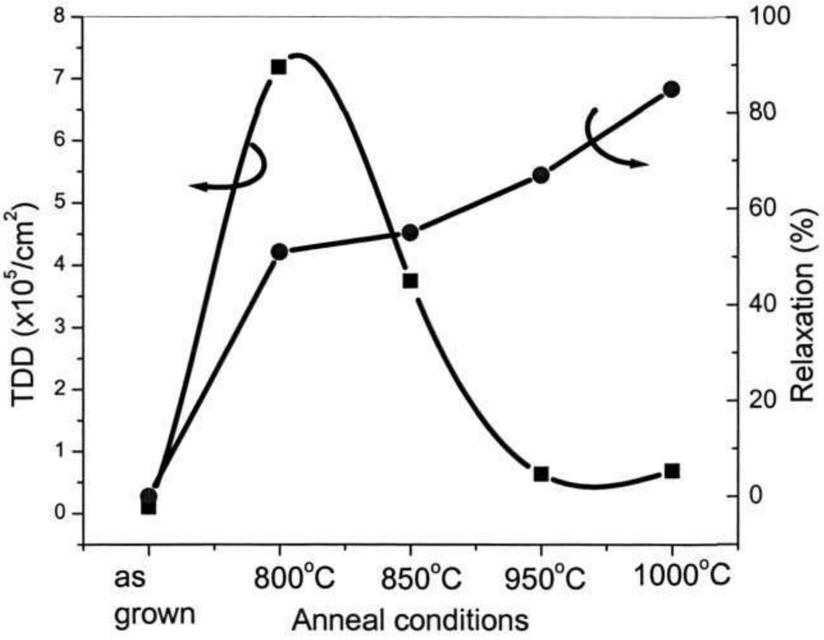

Figure 7.3. Threading dislocation density (TDD) and degree of relaxation of the sample after annealing at various temperatures.

To further investigate the relaxation mechanism, cross-sectional TEM was performed on the samples before and after annealing at 800 and 1000°C. The low-magnification TEM image of the as-grown sample (Fig. 7.4(a)) shows a defect-free SiGe layer. The HRTEM image of the as-grown sample (Fig. 7.4(b)) clearly shows alternating layers of strained $Si_{0.77}Ge_{0.23}$ / $Si_{0.76}Ge_{0.23}C_{0.01}$ where the interfaces appear to be almost free of defects.

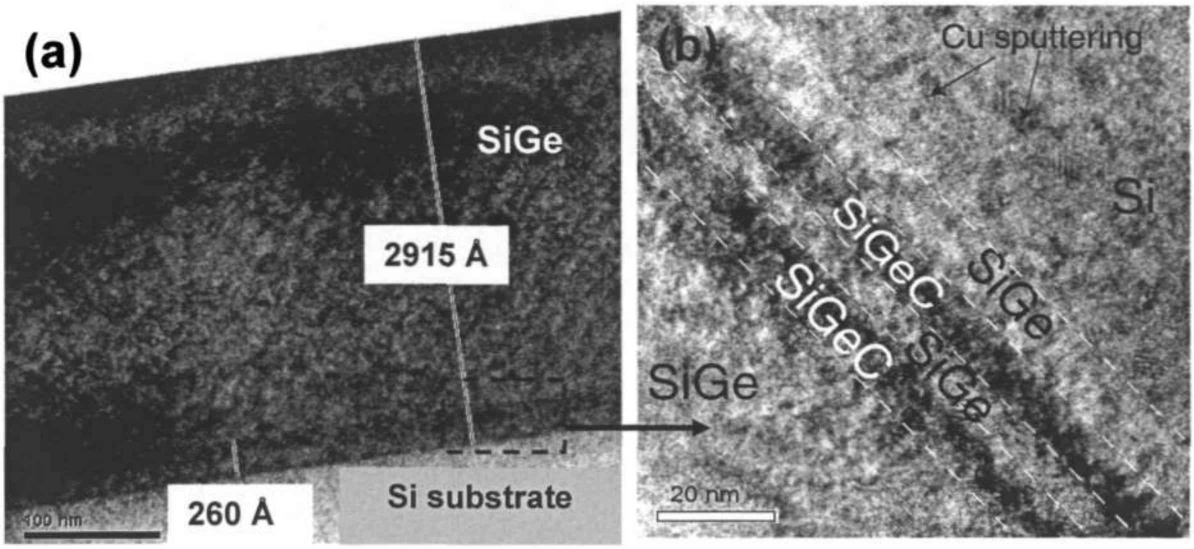

Figure 7.4. (a) Low magnification TEM image of the as-grown sample and (b) a bright-field TEM image of the SiGeC/SiGe alternating buffer layer.

After the sample was annealed at 800°C, dislocations were generated at the $Si_{0.77}Ge_{0.23}$/Si interface and propagate upwards as threading dislocations. A statistical TDD estimation based on several TEM images (an example of which is shown in Fig. 7.5) yields a value of 7.68 x $10^5/cm^2$, which is in good agreement with the etching experiment. The alternating layers of strained $Si_{0.77}Ge_{0.23}$ / $Si_{0.76}Ge_{0.23}C_{0.01}$ are clearly shown in the inset of Fig. 7.5. Based on these observations we can conclude that the strain relaxation of the $Si_{0.77}Ge_{0.23}$ layer at 800°C is mainly accommodated by the formation of misfit dislocations, as expected.

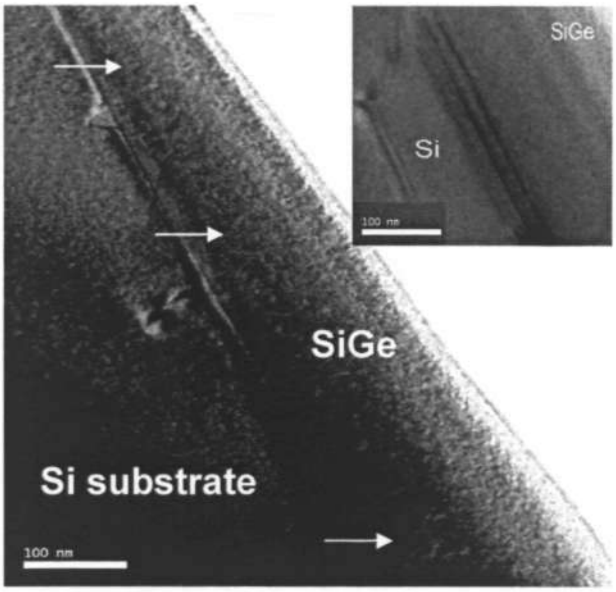

Figure 7.5 Low magnification TEM image of the sample after anneal at 800°C with threading dislocations indicated by arrows. The inset shows the presence of SiGeC/SiGe alternating buffer layer.

On the other hand, the TEM investigation of the sample after annealing at 1000°C (Fig. 7.6(a)) shows a notable absence of dislocations and a complex contrast at the interface of the Si and buffer layer. SIMS measurement (not shown) confirms that C was not lost after annealing. The HR-TEM image of the interface (Fig. 7.6(b)) reveals whitish, grey and black contrasts, which may correspond to small domains exerting different amounts of stress to the matrix. A few dislocations can also be observed as indicated by parallel lines. Selected area electron diffraction (SAED) of the interface regions along [110] reveals at least one weak satellite spot at high angles, and at some reflections, two satellite spots can be observed (inset of Fig.7.6(b)). The satellite spots are aligned with the main diffraction spots, implying coherency with the matrix. The coherency between the domains and the matrix is further confirmed by the absence of Moire fringes in dark-field TEM images (not shown). In Fig. 7.6 (b), the lattice constant of reflection 1 is indexed to be 5.47 Å, which corresponds to the $Si_{0.77}Ge_{0.23}$ matrix (85 % relaxed) while, the lattice constant of reflection 2 is indexed to be 5.45 Å, which may correspond to Si_{1-x-}

$_{y}\mathrm{Ge}_{x}\mathrm{C}_{y}$ (with $x \leq 0.23$ and $y \leq 0.01$). Finally, the lattice constant of reflection 3 is indexed to be 5.44 Å, close to pure Si. The presence of pure Si reflections can be explained by inter-diffusion of Si and SiGe/SiGeC.

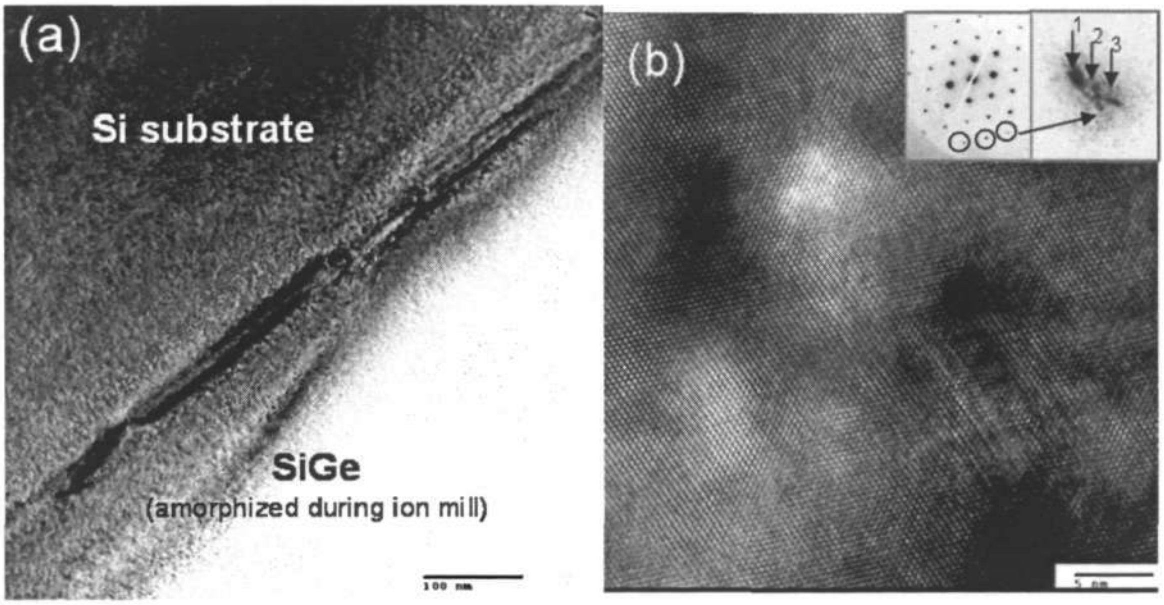

Figure 7.6. (a) Low magnification TEM image of the sample after anneal at 1000°C, and **(b)** HR-TEM image of the sample's interface after anneal at 1000°C with misfit dislocations indicated by arrows. The inset shows the selected area electron diffraction pattern of the interface region, showing satellite spots of the domains.

Further evidence of the presence of domains is shown by the plan-view TEM image (Fig. 7.7), taken normal to [001] plane. Unlike the conventional misfit dislocation network, where the dislocations run in two orthogonal directions, an irregular dislocation network is observed in Fig. 7.7. In the presence of domains, a gliding misfit dislocation may climb or cross-slip around the domains instead of gliding pass through it as a huge amount of energy would be required [150].

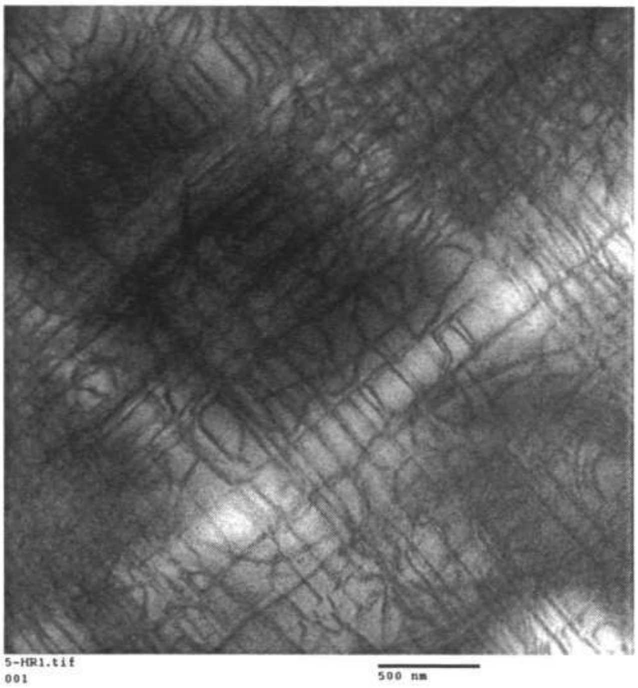

Figure 7.7. Plan-view TEM image of the sample showing an irregular dislocation network.

Earlier experimental work has reported the formation of β-SiC in SiGeC after annealing at 900 °C [49,50]. However, the indexing of diffraction pattern satellites does not match the lattice constant of β-SiC (a = 4.36 Å). FTIR observation does not reveal the β-SiC peak in all annealed samples (not shown). Thus, these phase-separated domains that we have observed do not appear to be SiC. The reason behind the retardation of SiC formation presently remains unclear. It could be due to the lowering of the average C content in the buffer due to homogenization, which reduces the driving force for SiC precipitation. It is also likely that the retardation of SiC formation is directly related to the formation of SiGeC domains, a mechanism that still requires further investigation. It is possible that the strain-field fluctuations due to the SiGeC/SiGe superlattice and/or existing misfit dislocation have caused non-homogenous Ge or C diffusion which forms the SiGeC domains.

From all of the above observations, it is clear that the initial $Si_{0.77}Ge_{0.23}$ / $Si_{0.76}Ge_{0.23}C_{0.01}$ alternating layers have been homogenized after annealing at 1000°C, probably facilitated by Ge and C diffusion. We propose that the strain relaxation of the top $Si_{0.77}Ge_{0.23}$ at 1000ºC is accompanied by a reduction in TDD because of the formation of coherent $Si_{1-x-y}Ge_xC_y$ domains, which could be facilitated by the decomposition of the alternating layers. These domains may assist the relaxation of the top $Si_{0.77}Ge_{0.23}$ layer by transforming the epitaxial misfit strain to discrete strain at the interface of the domains and the $Si_{0.77}Ge_{0.23}$ matrix, as shown by the contrast of HR-TEM images(Fig. 7.6(b)). In addition, the $Si_{1-x-y}Ge_xC_y$ domains may provide the interface for the termination of misfit dislocations, which could be generated during the earlier stage of strain relaxation. Thus, the relaxation of lattice-mismatched $Si_{0.77}Ge_{0.23}$ on Si with a reduction in TDD, can be explained by the dual role of $Si_{1-x-y}Ge_xC_y$ domains, i.e. creating discrete strains at the interface between $Si_{1-x-y}Ge_xC_y$ and $Si_{0.77}Ge_{0.23}$ matrix and blocking the propagation of misfit dislocations. It should also be noted that misfit dislocations may release part of the misfit strain. However, a rough estimation of misfit dislocation density from plan-view TEM images shows that the maximum strain relaxation released by misfit dislocation is 40 %. It is then safe to conclude that the remaining strain is released by the discrete strain relief of the $Si_{1-x-y}Ge_xC_y$ domains.

In conclusion, the relaxation of lattice-mismatched $Si_{0.77}Ge_{0.23}$ on Si accompanied by a reduction in TDD has been observed. HR-TEM study shows the absence of dislocations at $Si_{0.77}Ge_{0.23}$/Si interface and the presence of $Si_{1-x-y}Ge_xC_y$ (with $x \leq 0.23$ and $y \leq 0.01$) domains in $Si_{0.77}Ge_{0.23}$ matrix. We infer that the low TDD-relaxation is a consequence of the dual role of the domains, that first, transform the epitaxial misfit strain into discrete strains, and second, block the propagation of misfit dislocations.

7.2. The role of SiGeC domains on the threading dislocation reduction

In this sub-chapter the role of SiGeC domains in reducing TDD is investigated by plan-view TEM observations. A bright-field plan-view TEM image along [001] focused at the level of the Si/buffer interface is shown in Fig. 7.8 (a). Even though most of the dislocations are aligned orthogonally, a few misoriented dislocations are visible. Dark-field images of the same area, obtained by selecting different ***g*** reflections, are shown in Figures 7.8 (b-d). According to the ***g.b*** invisibility criteria, pure edge dislocations with $\boldsymbol{b}=\frac{a}{2}<110>$ or $\frac{a}{2}<1\bar{1}0>$ are invisible when one of the 220 reflections (i.e. 220 or $\bar{2}20$) is selected, and invisible for the other 200 reflection. 60° misfit dislocations, on the other hand, are always visible when either 220 reflections is selected and may be invisible when the 400 reflection is selected. Figures 7.8 (c) and (d) show that some dislocations disappear when reflections 220 or $\bar{2}20$ are selected, but become visible when 400 reflection is selected. This observation suggests that these are pure edge dislocations. On the other hand, most of the dislocations are always visible, but invisible using the 400 reflection; this last observation suggests these are 60° misfit dislocations. Thus, the misfit dislocation network consists of pure edge dislocations and a majority of 60° misfit dislocations.

Since pure edge dislocations are widely-known to release mismatch strain due to the large Burger's vector [63-64], it is possible then to estimate the average distance of pure edge dislocations to calculate the amount of strain relief. The estimation was not straightforward because the pure edge dislocations are short and the density is relatively low (as observed from Fig. 7.8 (a) and other images, not shown). The closest average distance between two rows of pure edge dislocations is roughly estimated to be at least 500 nm, corresponding to a 8% strain relief. Since the total relaxation is 85%, the strain relief by pure edge dislocation is not dominant. Nevertheless, its role in the TDD reduction is very crucial, as will be elaborated below.

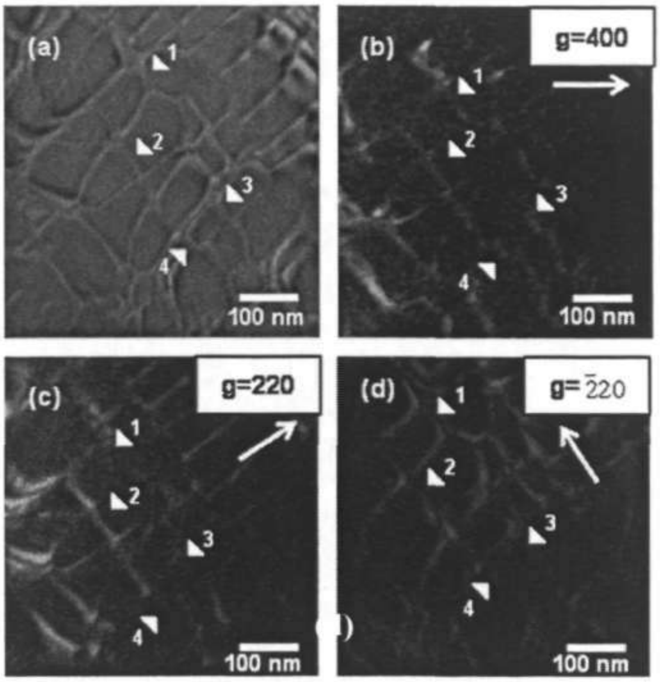

Figure 7.8. (a) Bright-field plan-view TEM image of the buffer/Si interface and the dark field images of the same location taken at (b) ***g*** = 400, (c) ***g*** = 220 and (d) ***g*** = $\bar{2}20$

For a low mismatch heteroepitaxy ($\varepsilon < 0.02$), it is generally believed that the formation of a pure edge dislocation from reactions of two 60° MDs with the appropriate Burger's vector combination is more favorable than direct nucleation [62-64]. With a large density of 60° MDs and the reduction of TDD observed, it is reasonable to assume that this reaction route would be dominant. Moreover, the short pure edge dislocation segments show that the propagation of pure edge dislocations is somehow blocked, presumably by the original network of 60° MDs or the strain field from SiGeC domains. Previous plan-view TEM observations showed the formation of pure edge dislocations from two parallel 60° MDs lying on the same interface [62,65,151]. However, these dislocation reactions are not observed in our plan-view TEM images. It is possible then, that the two 60° MDs first formed at different interfaces, (i.e. the SiGeC/SiGe interfaces) and one "climbs" or cross-slips to form pure edge dislocation. This reaction path was reported earlier by Narayan and Sharan in GaAs/Si heteroepitaxy [63].

Figure 7.9 (a) illustrates the formation of a pure edge dislocation from two 60° misfit dislocations around a SiGeC domain. The significant strain field around the SiGeC domains inhibits the glide of 60° MD and force it to cross-slip or climb around it in order to continue gliding. Figure 7.9 (b) illustrates the concentration of vacancies at the SiGeC domain/SiGe matrix interface is an additional driving force for the climb process. Finally, the reaction between two MDs also results in annihilation or fusion of threading dislocations, consistent with the TDD reduction observed earlier.

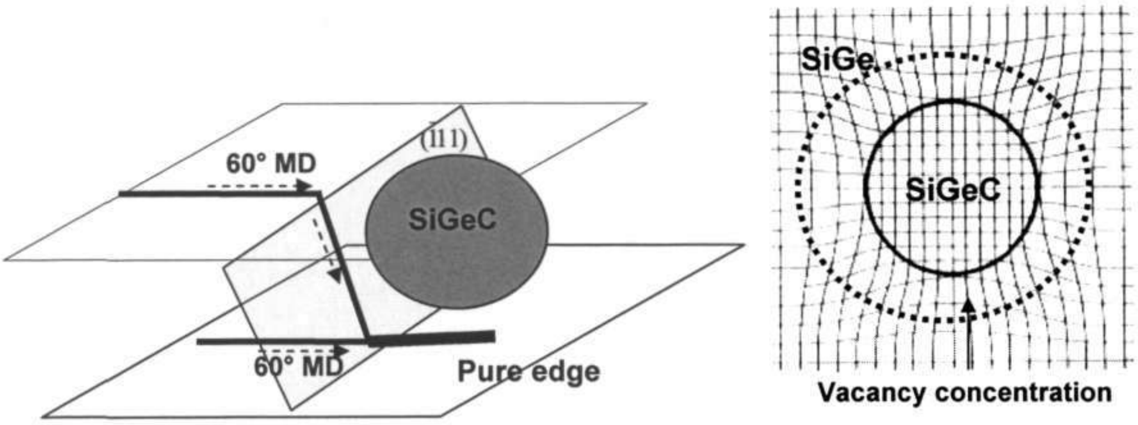

(a) (b)

Figure 7.9 Schematic of (a) two 60° misfit dislocations react to form pure edge dislocations via cross-slip, (b) the vacancy concentration at the SiGeC domain/SiGe matrix interface.

Evidence of cross-slip near the domain is shown by the HR-TEM image taken from the domain region (Fig. 7.10).

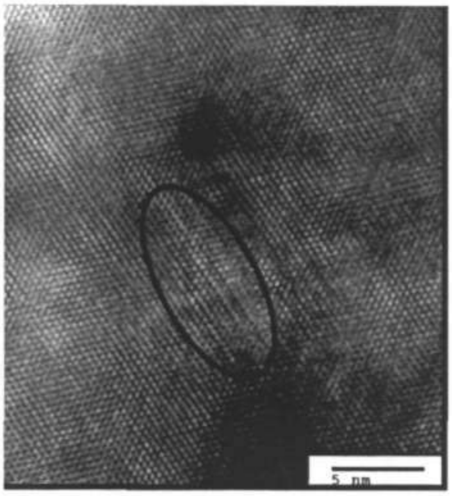

Figure 7.10. HR-TEM image of a dislocation cross-slip at the SiGeC domains area.

Finally, the more important implication of the formation of pure edge dislocation from two 60° misfit dislocations is the annihilation or fusion of threading dislocations. It was presented in section 7.1, that the TDD of the sample was 8 x 10^5/cm^2 after 800 °C anneal and 8x10^4/cm^2 after 1000 °C anneal. The difference between these two values (i.e. 7x10^5/cm^2 or rounded up to 1 threading dislocation/100 μm^2) represents the number of TD annihilation events. Assuming that the formation of one pure-edge dislocation corresponds to fusion of two threading dislocation arms into one, each pure edge dislocation corresponds to one TD annihilation event. From the TEM images, we could see more than one pure edge dislocations / 100 μm^2. Therefore, the phenomenon of TDD reduction could be explained by the pure edge dislocation formation.

It should be noted that cross-slips and climb may take place without precipitates, however, a large strain energy (4 times larger than our system) is required to initiate these reactions [62,63,152-154]. Dislocation climb can also be facilitated by Ge/C interdiffusion, which cannot be completely ruled-out at our annealing temperatures. It was reported that pure edge dislocations are formed at a distance (2 √Dt) from the SiGe/Si interface, corresponding to the diffusion length of the Ge into Si [64]. Using the diffusion coefficient of Ge into Si at 1000 °C [51], the diffusion length is about 30 nm. In a SiGeC alloy, the diffusion length could be even longer as the diffusion of Ge into Si is enhanced [90,91]. Unfortunately, to our knowledge the diffusion coefficient of Ge from SiGeC to Si at 1000°C is not available. If the diffusion-assisted climb is solely responsible for the formation of pure edge dislocations, cross-sectional TEM should show the presence of edge dislocations at a distance > 30 nm from the buffer/Si interface. Nevertheless, such dislocations are not observed (Fig 7.6 (a)). Moreover, from the plan-view TEM image (Fig. 7.8 (a)), it is clear that the pure edge dislocations lie at the same interface as the majority of the 60° MDs. Therefore, even though Ge/C diffusion might facilitate the formation of some pure edge dislocations, this mechanism is unlikely to be the dominant.

7.3. Chapter summary

In this chapter, strain relief accompanied by a reduction of TDD has been demonstrated on a SiGeC/SiGe superlattice. HR-TEM investigations reveal the homogenization of the superlattice and the presence of coherent SiGeC domains after annealing at 1000°C. Plan-view TEM observations reveal the formation of pure edge dislocations from the reaction of 60° misfit dislocations, that results in the annihilation of threading dislocations. Therefore, strain relaxation with a reduction of TDD is attributed to the dual-role of SiGeC domains that a) create elastic strain relief between the SiGeC domains/SiGe matrix and b) assist inthe formation of pure edge dislocations from reaction of 60° misfit dislocations and thus resulting in TDD annihilation. This strain relaxation mechanism which does not generate threading dislocations can be exploited for the growth of low defect density relaxed $Si_{1-x}Ge_x$ epilayers.

Chapter 8:

Conclusions and Future Work

8.1. Conclusions

Through various original experimental work, the objective of this thesis, which is to explore innovative new strategies for reducing dislocation density in SiGe/Si heteroepitaxy for strained Si application, has been achieved. Here, the conclusion and original contributions stemming from this thesis are summarized.

1. Determination of strain-shift coefficient for quantitative strain measurement by Raman spectroscopy

Direct measurement of the strain-shift coefficient of strained Si and strained SiGe has been carried out by a combination of High-resolution XRD (HR-XRD) and Raman spectroscopy. The first direct measurement of the Raman strain shift coefficient of Si-Si in strained Si, obtaining a measured value of -784 ± 4 cm^{-1}, has been presented. It has also been verified experimentally that b_{Si-Si}^{SiSiGe} is a function of Ge concentration (x), consistent with its theoretical definition, and follows the empirical relation $b = -773.8 - 897.7x$ for $x<0.35$.

2. Investigation of strain relaxation in a single epitaxial layer

Strain relaxation of two heterostructures, i.e. strained Si on relaxed SiGe and strained SiGe on Si substrate, was induced by annealing at the extreme conditions used in device manufacturing process. The purpose of this study is to study the classical relaxation mechanisms in SiGe/Si heteroepitaxy and the following conclusions can be drawn:

a. When the epilayer thickness is smaller than 2x the MB thickness ($t < 2\ t_{MB}$), strain is stable up to 1000°C for 5 minutes because of the kinetic barrier of dislocation nucleation. Since the thickness of strained Si is usually near to the MB thickness, it is reasonably stable against strain relaxation at the aforementioned annealing condition. However, Ge diffusion into strained Si was detected and is likely to be the limiting factor in real device manufacturing.

b. When the epilayer thickness is larger than 10x MB thickness ($t > 10\ t_{MB}$), experimental results suggest that surface relaxation is responsible for the initial relaxation, and after annealing at 900°C, strain relaxation takes place by misfit dislocation generation and followed by Ge diffusion.

3. A novel concept of reverse-graded buffer layer for relaxed SiGe heteroepitaxy

A novel concept of reverse grading (RG) in SiGe heteroepitaxy system has been proposed and demonstrated. This work has resulted in the following conclusions:

a. Relaxed $Si_{1-x}Ge_x$ (x = 0.14-0.35) has been successfully grown on a 90-nm RG layer with a TDD of $\sim 10^5/cm^2$ and a roughness of 1.1 nm, comparable to the best reported values [17,25,53,78].

b. TEM investigations show that strain relaxation takes place by misfit dislocations confined at the RG/Si interface and inside Si substrate, which is formed by modified Frank-Read mechanisms. The considerably large residual strain, as determined by RSM, exerts some force on the TD arms thus increasing the glide and probability of TD annihilation.

c. This heterostructure is stable up to 1000°C with no further relaxation in the RG and strained Si.

d. Unlike the well-known forward graded method, the reverse-graded concept suggests a non-conventional grading approach, which does not require full relaxation of the graded layer. Instead of using thickness to induce supersaturation of strain energy for dislocation nucleation, the highest lattice mismatch at the RG/Si interface provides the most favorable energetic route for misfit dislocation nucleation. Since all misfit dislocations required for relaxation can be confined at the interface, the graded layer thickness can be reduced significantly by using a metastable RG with large residual strain.

4. A novel SiGe/SiGeC buffer layer for low-dislocation-density strain relaxation of SiGe

Strain relaxation of SiGe on a novel SiGeC/SiGe superlattice buffer layer has been demonstrated after annealing at high temperatures, and the key results are summarized as follows:

a. An 85% relaxed SiGe with TDD of ~$10^4/cm^2$ and a roughness of 1.5 nm has been grown on a 28 nm SiGeC/SiGe superlattice buffer layer. The TDD is one of the lowest ever attained on such a thin buffer layer [17,25,53,78].

b. An unusual observation of strain relaxation accompanied by a reduction of TDD has been observed. HR-TEM study shows the absence of dislocations at the $Si_{0.77}Ge_{0.23}$/Si interface and the presence of $Si_{1-x-y}Ge_xC_y$ (with $x \leq 0.23$ and $y \leq 0.01$) domains in $Si_{0.77}Ge_{0.23}$ matrix. Plan-view TEM observations reveal the formation of pure edge dislocations from the reaction of 60° misfit dislocations, that consequently result in the annihilation of threading dislocations. Therefore, strain relaxation with a reduction of TDD is attributed to the dual-role of SiGeC domains which a) create elastic strain relief between the SiGeC domains/SiGe matrix and b) assist in the formation of pure edge dislocations from reaction of two 60° misfit dislocations that results in TDD annihilation.

8.2. Future Work

1. Reverse-graded buffer layer

Stemming from this successful preliminary study, the following future work is recommended to further exploit the advantages of the RG concept:

a. To grow a thin metastable graded layer, we postulate that the amount of initial mismatch is more important than the grading direction. In other words, if one grows a $Si_{1-x}Ge_x$ with $x = 0.5$ and reverse-grade to $x = 0.25$ or forward-grade to $x = 0.75$, and designing the thickness of the graded layer to keep similar residual strain, the strain relaxation mechanism will be similar to that established in this thesis. This hypothetical case is illustrated in Figure 8.1 and is the subject of further investigation.

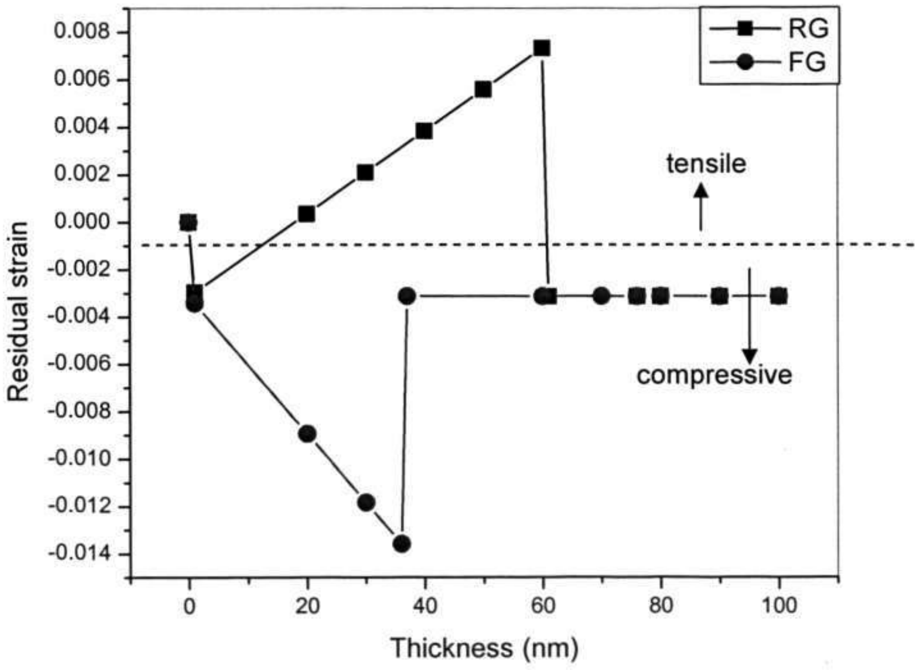

Figure 8.1. Residual strain plot of a hypothetical case of RG and FG layer with similar f_o.

It is also postulated that the RG thickness can be further reduced by increasing the mismatch at the RG/Si interface provided that the amount of residual strain is kept constant. It would be interesting to verify this postulation by starting with an RG of higher Ge concentration at the RG/Si interface.

b. Strained Si, strained SiGe, or strained Ge transistors can be grown on top of the Si/RG/relaxed SiGe heterostructure. A combination of strained Si and strained Ge which creates a dual-channel transistor for optimized nMOS and pMOS performance can also be grown on this heterostructure. Another possibility would be to grow GaAs on a SiGe RG/Si heterostructure for optical interconnect applications.

c. A relaxed pure Ge may also be grown on a reverse-graded buffer, which starts at pure Ge and graded down to $Si_{1-x}Ge_x$ with $x = 0.5$. The thickness of the RG layer is 30 nm, corresponding to the metastable thickness of the RG layer, and the thickness of the Ge layer is 30 nm, which is approximately 10x the critical thickness of pure Ge to ensure relaxation. It should be noted, however, that the growth condition should be controlled to avoid strain relaxation by 3D-islanding. One possible way to avoid islanding is to reduce the compressive strain per unit thickness by reducing the grading rate. The schematic of this idea is shown in Fig. 8.2.

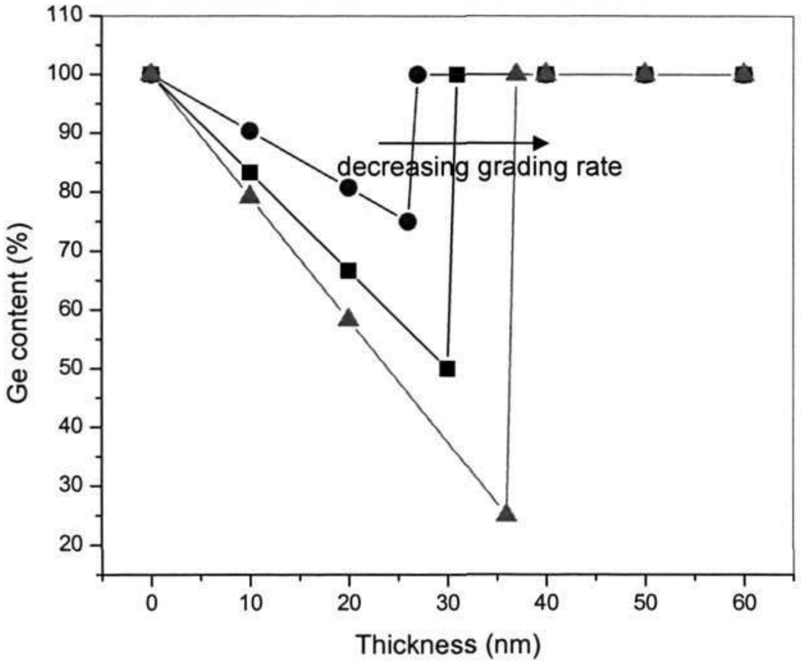

Figure 8.2. Proposed RG designs to grow relaxed pure Ge.

d. Moreover, the RG concept also implies that heteroepitaxial growth of any materials on any substrate can be accomplished by using another material with similar crystal structure and a larger lattice constant as a buffer layer. For example, one may design an RG buffer of InGaAs to grow a relaxed GaAs on Si. This approach will simplify the growth process into a single MOCVD system, rather than a combination of UHV-CVD and MOCVD usually employed to grow GaAs on forward graded SiGe [155]. This heterostructure could be used for optoelectronics on Si chips or solar cell applications.

2. SiGeC/SiGe superlattice buffer

Even though the SiC precipitates were not formed as initially predicted, the validity of the elastic strain relief between domains/matrix concept has been verified. In principle, if all epitaxial strain can be released elastically by the domains, dislocations may not be formed and (near) zero dislocation density can be achieved. However, further investigations in the following areas are recommended to fully understand the behavior of the SiGeC/SiGe heterostructure:

a. The mechanism of SiGeC domain formation is not fully understood. One possibility is that non-homogenous Ge/C diffusion may be related to the strain-field resulting from the superlattice structure and/or misfit dislocation array. To understand the role of the superlattice, SiGeC/SiGe superlattices with different thicknesses can be grown, annealed and investigated by a combination of SIMS and HRTEM. The role of misfit dislocation arrays can be investigated by growing a SiGeC/SiGe superlattice without relaxed SiGe cap, thus avoiding the formation of misfit dislocations prior to diffusion. If the formation of SiGeC domains is independently related to the misfit dislocations, a complete elastic relaxation can be realized and may result in a lower (or even zero) dislocation density. For example, the correct thickness ratio between relaxed SiGe and SiGeC/SiGe buffer layer may result in a total elastic relaxation.

b. The application of the proposed SiGeC/SiGe superlattice buffer layer can be extended to growth of pure Ge on Si. To avoid dislocation formation at the buffer/Ge interface, the Ge concentration in the SiGeC/SiGe buffer should be increased closer to pure Ge.

c. Furthermore, the characteristics of the SiGeC domains, such as their shape and distribution, should be further investigated. If the domains can be distributed uniformly, they could be used as quantum dots with optoelectronic capability. Otherwise, the domain array can be used as a template for subsequent deposition and self-organization of various nanostructure materials leading to optoelectronic or magnetic devices.

References

1. R.L. Gunshor and A.V. Nurmikko, *MRS Bulletin*, **20**, 17 (1995)
2. S.L. Yellen, A.H. Shepard, R.J. Dalby, J.A. Baumann, et al., IEEE J. Quantum Electron. **29**, 2058 (1993)
3. B.S. Meyerson, D.L. Harame, J. Stork, E. Crabbe, J. Comfort and G. Patton, Int. J. High Speed Electron. Systems **5**, 473 (1994).
4. J. Welser, J.L. Hoyt, J.F. Gibbons, *Tech. Dig. Int. Electron Dev. Meet.*, **1992**, 1000
5. K. Rim, J. Welser, J.L. Hoyt, J.F. Gibbons, *Tech. Dig. Int. Electron Dev. Meet.*, **1995**, 1026
6. J.E. Matthews, A.F. Blakeslee, J. Cryst. Growth **27**, 118 (1974).
7. K. Ismail, J. Vac. Sci Technol **B 14**, 2776 (1996)
8. L.M. Giovane, H-C. Luan, A.M. Agarwal and L.C. Kimerling, Appl. Phys. Lett. **78**, 541 (2001)
9. M.L. Lee et.al., *Tech. Dig. Int. Electron Dev. Meet.*, **2003**, 429
10. C.-H. Ge, et al., *Tech. Dig. Int. Electron Dev. Meet.*, **2003**, 3.7.1
11. I. Aberg, C. Ni Chleirigh, O.O. Olubuyide, X. Duan, J.L. Hoyt, *Tech. Dig. Int. Electron Dev. Meet.,* **2004**, 173
12. S. Takagi, J.L. Hoyt, J.J. Welser, J.F. Gibbons, J. Appl. Phys. **80**, 1567 (1996)
13. R. Oberhuber, G. Zandler, P. Vogl, Phys. Rev **B58**, 9941 (1998)
14. M.L. Lee and E.A. Fitzgerald, Appl. Phys. Lett. **83**, 4202 (2003).
15. J. Jung, M.L. Lee, E.A. Fitzgerald, and D.A. Antoniadis, IEEE Elec. Dev. Lett, **24**, 460 (2003).
16. H. Shang et al., *Tech. Dig. Int. Electron Dev. Meet.*, **2005**, 157
17. P.M. Mooney, Mat. Sci. Eng **R17**, 105 (1996).
18. Z. Ren, et al., *Tech. Dig. Int. Electron Dev. Meet.,* **2002**, 51

19. S.M. Sze, *Physics of Semiconductor Devices*, (Willey, New York 1981)
20. E.A. Fitzgerald, G.P. Watson, R.E. Proano, D.G. Ast, P.D. Kirchner, G.D. Pettit, J. M. Woodall, J. Appl. Phys. **65**, 2220 (1989)
21. E. A. Fitzgerald and N. Chand, J. Electron. Mats. **20**, 839 (1991)
22. S. Luryi and E. Suhir, Appl. Phys. Lett. **49**, 140 (1986)
23. A.R. Powell, S.S. Iyer, F.K. LeGoues, Appl. Phys. Lett., **64**, 1856 (1994)
24. Y.H. Luo, J.L. Liu, G. Jin, J. Wan, and K.L. Wang , C.D. Moore, M.S. Goorsky, C. Chih, and K.N. Tu, Appl. Phys. Lett., **78**, 1219 (2001)
25. Yu. B. Bolkhovityanov, O.P. Pchelyakov, L.V. Sokolov and S.I. Chikichev, Semiconductors **37** (5), 513 (2003), and the references therein.
26. J.W. Matthews and A.E. Blakeslee, J. Cryst. Growth **29**, 273 (1975)
27. J.W. Matthews and A.E. Blakeslee, J. Cryst. Growth **32**, 265 (1976)
28. R. Hull, J.C. Bean, R.E. Leibenguth, and D.J. Werder, J. Appl. Phys. **65**, 4723 (1989)
29. H. Chen, L. W. Guo, Q. Cui, Q. Hu, Q. Huang, and J. M. Zhou, J. Appl. Phys. **79**, 1167 (1996)
30. K. K. Linder, F. C. Zhang, J.-S. Rieh, P. Bhattacharya and D. Houghton, Appl. Phys. Lett., **70**, 3224 (1997)
31. S. W. Lee, H. C. Chen, L. J. Chen, Y. H. Peng, C. H. Kuan, H. H. Cheng, J. Appl. Phys., **92**, 6880 (2002)
32. S. Mantl, B. Holländer, R. Liedtke, St. Mesters, H.-J. Herzog, H. Kibbel, and T. Hackbarth, Nucl. Instrum. Methods Phys. Res. B **147**, 29 (1999)
33. M. Luysberg, D. Kirch, H. Trinkaus, B. Holländer, St. Lenk, S. Mantl, H.-J. Herzog,T. Hackbarth, and P. F. P. Fichtner, J. of Appl. Phys. **92**, 4290 (2002)
34. E. A. Fitzgerald, Y.-H. Xie, M. L. Green, D. Brasen, A. R. Kortan, J. Michel, Y.-J Mii, and B. E. Weir, Appl. Phys. Lett., 59, 811 (1991)

35. F. K. LeGoues, B. S. Meyerson, J. F. Morar and P. D. Kirchner, J. Appl. Phys. 71, 4230 (1992)
36. T. Hackbarth, H.-J. Herzog, K.-H. Hieber, U. Konig, M. Bollani, D. Chrastina and H. von Kanel, Appl. Phys. Lett. **83**, 5464 (2003)
37. K.A. Jenkins and K. Rim, IEEE Elec. Dev. Lett **23**, 360 (2002)
38. J.C. Tsang, P.M. Mooney, F. Dacol and J.O. Chu, J. Appl. Phys. **75,** 8098 (1994)
39. E. Anasstassakis, A. Cantarero and M. Cardona, Phys. Rev. **B 41,** 7529 (1990)
40. M. Chandrasekhar, J.B. Renucci and M. Cardona, Phys. Rev **B 17,** 1623(1978)
41. F.Cerdeira, A. Pinczuk, J.C. Bean, B. Batlogg and B.A. Wilson, Appl. Phys. Lett. **45,** 1138 (1984)
42. M. Holtz, W.M. Duncan, S. Zollner and R. Liu, J. Appl. Phys. **88,** 2523 (2000)
43. B. Dietrich, E. Bugiel, J. Klatt, G. Lippert, T. Morgenstern, H.J. Osten and P. Zaumseil, J. Appl. Phys. **74,** 3177 (1993)
44. F. Lu, C.H. Perry, F. Namavar, N.L. Rowell and R.A. Soref, Appl. Phys. Lett. **63,** 1243 (1993)
45. M.A.G. Halliwel, M.H. Lyons, S.T. Davey, M. Hockly, C.G. Tuppen and C.J. Gibbings, Semicond. Sci. Technol. **4,** 10 (1989)
46. F. Secco-D'Aragona, J. Electrochem. Soc., **119**, 948 (1972)
47. M. Wright-Jenkins, J. Electrochem. Soc., **124**, 757 (1977)
48. J. Tersoff, Appl. Phys. Lett. **62**, 693 (1993)
49. C.W. Liu, Y.D. Tseng, M.Y. Chern, C.L. Chang and J.C. Sturm, J. Appl. Phys. **85**, 2124 (1999)
50. P. Warren, J. Mi, F. Overney, M. Dutoit, J. Crys. Growth **157,** 414 (1995)
51. R. Hull, in *Germanium Silicon: Physics and Materials*, Semiconductor and Semimetals **56**, edited by R. Hull and J.C. Bean, (Academic Press, San Diego, 1999), pp. 101-167.

52. J.P. Dismukes, L. Ekstrom, and R.J. Paff, J. Phys. Chem. **68**, 3021 (1964)

53. R. Hull, J. Gray, C.C. Wu, S. Atha and J.A. Floro, J. Phys. Condens. Matter **14**, 12829 (2002)

54. J. Tersoff and F. K. LeGoues, Phys. Rev. Lett. **72**, 3570 (1994)

55. Y.-W. Mo, D.E. Savage, B.S. Swartzentruber and M.G. Lagally, Phys. Rev. Lett. **65**, 1020 (1990)

56. M. Tomitori, K. Watanabe, M. Kobayashi and O. Nishikawa, Appl. Suf. Sci. **76/77**, 322 (1994)

57. F.M. Ross, R.M. Tromp and M.C. Reuter, Science **286**, 1931 (1999)

58. G. Medeiros-Ribeiro, A.M. Bratkovski, T.I. Kamins, D.A.A. Ohlgerg, R.S. Williams, Science **279**, 353 (1998)

59. G.F.A. Van de Walle et al., Thin Solid Films **183**, 183 (1990)

60. A.T. Fiory, J.C. Bean, R. Hull and S. Nakahara, Phys. Rev. **B31**, 4063 (1985)

61. N. Sugii, J. Appl. Phys. **89**, 6459 (2001)

62. K.H. Chang, P.K. Bhattacharya, R. Gibala, J. Appl. Phys. **66**, 2993 (1989)

63. J. Narayan and S. Sharan, Mat. Sci and Eng **B10**, 261 (1991)

64. F.K. LeGoues, A. Powell and S.S. Iyer, J. Appl. Phys. **75**, 7240 (1994)

65. V.I. Vdovin, J. Cryst. Growth **172**, 58 (1997)

66. R.Hull and J.C. Bean, Crit Rev. Solid State Mater. Sci. **17** , 507 (1992)

67. B.W. Dodson and J.Y. Tsao, Appl. Phys. Lett. **51**, 1325 (1987)

68. D.C Houghton, J. of Appl. Phys. **70**, 2136 (1991)

69. W.A. Jesser and J.W. Matthews, Phil. Mag. **15** , 1097 (1967)

70. J.Zou, D.J.H. Cockayne, J.J. Russel-Harriott, Appl. Phys. Lett**.** **70**, 3134 (1997)

71. D.D. Perovic, G.C. Weatherly, J.M. Baribeu, D.C. Houghton, Thin Solid Films **183**, p 141 (1989)

72. D.J. Eaglesham, D.M. Maher, E.P. Kvam, J.C. Bean, C.J. Humphreys, Phys. Rev. Lett. **62**, 187 (1989)

73. W. Hagen and H. Strunk, Appl. Phys.**17**, 85 (1978)

74. F.C. Frank, *Symp.on Plastic Deformation of Crystalline Sollids*, Carnegie Institute of Tech. Pittsburg, 1950, 89

75. F.K. LeGoues, B.S. Meyerson, and J.F. Morar, Phys. Rev. Lett. **66**, 2903 (1991)

76. A. Lefebvre, C. Herbeaux, C. Bouillet and J. Di Persio, Phil. Mag. Lett. **63**, 23 (1991)

77. R. Beanland, J. Appl. Phys. **72**, 4031 (1992)

78. R. Beanland, D.J. Dunstan, and P.J. Goodhew, Advances in Physics **45**, 87 (1996)

79. J.S. Speck, M.A. Brewer, G.E. Beltz, A.E. Romanov and W. Pompe, J. Appl. Phys. **80**, 3808 (1996)

80. A.E. Romanov, W. Pompe, G.E. Beltz, J. S. Speck, Appl. Phys. Lett. **69**, 3342 (1996)

81. A.E. Romanov, W. Pompe, G. Beltz, and J.S. Speck, Phys. Status Solidi B**198**, 599 (1996)

82. A.E. Romanov, W. Pompe, G. Beltz, and J.S. Speck, Phys. Status Solidi B**199**, 33 (1997)

83. G.E. Beltz, M. Chang, J.S. Speck, A.E. Romanov and W. Pompe, Philos. Mag. A **76**, 807 (1997)

84. A.E. Romanov, W. Pompe, S. Mathis, G.E. Beltz, J.S. Speck, J. Appl. Phys. **85**, 182 (1999)

85. H. Chen, L.W. Guo, Q. Cui, Q. Hu, Q. Huang, J.M. Zhou, Appl. Phys. Lett. **79**, 1167 (1996)

86. J.H. Li, V. Holy, G. Bauer, F. Schaffler, J. Appl. Phys. **82**, 2881 (1997)

87. F.K. LeGoues, Phys. Rev. Lett. **72**, 876 (1994)

88. S.S. Iyer, K. Eberl, M.S. Goorsky, F.K. LeGoues, J.C. Tsang and F. Cardone, Appl. Phys. Lett. **60**, 356 (1992)

89. K. Eberl, S.S. Iyer, S. Zollner, J.C. Tsang, and F.K. LeGoues, Appl. Phys. Lett. **60**, 3033 (1992)

90. P. Zaumseil, G.G. Fischer, K. Brunner, and K. Eberl, J. Appl. Phys. **81**, 6134 (1997)

91. P. Zaumseil, J. Phys. D: Appl. Phys. **32**, A75 (1999)

92. M.S. Caroll, J. C. Sturm, D. De Salvador, E. Napolitani, M. Berti, J. Stangl, G. Bauer, Mater. Res. Soc. Symp. Proc. **669,** J6.7 (2001)

93. E. Napolitani, D.De Salvador, A. Coati, M. Berti, A.V. Drigo, M.S. Caroll, J.C. Sturm, J. Stangl, G. Bauer, C. Spinella, Nucl. Inst. Methods in Phys. Res. B **186**, 212 (2002)

94. H.J. Osten and E. Bugiel, Appl. Phys. Lett. **70,** 2813 (1997)

95. B. Dietrich, H.J. Osten, H. Rucker, M. Methfessel, P. Zaumseil, Phys. Rev. **B49**, 17185 (1994)

96. R. Delhougne, P. Meunier-Beillard, M. Caymax, R. Loo and W. Vandervorst, Appl. Surf. Sci. **224**, 91 (2004).

97. D.A. Porter and K.E. Easterling, *Phase Transformations in Metals and Alloys*, (Van Nostrand Reinhold, New York, 1981), p. 155

98. M.L. Hitchman and K.F. Jensen, *Chemical Vapor Deposition: Principles and Applications*, (Academic Press, 1993)

99. D.J. Robbins, J.L. Glasper, A.G. Gullis, W.Y. Leong, J. Appl. Phys. **69**, 3729 (1991).

100. A. Shimizu et al., *Tech. Dig. Int. Electron Dev. Meet.*, **2001**, 433

101. T. Matsumono et al., *Tech. Dig. Int. Electron Dev. Meet.*, **2002**, 663

102. K.W. Ang, K.-J. Chui, V. Bliznetsov, C.-H. Tung, A. Du, N. Balasubramanian, G. Samudra, M. F. Li, and Y.-C. Yeo, Appl. Phys. Lett. **86**, 093102 (2005)

103. J.R. Ferraro, K. Nakamoto, *Introductory Raman Spectroscopy*, (Academic Press, San Diego 1994)

104. I. De Wolf, Semicond. Sci. Technol. **11**, 139 (1996)

105. E. Anastassakis, A.Pinczuk, E. Burstein, F.H. Pollack and M. Cardona, Solid State Commun. **8,** 133 (1970)

106. S. Ganesan, A.A. Maradudin and J. Oitmaa, Ann. Phys. **56**, 556 (1970)

107. D.K. Bowen and B.K. Tanner, *High Resolution X-ray Diffractometry and Topography* (Taylor and Francis, London 1998)

108. S. Mahajan, K.S.S Harsha, *Principles of Growth and Processing of Semiconductors*, (McGraw Hill, Singapore 1999)

109. K.R Bray et.al., J. Electrochem. Soc. **152,** C310 (2005)

110. S.W. Bedell et al., Electrochem. Sol. State Lett. **7,** G105 (2004)

111. D.B. Williams and C.B Carter, *Transmission Electron Microscopy: A Text Book for Materials Science*, (Plenum Press, 1996)

112. M. Cabie, A. Ponchet, A. Rocher, V. Paillard and L. Vincent, Appl. Phys. Lett. **84,** 870 (2004)

113. S. Nakashima, T. Yamamoto, A. Ogura, K. Uejima and T. Yamamoto, Appl. Phys. Lett. **84,** 2533 (2004)

114. Z. Di, M. Zhang, W. Liu, C. Lin and P. K. Chu, Mater. Sci. Semicond. Process. **7,** 393 (2004)

115. T. Tezuka, N. Sugiyama and S. Takagi, Mater. Sci. Eng **B89,** 360 (2002)

116. B. Ghyselen et al., Solid-State Electron. **48,** 1285 (2004)

117. D.J. Lockwood and J.M. Baribeau, Phys. Rev. **B 45,** 8565 (1992)

118. M.I. Alonso and K. Winer, Phys. Rev. B **39,** 10056 (1989)

119. S.B. Samavedam, W.J. Taylor, J.M. Grant, J.A. Smith, P.J. Tobin, A. Dip, A.M Philips, R. Liu, J. Vac. Sci. Tech. B **17**, 1424 (1999)

120. S.J. Koester, K. Rim, J.O. Chu, P.M. Mooney, J.A. Ott, Appl. Phys. Lett. **79**, 2148 (2001)

121. S.R. Stiffler, et al., J. Appl. Phys. **70**, 1416 (1991)

122. A. Fischer, H. Kuhne, M. Eichler, F. Hollander, and H. Richter, Phys. Rev. **B54**, 8761 (1996)

123. F. Huang, Phys. Rev.Lett. **85**, 4411 (2000)

124. A. Fischer, Phys. Rev.Lett. **85**, 4412 (2000)

125. C. Kim, I.K. Robinson, J. Myoung, K. Shim, M.-C. Yoo, K. Kim, Appl. Phys. Lett. **69**, 2358 (1996)

126. Y.B. Bolkhovityanov, A.K. Gutakovskii, V.I. Mashanov, O.P. Pchelyakov, M.A. Revenko and L.V. Sokolov, J. Appl. Phys. **91**, 4710 (2002)

127. W. Lu, D.B. Li, C.R. Li, F. Shen, and Z.Zhang, J. Appl. Phys. **95**, 4362 (2004)

128. V.T. Gillard, W.D. Nix, L.B. Freund, J. Appl. Phys. **76,** 7280 (1994)

129. F.K. LeGoues, R. Rosenberg and B.S. Meyerson, Appl. Phys. Lett. **54**, 644 (1989)

130. D.K. Nayak, K. Kamjoo, J.C.S. Woo, J.S. Park, K.L. Wang, Appl. Phys. Lett. **56**, 66 (1990)

131. J.W. Hsu, E.A. Fitzgerald, Y.H. Xie, P.J. Silverman, M.J. Cardillo, Appl. Phys. Lett. **61**, 1293 (1992)

132. J. Xiang, N. Herbots, H. Jacobsson, P. Ye, S. Hearne, S. Whaley, J. Appl. Phys. **80,** 1857 (1996)

133. D. Dutartre, P. Warren, F. Provenier, F. Chollet and A. Perio, J. Vac. Sci Technol. A **12**, 1009 (1994)

134. J.H. Li, E. Koppensteiner, G. Bauer, M. Hohnisch, H.-J. Herzog, and F. Schaffler, Appl. Phys. Lett. **67**, 223 (1995)

135. C. Tatsuyama, T. Asano, T. Nakao, H. Matada, T. Tambo and H. Ueba, Thin Solid Films **369**, 161 (2000)

136. T. Asano, T. Nakao, H. Matada, T. Tambo, H. Ueba and C. Tatsuyama, J. Appl. Phys. **87**, 8759 (2000)

137. S. Bozzo, J.-L. Lazzari, C. Coudreau, et al., J. Cryst. Growth **216**, 171 (2000)

138. C. Rosenblad, T. Graf, J. Stangl, Y. Zhuang, G. Bauer, J. Schulze, H. von Kanel, Thin Solid Films **336**, 89 (1998)

139. C. Rosenblad, J. Stangl, E. Muller, G. Bauer, H. Von Kanel, Mat. Sci. Eng **B71**, 20 (2000)

140. D.J. Dunstan, Semicond. Sci. Technol. **6**, A76 (1991)

141. K. Sawano, S. Koh, Y. Shiraki, N. Usami, and K. Nakagawa Appl. Phys. Lett. **83**, 4339 (2003)

142. C. W. Leitz, M. T. Currie, A. Y. Kim, J. Lai, E. Robbins, E. A. Fitzgerald, M. T. Bulsara, J. Appl. Phys. **90**, 2730 (2001)

143. H. Chen, Y. K. Li, C. S. Peng, H. F. Liu, Y. L. Liu, Q. Huang, J. M. Zhou and Qi-Kun Xue, Phys. Rev. B **65**, 233303 (2002)

144. A.-C. Lindgren, C. Chen, S.-L. Zhang, M. Ostling, Y. Zhang, and D. Zhu, J. Appl. Phys., **91**, 2708 (2002)

145. C.S. Tan, W.K. Choi, L.K. Bera, K.L. Pey, D.A. Antoniadis, E.A. Fitzgerald, M.T. Currie, and C.K. Maiti, Solid State Electronics, **45**, 1945 (2001)

146. S.H. Olsen, A.G. O'Neill, L.S. Driscoll, S. Chattopadhyay, K.S.K. Kwa, A.M. Waite, Y.T. Tang, A.G.R. Evans, and J. Zhang, IEEE Trans. Elect. Dev., **51**, 1156 (2004)

147. P. Gaiduk, A.N. Larsen and J.L. Hansen, Thin Solid Films **367**, 120 (2000)

148. R. Hull and J.C. Bean, J. Vac. Sci Technol. **A7**, 2580 (1989)

149. V.I. Vdovin, Phys. Stat. Sol (a) **171**, 239 (1999)

150. J.P. Hirth, in *Physical Metallurgy Part II*, edited by R.W. Cahn and P. Haasen (Elsevier, Netherlands, 1983), p. 1224-1258.

151. A.F. Marshall, D.B. Aubertine, W.D. Nix and P.C. McIntyre, J. Mater. Res. **20**, 447 (2005)

152. F.K. LeGoues, M. Copel and R.M. Tromp, Phys. Rev. B **42**, 11690 (1990)

153. J. Zou, X.Z. Liao, D.J.H. Cockayne, Z.M. Jiang, Appl. Phys. Lett. **81**, 1996 (2002)

154. A. Sakai, N. Taoka, O. Nakatsuka, S. Zaima and Y. Yasuda, Appl. Phys. Lett. **86,** 221916 (2005)

155. C.L. Andre, J.J. Boeckl, D.M. Wilt, A.J. Pitera, M.L. Lee, E.A. Fitzgerald, B.M. Keyes, S.A. Ringel, Appl. Phys. Lett. **84**, 3447 (2004)

Appendix 1

Raman penetration depth in Si, Ge, and SiGe

4. Probing depth of the laser light

The total scattered light intensity integrated from the surface of the sample to a depth d, I_s, is given by [14]:

$$I_S = I_o D \int_0^d e^{-2\alpha x} dx = \frac{I_o D}{2\alpha}(1 - e^{-2\alpha d}) \tag{14}$$

while that from the depth d to infinity is given by

$$I_d = I_o D \int_d^\infty e^{-2\alpha x} dx = \frac{I_o D}{2\alpha} e^{-2\alpha d} \tag{15}$$

I_O, D and α are the incident light intensity, the Raman scattering cross section and the photoabsorption coefficient of the probed material, respectively. If one assumes that the penetration depth, d_P, is given by the depth that satisfies the relationship

$$\frac{I_d}{I_S + I_d} = 0.1 \tag{16}$$

then this depth is given by

$$d_p = \frac{-\ln 0.1}{2\alpha} = \frac{2.3}{2\alpha} \tag{17}$$

The values for α were taken from the IMEC spectroscopic ellipsometry library [15], or from an interpolation of data given in [16] or [17].

Silicon Si

Crystal structure: cubic, diamond

Space group: Fd3m O^7_h

Raman frequency:

Mode	ω_0 (Rcm^{-1})	Ref.
LO=TO	521	[N]

Spectrum:

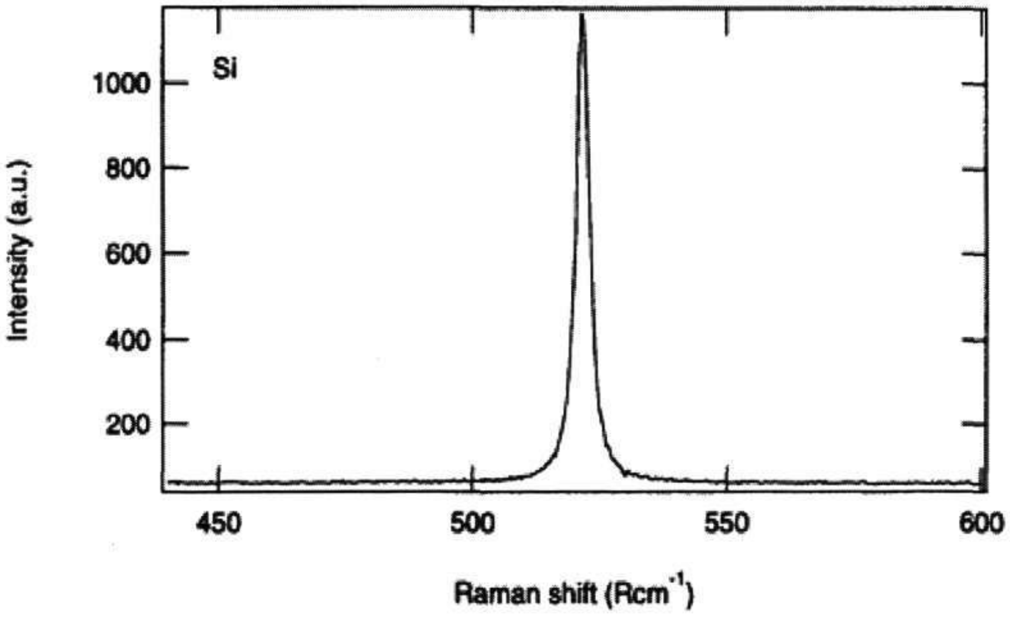

Probed depth by Raman spectroscopy:

(λ in nm, α in cm^{-1}, depth in nm) [15]

Ar+ laser lines								
λ	514.5	501.7	496.5	488	476.5	472.7	465.8	457.9
$10^{-3}\alpha$	15.08	17.39	18.19	20.23	27.27	30.80	34.05	36.66
depth	762	661	632	569	422	373	338	313

Kr^+ *laser lines*										
λ	799.3	752.5	676.4	647.1	568.2	530.9	520.8	482.5	476.2	423.1
$10^{-3}\ \alpha$	0.96	1.41	2.72	3.51	7.13	11.77	13.78	22.72	27.56	66.31
depth	11947	8183	4226	3273	1612	977	834	506	417	173

Mechanical stress:

γ	p/ω_0^2	q/ω_0^2	r/ω_0^2	Ref.
1.08 ± 0.07	-1.85 ± 0.06	-2.31 ± 0.06	-0.71 ± 0.02	[18]

Temperature :

Mode	A	B	C	D	Ref.
LO	1.295	0.105	-2.96	-0.174	0-1200K [13]
	1.28	0.04	-3.4	-	[19]

300-600 K:

x	x (T = 0) (cm^{-1})	dx/dT (cm^{-1}/K)	Ref.
$\Delta\omega$	527.874	-0.0242	[N]
$\Delta\omega$	528.6	-0.0247	[19]
Γ	3.1221	0.0102	[N]

Germanium Ge

Crystal structure: cubic, diamond

Space group: Fd3m O^7_h

Raman frequency:

Mode	ω_0 (Rcm^{-1})	Ref.
LO=TO	301	[17]

Spectrum:

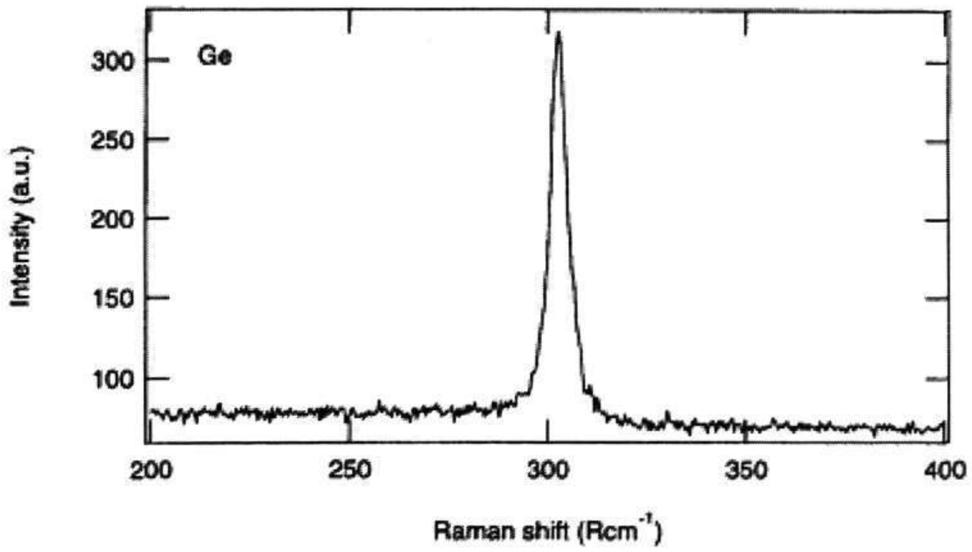

Probed depth by Raman spectroscopy: [15]

(λ in nm, α in cm^{-1}, depth in nm)

Ar⁺ laser lines								
λ	514.5	501.7	496.5	488	476.5	472.7	465.8	457.9
10^{-3} α	600	602	603	605	609	610	612	614
depth	19.2	19.1	19.1	19	18.9	18.8	18.8	18.7

Kr^+ laser lines

λ	799.3	752.5	676.4	647.1	568.2	530.9	520.8	482.5	476.2	423.1
$10^{-3}\alpha$	51	61	98	130	448	573	595	607	609	635
Depth	227	188	117	88	26	20	19	19	19	18

Mechanical stress:

γ	$(p-q)/2\omega_0^2$	r/ω_0^2	Ref.
0.89	0.23	-0.87	[23]

Temperature :

mode	A	B	ω_0	C	D	Ref.
LO	0.54	0.06	306.4	-1.4	-	[19]

300-600 K:

	ω (T = 0) (cm^{-1})	dω/dT (cm^{-1}/K)	Ref.
$\Delta\omega$	307.1	-0.02	[19]

Similar relations to those reported for polycrystalline and amorphous silicon can be obtained for Germanium. In particular the average bond angle distortion obeys the following relationship [66]:

$\Gamma^2 = \Gamma_0^2 + \Gamma_\theta^2$ where

$\Gamma_\theta = 5.31\,\Delta\theta_b$

Here Γ_0 is the finite linewidth for the crystalline phonon and Γ_θ is the linewidth due to a random variation of the bond-angle. Γ is two times the half-width at half maximum at the high frequency side of the peak.

Silicon-Germanium $Si_{1-x}Ge_x$

Crystal structure: cubic, diamond

Raman frequency:
The main physical parameters can be obtained from those of Si and Ge by interpolation.

Mode	ω_O (Rcm^{-1})	Ref.
Si-Si	near 500	[24]
Si-Ge	near 400	
Ge-Ge	near 300	

The Si-Si peak varies linearly with composition [24, 27]:
$\omega_{Si\text{-}Si} = 520 - 68\,x$ (cm^{-1})

The Si-Ge peak frequency varies slowly over most of the composition range:
$\omega_{Si\text{-}Ge} = 400.5 + 12\,x$ (cm^{-1})

Spectrum: sample: 120 nm SiGe on Si substrate, 30% Ge

Si-Si, Si-Ge, Ge-Ge:	Raman signals from the Si-Ge film
Si:	Si Raman signal from the substrate

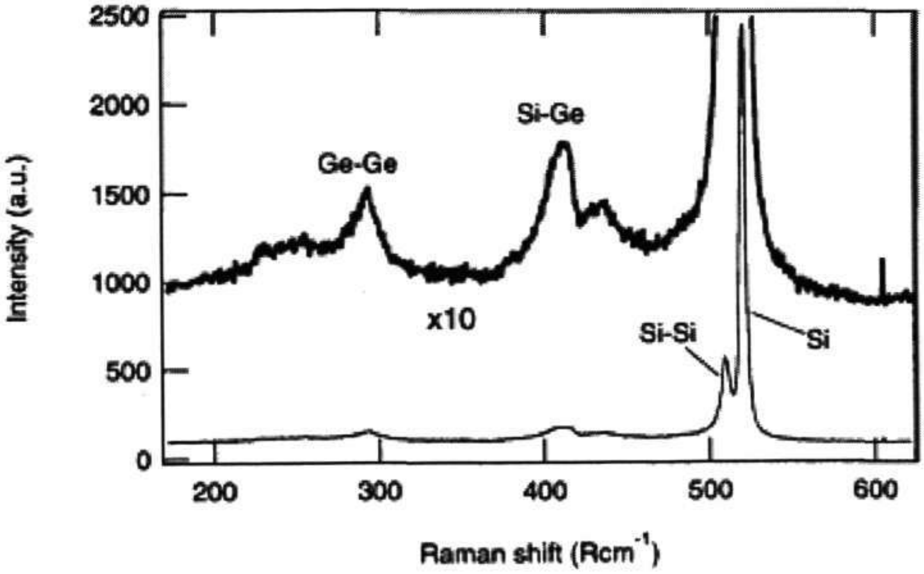

Probed depth by Raman spectroscopy:

Depending on the composition, the probed depth, d, is between the one for Si and the one for Ge. A good estimation can be obtained by assuming:

$$d_{SiGe} = (1-x)\, d_{Si} + x\, d_{Ge}$$

Mechanical stress:

A SiGe layer on a Si substrate will be under compressive stress. In such a layer, the frequency of the Si-Si peak is at a higher frequency than for an unstressed layer. In a partly relaxed SiGe layer, the frequency of the Si-Si peak will be shifted down. The relation between strain in the layer, ε, and peak position is given by [25]:

$$\Delta\omega_{Si\text{-}Si}\ (\mathrm{cm}^{-1}) = -9.3\, \varepsilon\ (\%)$$

Grüneisen constant of SiGe alloys [26]:

x	$\gamma_{Ge\text{-}Ge}$	$\gamma_{Ge\text{-}Si}$	$\gamma_{Si\text{-}Si}$
1.00	1.12	-	-
0.84	1.06	1.20	-
0.78	1.03	1.21	-
0.46	1.31	-	1.24
0.23	-	-	1.10
0.09	-	-	1.15
0.00	-	-	1.02

Temperature (range 300 to 800 K) [19]:

Mode	x	ω (T = 0) (cm^{-1})	dω/dT (cm^{-1}/K)
Si-Si	0.08	522.7	-0.0239
	0.30	509.4	-0.0238
	0.41	501.8	-0.0211
	0.71	476.9	-0.0207
Ge-Si	0.41	414.1	-0.0215
	0.71	411.5	-0.0232
	0.85	403.7	-0.0259
Ge-Ge	0.41	294.7	-0.0187
	0.71	299.5	-0.0210
	0.85	303.9	-0.0225

Amorphous SiGe [N]:

$\omega_{Si\text{-}Si} = 478.3 - 42.1\, x$

$\omega_{Si\text{-}Ge} = 380.8 + 15.6\, x$

Appendix 2

Author's Publication List

JOURNAL ARTICLES:

1. Strain relaxation mechanism in a reverse compositionally-graded SiGe heterostructure
   L.H. Wong, J.P. Liu, F. Romanato, C.C. Wong, and F.Y. Lim
   Applied Physics Letters 90, 061913 (2007)

2. Threading-dislocation reduction by SiGeC domains in SiGe/SiGeC heterostructures: Role of pure edge dislocations
   L.H. Wong, C. Ferraris, C.C. Wong and J.P. Liu,
   Applied Physics Letters 89, 231906 (2006)

3. Low dislocation density strain relaxation of SiGe on a SiGe/SiGeC buffer layer
   L.H. Wong, J.P. Liu, C. Ferraris, C.C. Wong, M.C. Jonathan, T.J. White, L. Chan
   Applied Physics Letters 88, 041915 (2006)

4. Thermal stability of a reverse-graded SiGe buffer layer for relaxed SiGe
   L.H. Wong, J.P. Liu, C.C. Wong, C. Ferraris, T.J. White, L. Chan, D.K. Sohn, L.C. Hsia
   Electrochemical Society Solid-State Letters 9 (4), G114-G116, (2006)

5. Determination of Raman phonon strain shift coefficient of strained Si and strained SiGe
   L.H. Wong, C.C. Wong, J.P.Liu, D.K. Sohn, L. Chan, L.C.Hsia, H.Zang, Z.H. Ni, Z.X. Shen
   Japanese Journal of Applied Physics Part 1, 44 (11), 7922 (2005)

6. A novel thin buffer concept for epitaxial growth of relaxed SiGe layers with low threading dislocation density
   J.P. Liu, L.H. Wong, D. K. Sohn, L.C. Hsia, L. Chan, C.C. Wong, H.J. Osten
   Electrochem. Solid-State Letters, 8 (2), G60-G62, (2005)

7. Thermal stability of strained Si/$Si_{1-x}Ge_x$ heterostructures for advanced microelectronics devices
   L.H.Wong, C.C. Wong, K.K. Ong, J.P. Liu, L. Chan, R.Rao,K.L. Pey, L. Liu, Z.X.Shen
   Thin Solid Film 462-463, 76-79, (2004)

CONFERENCE PRESENTATIONS:

1. Enhanced Dopant Activation in Strained-Si/Si1-xGex Substrate Using Non-melt Laser Annealing
   K. Pey, K. Ong, P. Lee, A. Wee, X. Wang, A. Chong, L. Wong and C. Wong
   208th Meeting of The Electrochemical Society, Los Angeles, California(2005)

2. Thermal stability of a reverse-graded layer for relaxed SiGe/Si heteroepitaxy
   L.H. Wong, C.C. Wong, R.Rao, C.Ferraris, T.J.White, J.P. Liu, L. Chan,
   3rd Int. Conf. on Mat. Adv. Tech (ICMAT), Singapore (2005)

3. Thermal stability of a novel graded layer for relaxed SiGe/Si heteroepitaxy
   L.H. Wong, C.C. Wong, C.Ferraris, T.J.White, J.P. Liu, L. Chan,
   207th Meeting of the Electrochemical Society, Quebec City, Canada (2005)

4. Thermal Relaxation of Metastable SiGe in Strained SiGe/Si Heterostructures
   L.H. Wong, C.C. Wong, J.P. Liu, K.C. Tee, L. Chan
   3rd Int. Conf. on Matl. Processing for Properties and Performance (MP^3), Singapore (2004)

5. The Effects of Ablated Particles' Kinetic Energy on the Crystallization behavior of HfO_2 thin films in pulsed laser deposition
   V.S. Chin, L.H. Wong, C.C. Wong, C.K.P. Lee, A. Patran and R.S. Rawat
   2nd Int. Conf. on Tech. Adv. of Thin Films and Surf. Coatings, Singapore, (2004)

6. Thermal stability of strained $Si/Si_{1-x}Ge_x$ heterostructures for advanced microelectronics devices
   L.H.Wong, C.C. Wong, K.K. Ong, J.P. Liu, L. Chan, R.Rao,K.L. Pey, L. Liu, Z.X.Shen
   2ndInt. Conf. on Mat. Adv. Tech (ICMAT), Singapore (2003)

PATENTS:

Method of manufacturing A Semiconductor device with a strained channel
Chui King Jien, Yeo Yee Chia, Ganesh S Samudra, Liu Jinping, Tee Kheng Chok, Lydia Wong, Phua Wee Hong
pending to US Patent Office